A coherent light-matter interface with a semiconductor quantum dot in an optical microcavity

Inauguraldissertation

zur
Erlangung der Würde eines Doktors der Philosophie
vorgelegt der
Philosophisch-Naturwissenschaftlichen Fakultät
der Universität Basel

von

Daniel Najer
aus Dagmersellen LU

2019

Genehmigt von der Philosophisch-Naturwissenschaftlichen Fakultät
auf Antrag von

Prof. Dr. Richard J. Warburton

Prof. Dr. Jacek Kasprzak

Basel, den 21. Mai 2019

Prof. Dr. Martin Spiess
Dekan

To my wife, Tharmini, and our two little boys, Ajay & Ashwin.

Preface

The development of a functioning quantum computer operating on many quantum bits (qubits) is an ongoing global challenge. One proposed way of realising quantum computation is to use the polarisation of single photons as photonic qubits [1, 2]. This offers the advantage of scalability – the number of qubits can easily be scaled up by the generation of many single-photon pulses [3].

The fundamental problem is that photons do not interact with each other. This can be solved by means of a strongly-coupled atom-cavity system, where a photon emitted by a single trapped three-level atom (or "artificial atom") can be reabsorbed due to the strong light-matter interaction before it leaks out of the cavity or via other loss channels. This system can act as mediator between two photonic qubits by providing controlled (photon-photon) gate operations between them [3]. A measure for how well these gate operations can be performed is the (gate) fidelity. The fidelity itself depends on the cooperativity C of the strongly-coupled atom-cavity system [4], the figure-of-merit which relates the coherent light-matter coupling to all incoherent losses in the system: the higher the cooperativity, the higher the gate fidelity.

Achieving a high cooperativity in a strongly coupled atom-cavity system with optical photons – which can be transported over large distances and allow for fast gate operations – has been a major challenge in atomic [5–8] and solid-state physics [9–16]. Until 2018, the (time-averaged) cooperativities reported in literature were (at most) in the order of ten [7–10, 14, 17–20].

This thesis describes the experimental realisation of high-cooperativity strong coupling ($C = 150$) between an "artificial" atom (a semiconductor quantum dot) and a fully tunable optical microcavity. Embedding the quantum dots within an n-i-p diode allows for deterministic charging with single electrons or holes – i.e. with a single spin [21] – via the Coulomb blockade effect [22], which delivers the requested three-level "atom" for realising a photon-photon gate. The potential photon-photon gate fidelity for the present sample is already 77%. With an advanced semiconductor design that would reduce the intrinsic cavity loss by a factor of ten, the fidelity could be increased to 92%, proof of the high potential of the investigated system for quantum technology.

Chapter 1 gives a short introduction to the relevant physics in the context of cavity quantum electrodynamics (cavity-QED) and discusses the experimental requirements for entering the strong-coupling regime. Alternative solid-state implementations of strong coupling with monolithic microcavities are briefly discussed and a motivation for using a tunable microcavity together with InAs quantum dots embedded in an n-i-p diode is given.

In Chapter 2, the experimental realization of strong coupling is presented and compared to the standard model of cavity-QED, the Jaynes-Cummings model. Besides a very clear avoided crossing at resonance without the solid-state "noise" (cavity-feeding) which has complicated previous solid-state implementations, intensity correlation measurements reveal the vacuum Rabi-oscillations as a manifestation of the coherent atom-photon exchange: the quantum dot and the empty microcavity coherently exchange a single quantum of energy several times before the system decoheres. Moreover, photon-statistics spectroscopy as an alternative spectroscopy method is used to probe the second rung of the Jaynes-Cummings ladder.

Chapter 3 provides more experimental background on Chapter 2. The design and characterisation of the n-i-p diode and microcavity is presented together with additional measurements in the strong-coupling regime using resonant excitation. This chapter demonstrates for the reproducibility of the measurements presented in Chapter 2.

Chapter 4 discusses the experimental challenges to achieve $\mathcal{Q}$-factors up to one million in a semiconductor microcavity involving gates and includes a recipe to passivate the semiconductor DBR surface that enhances the $\mathcal{Q}$-factor by almost two orders of magnitude.

Chapter 5 presents two alternative methods to produce micron-sized mirror curvatures in order to reduce the cavity's mode volume and thus increase the coupling strength in a tunable microcavity.

In Chapter 6, a summary is given for all presented experiments together with some perspectives for future direction.

Contents

Chapter 1

Introduction

1.1 Cavity quantum electrodynamics

Cavity quantum electrodynamics (cavity-QED) is the study of the fully quantum interaction between one or several atoms and a light field confined by an optical resonator [23, 24]. "Atom" here means a conventional atom, a molecule [25] or an "artificial" atom such as a semiconductor quantum dot, a nitrogen-vacancy (NV) centre in diamond [26], etc.

1.1.1 Relevant parameters

Once a two-level atom consisting of a ground state $|\mathrm{g}\rangle$ and an excited state $|\mathrm{e}\rangle$ is excited optically, it can decay radiatively by emitting a photon of frequency ω_0 with rate γ_{rad} or non-radiatively (rate γ_{nonrad}) by creating a phonon, for instance. The sum of both yields the atom decay rate $\gamma = \gamma_{\mathrm{rad}} + \gamma_{\mathrm{nonrad}}$. Ignoring non-radiative decay processes and assuming the atom is in a homogeneous medium with refractive index n, the total decay rate [27] can be written as

$$\gamma = \frac{1}{\tau_{\mathrm{rad}}} = \frac{n\omega^3}{3\pi\epsilon_0\hbar c^3} \cdot \mu^2, \tag{1.1}$$

where τ_{rad} is the radiative lifetime and c the speed of light. The cavity-photon loss rate κ includes all losses due to transmission, scattering and absorption of the cavity mirrors. It is inversely proportional to the cavity's $\mathcal{Q}$-factor,

$$\kappa = \frac{1}{\tau_{\mathrm{cav}}} = \frac{\omega}{\mathcal{Q}}, \tag{1.2}$$

where τ_{cav} is the lifetime of a photon inside the cavity. In case of perfect overlap of the atomic transition dipole moment μ with the polarization of the vacuum electric field of

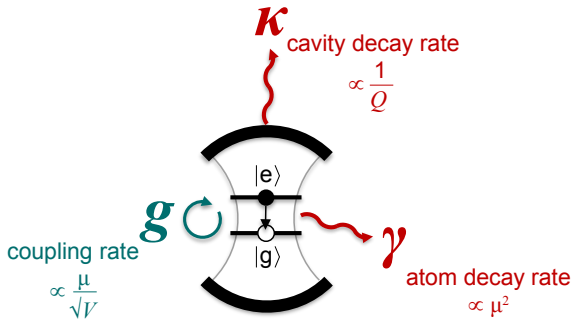

Fig. 1.1. The three relevant parameters of cavity-QED. Schematic of a two-level system with excited (ground) state $|e\rangle$ ($|g\rangle$) coupled to a single quantized mode of the electromagnetic field. The system dynamics are described by three parameters: the cavity photon loss rate κ, the atom decay rate γ into all other modes except the cavity mode as well as the coupling rate g between the atom's transition dipole moment μ and the cavity-confined vacuum state of the electromagnetic field. Dependence on the cavity and emitter properties (cavity $\mathcal{Q}$-factor, effective mode volume V, dipole moment μ) are given in the figure.

amplitude E_{vac}, the interaction between both is described by the coupling rate (Fig. 1.1)

$$g = \frac{\mu E_{\mathrm{vac}}}{\hbar}. \tag{1.3}$$

Taking equal contribution [28] of magnetic and electric fields to the total vacuum energy, the coupling strength reads

$$g = \sqrt{\frac{\omega}{2\hbar\epsilon_0 n^2}} \cdot \frac{\mu}{\sqrt{V}}, \tag{1.4}$$

where V is the cavity's effective mode volume.

1.1.2 Cooperativity and quantum efficiency

The figure-of-merit of a cavity-QED system is its cooperativity defined as

$$C = \frac{2g^2}{\kappa\gamma} \propto \frac{\mathcal{Q}}{V}, \tag{1.5}$$

relating the coherent coupling rate (g) to all incoherent losses in the system (κ, γ). Note that C is only proportional to $\mathcal{Q}/V$ – the dipole moment μ cancels out. With this definition, C is connected to the Purcell factor F_{p} [29] via $F_{\mathrm{p}} = 2C$. Equivalently, the β-factor [30], the fraction of emitted photons entering the cavity mode, is defined as

$$\beta = \frac{F_{\mathrm{p}}}{F_{\mathrm{p}} + 1} = \frac{2C}{2C + 1} = \frac{g^2}{g^2 + \kappa\gamma/4}. \tag{1.6}$$

For $C \gg 1$, the β-factor is close to 100%. Neglecting all absorption and scattering losses and assuming a so-called "single-sided" cavity with a perfectly reflecting mirror on one side and a partly reflecting mirror on the other one, the cavity's photon extraction efficiency [31] is given by

$$\eta_{\text{out}} = \frac{\kappa}{\kappa + \gamma}. \tag{1.7}$$

This yields a quantum efficiency [31] of the cavity-QED system of

$$\eta = \beta \cdot \eta_{\text{out}} = \frac{g^2}{g^2 + \kappa\gamma/4} \cdot \frac{\kappa}{\kappa + \gamma}, \tag{1.8}$$

the probability of an exciton producing a photon into the first lens of the optical setup [32]. For a fixed g and γ, the quantum efficiency is maximised for the condition $\kappa = 2g$.

Note that the quantum efficiency is only one side of the coin: once a photon efficiently exits the cavity-QED system, it also has to be collected efficiently into an optical fibre and detected efficiently by a single-photon detector. This makes *plano-concave* cavities that support a Gaussian cavity mode [33] (which can be coupled efficiently to an optical fibre) and *optical* photons (that can be detected very efficiently [34]) highly attractive for the realisation of an efficient single-photon source.

1.1.3 Strong coupling: Jaynes-Cummings model

In the case of $g \gg \kappa, \gamma$ (which implies large $C \gg 1$) the system enters the strong-coupling regime where the coupling strength is so large compared to all decoherence mechanisms that an initially excited atom inside an "empty" cavity (field in vacuum state) is able to reabsorb a spontaneously emitted photon: there is a coherent exchange of a single energy quantum between the atom and the cavity, referred to as "vacuum Rabi-oscillation" [7, 35, 36].

A single quantized (two-level) atom coupled to a single quantized mode of the electromagnetic field can be described via the "standard model" of cavity-QED, the Jaynes-Cummings model [37]. For simplicity, all decoherence mechanisms (see Appendix D where the effects of γ and κ are included) are neglected. At the heart of this model is the Jaynes-Cummings Hamiltonian, which in case of atom-cavity resonance and in the rotating wave approximation (RWA) reads

$$H = \underbrace{\hbar\omega_0 b^\dagger b}_{H_{\text{atom}}} + \underbrace{\hbar\omega_0 a^\dagger a}_{H_{\text{cavity}}} + \underbrace{\hbar g(ab^\dagger + a^\dagger b)}_{H_{\text{interaction}}}, \tag{1.9}$$

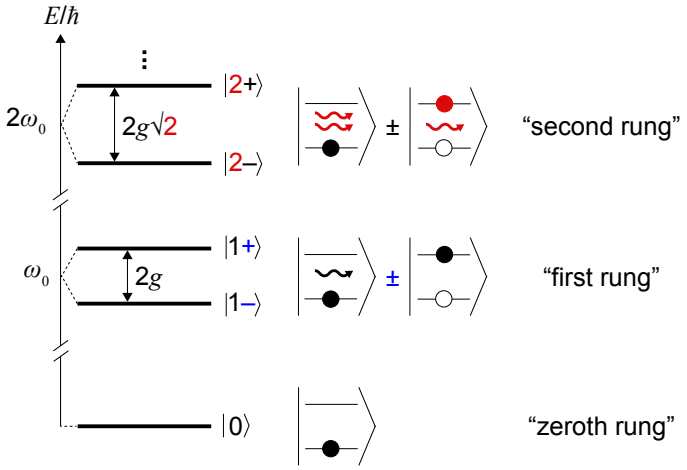

Fig. 1.2. The Jaynes-Cummings ladder. Ground state and the first two "rungs" of the Jaynes-Cummings ladder with energy splittings $2g\sqrt{n}$ (n being the number of excitations in the system).

where ω_0 is the frequency separation of the ground state $|g\rangle$ and excited state $|e\rangle$ of the atom [38]. H_{atom} and H_{cavity} are the Hamiltonians of the uncoupled two-level atom and cavity mode, respectively, and $H_{\text{interaction}}$ is the interaction Hamiltonian. $a^\dagger$ (a) and $b^\dagger$ (b) are the creation (annihilation) operators of a cavity photon and an emitter excitation, respectively (Appendix D).

In the strong-coupling regime, the eigenstates of this Hamiltonian are mixed light-matter states also referred to as dressed states or polaritons,

$$|n\pm\rangle = \frac{|\mathrm{g}, n\rangle \pm |\mathrm{e}, n-1\rangle}{\sqrt{2}}, \tag{1.10}$$

where $n = 1, 2, 3, ...$ is the number of excitations in the system in form of an atomic excitation and/or photons in the light field. The infinite set of eigenstates makes up the Jaynes-Cummings ladder with the nth "rung" (or manifold) consisting of a doublet of eigenstates split by $2\hbar g\sqrt{n}$. Each state is a symmetric or antisymmetric superposition (normalized) of the state $|\mathrm{g}, n\rangle$ (where the atom is in the ground state $|g\rangle$ and n photons are in the cavity) and the state $|\mathrm{e}, n-1\rangle$ (where the atom is excited $|e\rangle$ and $n-1$ photons are in the cavity), see Fig. 1.2.

The anharmonic nature of the Jaynes-Cummings ladder is equivalent to the fact that adding a single photon to the system changes its resonance frequencies. This is a profound nonlinearity and leads to effects such as "photon blockade" [6] where adding a second photon to the system where one photon is already present is forbidden. In other words, the presence of a single photon in the cavity leads to a reflection of an incoming

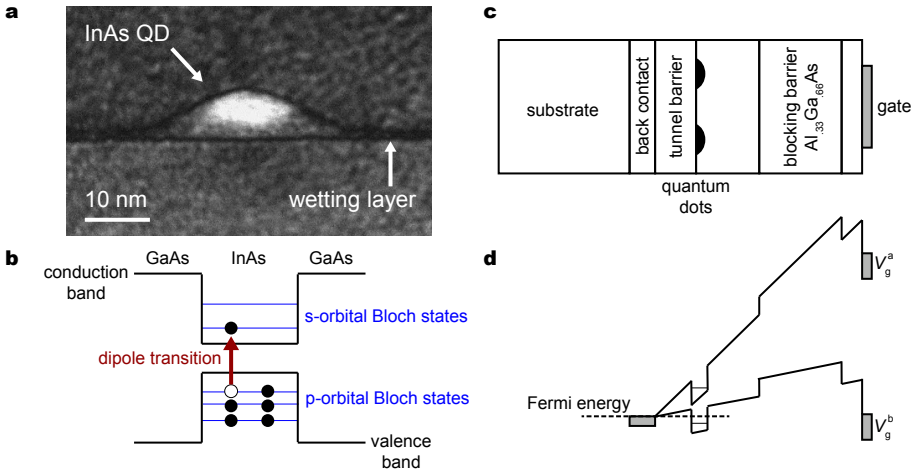

Fig. 1.3. Self-assembled InAs quantum dots. **a**, Dark-field transmission electron microscopy (TEM) image of a self-assembled quantum dot revealing its diameter of $\sim 28\,\mathrm{nm}$ and height of $7.8 \pm 0.5\,\mathrm{nm}$. Courtesy of Jean-Michel Chauveau and Arne Ludwig. **b**, Schematic of the energy level structure of an InAs QD embedded in a GaAs matrix. The small volume of InAs material acts as potential well for electrons and holes, making their allowed energy levels discrete. **c**, Heterostructure presented in Ref. [22] in order to tune the quantum dot energy levels with respect to the Fermi sea of the backgate. **d**, Conduction band edge for two different voltages applied to the top gate. **c** and **d** reproduced and modified from Ref. [22].

second photon of same frequency – photons apparently interact with each other. This is the basis of a "single-photon transistor" [39].

From Eqs. 1.1–1.4, the requirements to enter the strong-coupling regime ($g \gg \kappa, \gamma$) experimentally can be stated: a large dipole moment of the atom as well as a high $\mathcal{Q}$-factor and small mode volume V of the cavity.

1.2 Self-assembled quantum dots

A self-assembled quantum dot is an excellent solid-state emitter of bright and indistiguishable single photons [32, 40–42] and exhibits a large optical dipole moment [21]. An InAs quantum dot is a few nanometers wide "island" of InAs molecules (few tens of thousands) which is formed due to strain during growth of an initial layer of InAs (the wetting layer) via molecular beam epitaxy (MBE) on top of a GaAs host substrate. Due to the three-dimensional confinement of electrons and holes in a small volume with an extension in the order of 10 nm (Fig. 3.4a), the energy levels are quantized so that a single electron-level in the s-shell together with a single hole-level in the s-shell form an effective two-level system. An optical transition between the ground state $|\mathrm{g}\rangle$ and

excited state $|e\rangle$ of this two-level system forms a bound electron-hole pair, an exciton (Fig. 3.4b). An exciton created in an initially empty quantum dot is referred to as neutral exciton, X^0, while one created in a quantum dot already hosting a single electron (hole) is called negatively (positively) charged trion, X^- (X^+).

Embedding the quantum dots in a semiconductor heterostructure with doped layers or a Schottky contact acting as gates (Fig. 3.4c) allows the quantum dot energy levels to be shifted with respect to the Fermi sea of the back-gate (Fig. 3.4d). This enables a single quantum dot to be charged deterministically by adding electrons one-by-one via the Coulomb blockade effect [22]. Also, it allows for fine-tuning of the quantum dot transition frequency via the dc Stark effect. Moreover, embedding the quantum dots within a gated heterostructure has been shown to reduce noise in the quantum dot significantly leading to emission close to the so-called transform limit [40], the minimum emitter linewidth limited by the emitter's radiative decay rate only, $\gamma_R = 1/\tau_R$ (where τ_R is the radiative lifetime).

1.3 Solid-state strong coupling with monolithic microcavities

Strong coupling of a single semiconductor quantum dot to a monolithic microcavity was first observed in 2004 with a micropillar [9] with $(g, \kappa, \gamma)/2\pi \approx (19, 44, 18)\,\mathrm{GHz}$ ($C \approx 0.91$) and with a photonic crystal cavity [10] with $(g, \kappa, \gamma)/2\pi \approx (21, 42, 22)\,\mathrm{GHz}$ ($C \approx 0.95$). In 2005, strong coupling with a microdisk microcavity [17] with $(g, \kappa, \gamma)/2\pi \approx (48, 34, 68)\,\mathrm{GHz}$ ($C \approx 2.0$) was reported.

A micropillar is created from a semiconductor planar cavity with an embedded λ-layer of GaAs forming the cavity layer. The self-assembled QDs are embedded in the center of this λ-layer ensuring maximum coupling strength. A pillar with diameter up to a few microns is formed by etching and leads to a lateral confinement of the photonic mode due to total internal reflection at the pillar walls.

A photonic crystal cavity (PCC) is a lateral waveguide with periodically etched holes and a defect (i.e. one or few missing holes) forming the cavity region with a self-assembled QD in the center. Similar to the existence of an electronic bandgap forming in a semiconductor crystal, a photonic bandgap can thus be formed in a photonic crystal.

A microdisk microcavity [17] is based on whispering gallery modes [43] inside a ring resonator.

Micropillars offer mode volumes in the order of a few $(\lambda/n)^3$ [18–20] and $\mathcal{Q}$-factors typically in the order of a few tens of thousands [18–20], while a high $\mathcal{Q} = 250,000$ was reported in Ref. [44]. The photon extraction efficiency of micropillars is potentially

high [32, 41].

PCCs feature smaller mode volumes below $(\lambda/n)^3$ (which is why they're often called "nanocavities") while exhibiting similar $\mathcal{Q}$-factors to micropillars with a maximum achieved $\mathcal{Q} = 81,000$ in Ref. [36], but require sophisticated photon out-couplers [45] (with limited photon extraction efficiency) in order to allow for vertical out-coupling of photons.

While ultrahigh $\mathcal{Q}$-factors up to $6 \cdot 10^6$ have been reported [43] with microdisk microcavities, high-efficiency out-coupling of single photons is hard to achieve [46] and the mode volume is typically higher than the one of micropillars and PCCs [46].

The entire geometry of a monolithic microcavity is fixed in space, which makes in-situ frequency tuning difficult. Temperature tuning is one of the established techniques, or, alternatively, gas tuning in PCCs that can be used to change the refractive index of holes and thus the cavity's resonance frequency [36]. However, there is a restriction on the temperature tuning range as exciton lines become significantly broadened above temperatures of $T = 30\,\mathrm{K}$ [47]. Also, positioning a single QD in the center of the cavity mode is tough to achieve. Although deterministic methods to position a single quantum dot in the center of the monolithic cavity exist (via advanced in-situ lithography techniques in the case of micropillars for instance [32]), the accuracy is limited to about 50 nm [32] and *in situ* tuning is impossible once the micropillar has been etched.

Also, incorporation of gates in monolithic cavities is tough: in the case of a micropillars for instance, the entire top and bottom mirrors must be heavily doped as electrical contacts are possible only via the outermost layers [32], leading inevitably to free-carrier absorption, thus decreasing the cooperativity and collection efficiency. Gated PCCs exist, however they suffer from considerable leakage currents [48] due to the small thickness ($\sim 200\,\mathrm{nm}$) of the membranes.

Until 2018, cooperativities from monolithic microcavities improved only modestly, see for instance $C \approx 3.3$ [18], $C \approx 4.8$ [19], $C \approx 2.0$ [20] and $C \approx 12$ [14]. In 2018, strong coupling with $C > 100$ [16] was reported with a PCC by exploiting the extremely small mode volume and thus achieving a high coupling strength of $g/2\pi = 40\,\mathrm{GHz}$, however only with one QD (which is non-deterministically positioned), moderate $\mathcal{Q} \sim 8 \cdot 10^4$ (still: record-high for QD cavity-QED studies with PCCs according to Ref. [16]) and spectra suffering from "cavity-feeding" due to charge noise. Cavity-feeding is the observation of scattering from the bare cavity mode even at the QD-cavity resonance that has complicated quantum-dot cavity-QED at optical frequencies in the past [11, 12, 14–16, 36, 49].

1.4 Tunable microcavity with gated InAs quantum dots

A plano-concave Fabry-Pérot cavity consisting of two individual mirrors – one planar, one curved with radius R – separated by a distance L_{vac} (the vacuum-gap) has several advantages. First, both mirrors (often distributed Bragg reflectors, DBRs) can be placed with respect to each other in all three dimensions. This enables any quantum emitter embedded in the planar mirror to be brought into resonance with the microcavity by frequency tuning (via the cavity length) and spatial tuning (via lateral positioning of the planar mirror). Secondly, a stable cavity mode is rather simple to achieve once the stability criterion $L_{\mathrm{vac}} < R$ for a stable cavity mode is fulfilled [33]. Thirdly, the photonic mode confined by a plano-concave cavity is close to a simple Gaussian [33] making this system extremely attractive for efficient single-photon extraction into an optical fibre. Fourthly, the device doesn't require any temperature tuning – it can be operated at a constant temperature of 4.2 K where exciton-linewidths are small [47]. Last but not least, tunable microcavities do not require etching close to the quantum dot itself, which minimizes scattering losses.

Reported realisations so far involved a planar semiconductor DBR with embedded QDs [49, 50] or a planar dielectric DBR with a GaAs or diamond membrane on top containing QDs [51] or NV centers [26]. In all these experiments, a choice for the curved mirror has been a fused silica substrate [52, 53] or the end facet of an optical fibre [50], CO_2-laser ablated [54] to produce atomically smooth indentations (or "craters") with curvature radii R down to 13 μm [49].

An issue with fibre microcavities is the limited mode-matching between the cavity mode and guided mode of the fibre. Open microcavities however allow for an excellent mode-matching [53] due to the fact that the numerical aperture (NA) of the objective lens can be chosen independently of the top mirror curvature.

Compared to monolithic microcavities, tunable microcavities offer similar (Appendix C) or slightly higher [53] mode volumes than micropillars, while the $\mathcal{Q}$-factors can potentially be much higher due to the fact that etching is not required: the lateral extent of the cavity mode, the beam waist w_0, is simply given by the curvature R of the top mirror and the geometrical cavity length L_{geom}* [33, 53],

$$w_0 = \sqrt{\frac{\lambda_0}{\pi}}\Big(RL_{\mathrm{geom}} - L_{\mathrm{geom}}^2\Big)^{1/4}. \tag{1.11}$$

*Note that the geometrical cavity length L_{geom} depends on the vacuum-gap as well as the energy penetration depth into the top and bottom DBR.

Embedding gates in a tunable microcavity has already been proposed in Ref. [49] in order to reduce spectral wandering in self-assembled QDs and thus eliminate cavity-feeding. Due to the large lateral extent of the gated layers (compared to a micropillar for instance) in a semiconductor heterostructure, even very thin doped layers on the order of 10 nm can be contacted – no gradual doping across the entire microcavity as in the case of micropillars is needed.

To summarise, the usage of a tunable microcavity together with gated InAs quantum dots is a highly promising cavity-QED system to achieve a coherent atom-photon interface in the solid-state at optical frequencies with an excellent photon extraction efficiency.

Chapter 2

Strong coupling of a charge-tunable quantum dot to an optical microcavity

Adapted from:

Daniel Najer[1], Immo Söllner[1], Pavel Sekatski[1], Vincent Dolique[3], Matthias C. Löbl[1], Daniel Riedel[1], Rüdiger Schott[2], Sebastian Starosielec[1], Sascha R. Valentin[2], Andreas D. Wieck[2], Nicolas Sangouard[1], Arne Ludwig[2], and Richard J. Warburton[1],

"A gated quantum dot far in the strong-coupling regime of cavity-QED at optical frequencies",
arXiv:1812.08662 (2018).

[1]Department of Physics, University of Basel, Klingelbergstrasse 82, CH-4056 Basel, Switzerland
[2]Lehrstuhl für Angewandte Festkörperphysik, Ruhr-Universität Bochum, D-44780 Bochum, Germany
[3]Laboratoire des Matériaux Avancés (LMA), IN2P3/CNRS, Université de Lyon, F-69622 Villeurbanne, Lyon, France

2.1 Summary

The strong-coupling regime of cavity-quantum-electrodynamics (cQED) represents the light-matter interaction at the fully quantum level. Adding a single photon shifts the resonance frequencies, a profound nonlinearity. cQED is a test-bed of quantum optics [5–7] and the basis of photon-photon and atom-atom entangling gates [3, 55]. At microwave frequencies, success in cQED has had a transformative effect [56]. At optical frequencies, the gates are potentially much faster; the photons can propagate over long distances and can be detected easily. Following pioneering work on single atoms [5–8],

solid-state implementations using semiconductor quantum dots are emerging [9–16]. We present here a gated, ultralow-loss microcavity-device. The gates allow both the quantum dot charge and resonance frequency to be controlled electrically; crucially, they allow cavity-feeding [11, 12, 14–16, 36, 49] to be eliminated. Even in the microcavity, the quantum dot has a linewidth close to the radiative limit. In addition to a very pronounced avoided-crossing in the spectral domain, we observe a clear coherent exchange of a single energy-quantum between the "atom" and cavity in the time domain (vacuum Rabi-oscillations). Decoherence arises predominantly via the atom and photon loss-channels. The coherence is exploited to probe the transitions between the singly- and doubly-excited photon-atom system via photon-statistics spectroscopy [57]. We propose this system as a platform for quantum technology.

2.2 Introduction

A resonant, low-loss, low-volume cavity boosts massively the light-matter interaction such that cavity-QED can potentially provide a highly coherent interface between single photons and single atoms. The metric for the coherence is the cooperativity, the ratio of the coherent coupling squared to the loss rates, $C = 2g^2/(\kappa\gamma)$ (g is the coherent photon-atom coupling, κ the cavity loss rate, γ the decay rate of the atom into non-cavity modes). The potential for achieving a high cooperativity gives cavity-QED a central role in the development of high-fidelity quantum gates.

In the microwave domain, a transmon "atom" exhibits strong coupling to a cavity photon [56] and this facilitates remote transmon-transmon coupling via a virtual photon. Recently, the transmon was replaced with a semiconductor quantum dot (QD), and a coupling between a microwave photon and both charge- [58] and spin-qubits [59–61] was observed. In contrast to microwave photons, optical frequency photons can carry quantum information over very large distances and therefore play an indispensable role in quantum communication. Creating an optical photon-photon gate depends critically on a high-C photon-atom interface along with efficient photonic engineering [3]. Cavity-QED can potentially achieve both simultaneously. Translating these concepts to the solid-state is important for developing on-chip quantum technology. The most promising solid-state "atom" is a self-assembled semiconductor QD: an InGaAs QD in a GaAs host is a bright and fast emitter of highly indistinguishable photons [32, 41], and a QD spin provides the resource required for atom-photon and photon-photon gates. However, a low-noise, high-C, high-efficiency single photon-single QD interface does not yet exist.

2.3 Challenges

In QD cavity-QED, one key problem is the almost ubiquitous observation of scattering from the bare cavity even at the QD-cavity resonance [11, 12, 14–16, 36, 49]. This "cavity-feeding" is the manifestation of complex noise processes in the semiconductor host [12]. Another key problem is the trade-off between coupling g and the loss rates κ and γ: as the devices, for instance micropillar [9, 32] or photonic-crystal cavities [10–12, 14–16], are made smaller in an attempt to boost g, both κ and γ tend to increase. The increase in κ, reflecting a deterioration in the quality-factor ($\mathcal{Q}$-factor) of the microcavity, arises on account of increased scattering and absorption; the increase in γ reflects an inhomogeneous broadening in the emitter frequency. The increase in the loss rates is only partly a consequence of fabrication imperfections. An additional factor is the GaAs surface which pins the Fermi energy mid-gap resulting in surface-related absorption [43] and charge-noise.

2.4 Our solution

We present here a resolution to these conundrums. The QD exhibits close-to-transform limited linewidths even in the microcavity; the microcavity has an ultrahigh $\mathcal{Q}$-factor yet small mode volume. The QD exciton is far in the strong-coupling regime of cavity-QED ($g \gg \kappa$, $g \gg \gamma$). Strong coupling is achieved on both neutral and charged excitons in the same QD by tuning both the QD-charge and the microcavity frequency *in situ*. The output is close to a simple Gaussian beam. We achieve a cooperativity of $C = 150$, higher than that achieved with cold-atom experiments [7] and comparable to state-of-the-art QD photonic-crystal cavities [16] but crucially here, cavity-feeding is eliminated and other sources of noise are very weak. Equivalently, the β-factor, the probability of the excited atom emitting into the cavity mode, is as high as 99.7%. The coherence of the coupled QD-cavity system is demonstrated most forcefully by the observation of a very clear atom-photon exchange in the time domain (a vacuum Rabi-oscillation).

Design of the QD-microcavity was guided by three principles. First and foremost, a self-assembled QD benefits enormously from electrical control via the conducting gates of a diode structure. A gated QD in high quality material gives close-to-transform-limited linewidths [40], control over both the optical frequency via the Stark effect and the QD charge state via Coulomb blockade [63]. We therefore include electrical gates in the cavity device. This is non-trivial. The gates themselves, n-doped and p-doped regions in the semiconductor, absorb light via free-carrier absorption – they are not obviously

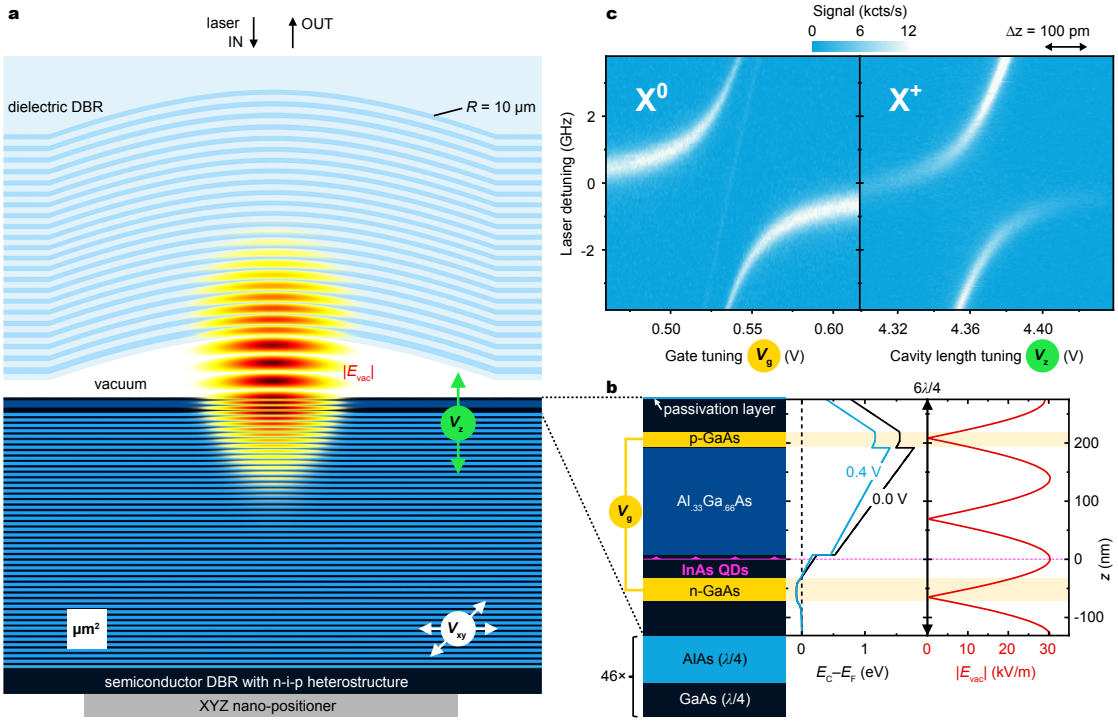

Fig. 2.1. Gated quantum dot in a tunable microcavity: design and realisation. a, Simulation of the vacuum electric field $|E_{\rm vac}|$ in the microcavity (image to scale). The bottom mirror is a distributed Bragg reflector (DBR) consisting of 46 AlAs($\lambda/4$)/GaAs($\lambda/4$) pairs. (λ refers to the wavelength in each material.) The top mirror is fabricated in a silica substrate [52, 54]. It has radius of curvature $R = 10\,\mu$m and consists of 22 silica($\lambda/4$)/tantala($\lambda/4$) pairs. The layer of quantum dots (QDs) is located at the vacuum field anti-node one wavelength beneath the surface. The vacuum-gap has the dimension of $3\lambda/2$. $V_{\rm xy}$ ($V_{\rm z}$) controls the lateral (vertical) position of the QD with respect to the fixed top mirror. **b**, The top part of the semiconductor heterostructure. A voltage $V_{\rm g}$ is applied across the n-i-p diode. $V_{\rm g}$ controls the QD-charge via Coulomb blockade and within a Coulomb blockade plateau the exact QD optical frequency via the dc Stark effect. Free-carrier absorption in the p-layer [62] is minimised by positioning it at a node of the vacuum field. A passivation layer suppresses surface-related absorption [43]. **c**, Laser detuning ($\Delta_{\rm L}$) versus cavity detuning ($\Delta_{\rm C}$) of a neutral QD exciton (X^0) and a positively-charged exciton (X^+) in one and the same QD. Cavity detuning is achieved by tuning the QD at fixed microcavity frequency (X^0); and by tuning the microcavity frequency at fixed QD frequency (X^+). For X^0, the weak signal close to the bare microcavity frequency arises from weak coupling to the other orthogonally-polarised X^0 transition – it does not arise from cavity-feeding (see Supplementary III.E). Data in **c** from QD1 at $B = 0.00\,$T.

compatible with a high-$\mathcal{Q}$-factor cavity. Also, the gates inevitably create electric fields in the device resulting in absorption via the Franz-Keldysh mechanism. Secondly, in order to achieve narrow QD linewidths in the cavity, we minimise the area of the free GaAs surface in order to reduce surface-related noise. Finally, we include a mechanism

for *in situ* tuning the cavity, both in frequency and in lateral position, to allow a full exploration of the parameter space.

We employ a miniaturised Fabry-Pérot cavity consisting of a semiconductor heterostructure and external top mirror (Fig. 2.1a, Section 3.2–3.3). The heterostructure has an n-i-p design with the QDs in the intrinsic (i) region (Fig. 2.1b, Section 3.1). The QDs are located at an antinode of the vacuum field (see Appendix C for details on the microcavity simulation); the p-layer is located at the node of the photon field in the microcavity in order to minimise free-carrier absorption from the mobile holes [62] (Fig. 2.1a). Mobile electrons absorb considerably less than mobile holes [62] such that it is not imperative to place the n-doping at a node of the vacuum field. The n-layer begins 25 nm "below" the QDs such that the QDs are in tunnel-contact with the Fermi sea in the n-layer: the QDs are in the Coulomb blockade regime. The n- and p-layers are separately contacted. The bottom mirror is a highly reflective semiconductor mirror (a distributed Bragg reflector, DBR); the top mirror consists of a $10\,\mu$m-radius crater micro-machined into a fused silica substrate [54], subsequently coated with a highly reflective dielectric DBR. The position of the contacted sample is controlled *in situ* with respect to the top mirror. We find that surface-related absorption limits the $\mathcal{Q}$-factor to $2.0 \cdot 10^4$ – this represented a major problem in the development of this device. We found a way to solve it: the GaAs surface is passivated with a process that replaces the native oxide with a few-nm thick alumina layer [43]. With surface passivation, the fully-contacted device has a $\mathcal{Q}$-factor close to 10^6. The mode volume is $1.4\lambda_0^3$ (Appendix C.3), where λ_0 is the free-space wavelength.

2.5 Cooperativity via resonant spectroscopy

We excite the QD–microcavity system with a resonant laser (continuous-wave), initially with an average photon-occupation much less than one ($\langle n \rangle \simeq 0.05$), and detect the scattered photons, rejecting directly reflected laser-light with a polarisation-based dark-field technique [40, 64]. The fundamental microcavity mode splits into two, separated by 32 GHz, predominantly on account of a weak birefringence in the semiconductor DBR; each mode is linearly polarised. The neutral exciton also splits into a linearly-polarised doublet, X^0_a and X^0_b, via the fine-structure splitting (FSS). QDs are chosen for which the microcavity and X^0 axes are closely aligned. The FSS varies from QD to QD and can be small enough that both X^0_a and X^0_b couple to the same microcavity mode, one strongly, one weakly. In such cases, e.g. QD1 (Fig. 2.2h), this complication can be avoided by applying a magnetic field which pushes X^0_a and X^0_b apart via the Zeeman

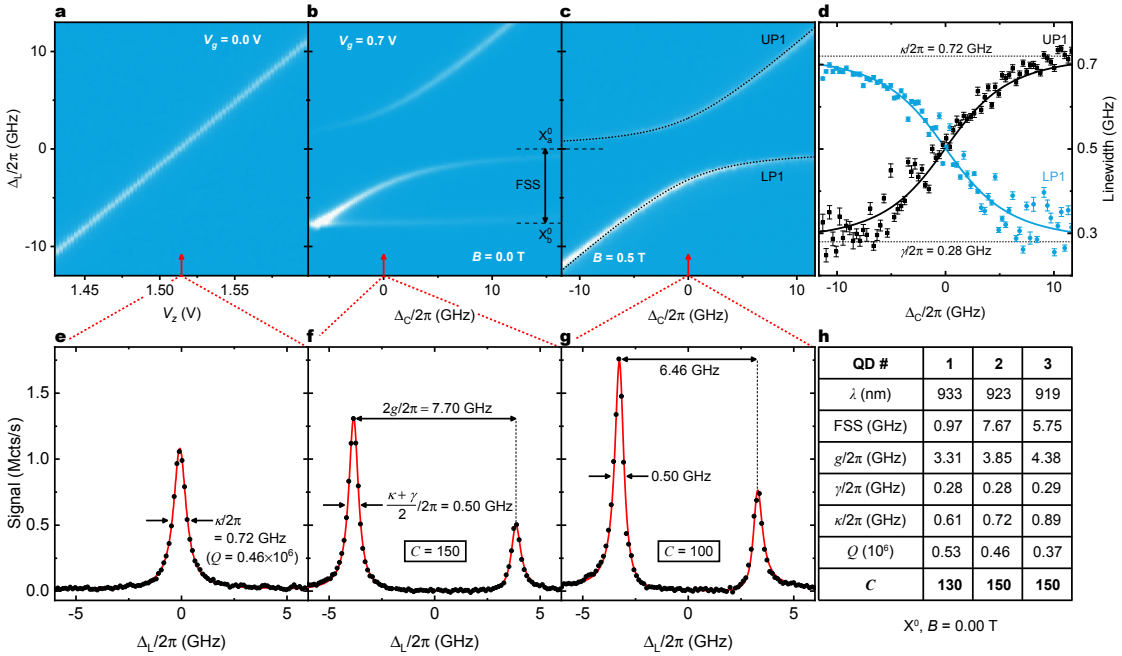

QD #	1	2	3
λ (nm)	933	923	919
FSS (GHz)	0.97	7.67	5.75
$g/2\pi$ (GHz)	3.31	3.85	4.38
$\gamma/2\pi$ (GHz)	0.28	0.28	0.29
$\kappa/2\pi$ (GHz)	0.61	0.72	0.89
Q (10^6)	0.53	0.46	0.37
C	130	150	150

Fig. 2.2. Strong coupling of a QD exciton in the microcavity. The spectra were recorded by measuring the photons scattered by the microcavity–QD system at a temperature of 4.2 K, rejecting reflected laser light with a polarisation-based dark-field technique [40, 64]. Data shown here were taken on the X^0 transition. **a**, **e**, Signal with QD far-detuned from microcavity in order to determine the photon loss-rate κ, equivalently the quality factor $\mathcal{Q}$. **b**, **f**, X^0 at magnetic field $B = 0.00$ T showing strong coupling to one fine-structure-split (FSS) transition, weak coupling to the other (there is an almost perfect alignment of the X^0 and microcavity axes). From the spectra, we determine g, κ, γ and C (as defined in the main text). **c**, **d**, **g**, X^0 at $B = 0.50$ T: the magnetic field increases the FSS. C is smaller than at $B = 0.00$ T because the X^0 transitions become circularly polarised and couple less strongly to the linear-polarised microcavity mode. The simple avoided-crossing in **c** enables a determination of κ and γ by using data at all values of Δ_C. The dotted lines in **c** and solid lines in **d**–**g** are fits to a solution of the Jaynes-Cummings Hamiltonian in the limit of very small average photon occupation [49]. **h**, Summary of strong-coupling parameters recorded on X^0 at $B = 0.00$ T on three separate QDs using the same microcavity mode. $C > 100$ in all three cases. Data in **a**–**g** from X^0 in QD2.

effect. Alternatively, the charged exciton X^+ can be probed which has just one optical resonance at zero magnetic field.

When the microcavity and QD optical frequency come into resonance, we observe a clear avoided crossing in the spectral response (Fig. 2.1c) signifying strong coupling. We achieve strong coupling on different charge states in the same QD (Fig. 2.1c), also on many different QDs (Fig. 2.2h and Section 3.5–3.6). The cavity-emitter detuning is controlled *in situ* either by tuning the QD (voltage V_g) or by tuning the microcavity (voltage V_z) (Fig. 2.1c).

At the QD-cavity resonance, mixed states form, the polaritons. In between the lower- and upper-polaritons (LP1 and UP1, respectively), there is no trace of the bare microcavity mode (Fig. 2.2f,g). These results demonstrate that cavity-feeding has been eliminated. This is a consequence of the electrical control via the gates. The high doping in the back contact creates a Fermi sea and determines the Fermi energy. Each QD is in tunnel-contact with the Fermi sea and operates in the Coulomb blockade regime such that the QD is always in the charge state which couples to the microcavity mode. (A change of charge state detunes the QD from the microcavity mode leading to scattering from the bare microcavity mode.) Additionally, states higher in energy than the QD states are not occupied. Population of the wetting-layer states for instance leads to charge noise but this is highly suppressed with the gated device under resonant excitation. Furthermore, phonon-assisted excitation of off-resonant QDs is clearly negligible.

A full spectral analysis determines the parameters g, κ and γ (Fig. 2.2). $\gamma/2\pi = 0.28$ GHz (Fig. 2.2). The transform-limit for these QDs is 0.30 ± 0.05 GHz, the uncertainty accounting for QD-to-QD fluctuations [65]. The measured γ, 0.28 GHz, corresponds to the ideal limit to within the uncertainties of $10-20\%$. The linewidths in the microcavity match the best QD linewidths ever reported [40]. The coupling g lies in the GHz regime pointing to potentially very fast quantum-operations. g corresponds closely to that expected based on the geometry of the device (Fig. 2.1b and Appendix C.2) and the QD optical dipole. For QD2 at zero magnetic field, $g/\gamma = 14$, $g/\kappa = 5.3$ corresponding to a cooperativity $C = 2g^2/(\kappa\gamma) = 150$. Equivalently, the β-factor [66] is $\beta = 2C/(2C+1) = 99.7\%$. A high cooperativity is achieved on all QDs within the spectral window of the microcavity (Fig. 2.2h).

2.6 Time-resolved vacuum Rabi-oscillations via $g^{(2)}(\tau)$

To probe the coherence of the coupled photon-exciton system, we look for a photon-atom exchange, i.e. a "vacuum Rabi-oscillation" [7, 35, 36]. We drive the system at a frequency positively detuned from the lower-frequency polariton (LP1) and record the two-photon autocorrelation $g^{(2)}(\tau)$ without spectral filtering (Fig. 2.3). All photons in the detection channel contribute: $g^{(2)}(\tau)$ is recorded without spectral filtering. Coherent oscillations are observed as a function of delay whose period, 220 ps, corresponds exactly to 2π divided by the measured frequency splitting of the polaritons at this cavity detuning (Section 3.6.2). These oscillations can be understood in terms of the Jaynes-Cummings ladder (Fig. 2.3 inset). The laser drives weakly the two-photon transition $|0\rangle \leftrightarrow |2-\rangle$. $|2-\rangle$ decays by emitting two photons. Detection of the first photon leaves the system in

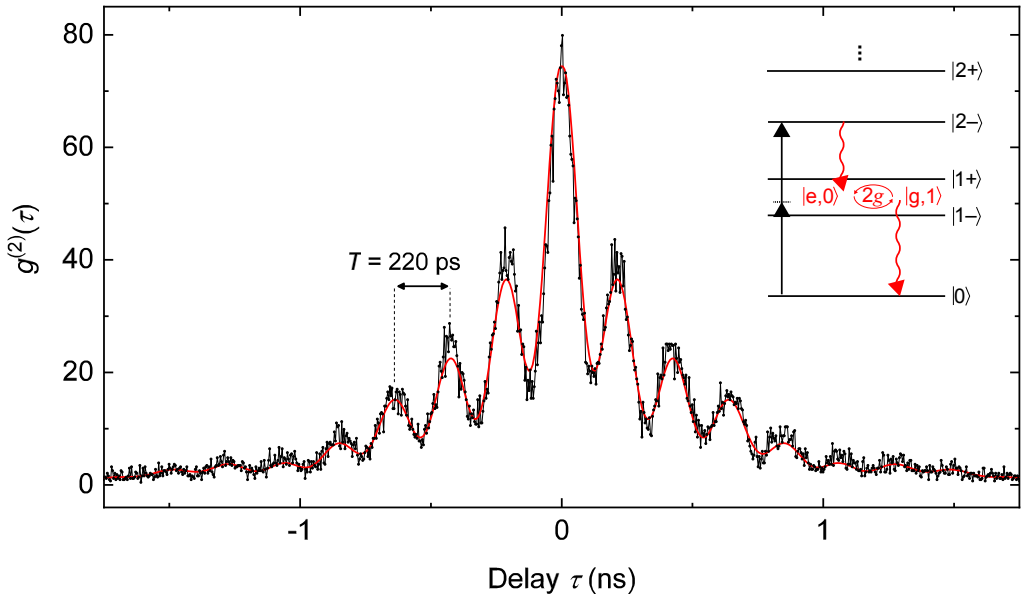

Fig. 2.3. Time-resolved vacuum Rabi-oscillations. Intensity autocorrelation function $g^{(2)}(\tau)$ as a function of delay τ for $\Delta_C = 0.73g$ (detuned via cavity length) and $\Delta_L = -0.13g$. The inset shows the first few rungs of the Jaynes-Cummings ladder. The laser drives a two-photon transition $|0\rangle \leftrightarrow |2-\rangle$. The solid red line is the result of calculating $g^{(2)}(\tau)$ from the Jaynes-Cummings Hamiltonian using g, κ and γ from the spectroscopy experiments (Fig. 2.2) and Rabi coupling $\Omega/2\pi = 0.16$ GHz. Data from X^0 in QD1 at $B = 0.40$ T.

a superposition of the eigenstates $|1-\rangle$ and $|1+\rangle$ such that a quantum beat takes place. Detection of the second photon projects the system into the ground state $|0\rangle$, stopping the quantum beat (Supplementary section V in Ref. [67]). The large $g^{(2)}(0)$ (80 in this particular experiment) is confirmation that the photon states with quanta $n \geq 2$ are preferentially scattered [11, 14].

The measured $g^{(2)}(\tau)$ is fully described with a numerical solution of the Jaynes-Cummings model: the standard Hamiltonian along with the parameters determined by the spectroscopy experiments (Appendix D) gives excellent agreement with the experimental result (Fig. 2.3). The vacuum Rabi-oscillations are sensitive to decoherence, not just the loss processes but also pure dephasing of the emitter. Including pure dephasing into the theory improves slightly the quantitative description of $g^{(2)}(\tau)$: the pure dephasing rate is $(10 \pm 2)\%$ of the measured linewidth (see Appendix D.4.2).

The photon statistics change a lot as a function of both laser detuning Δ_L and cavity detuning Δ_C (both defined with respect to the bare exciton) [68]. For $\Delta_C = 0$, $g^{(2)}(0)$ is highly bunched at the two-photon resonance, $\Delta_L = -g/\sqrt{2}$ (Fig. 2.4b), yet highly anti-bunched at the single-photon resonance, $\Delta_L = -g$ (Fig. 2.4c). The anti-bunching

is a demonstration of photon blockade in this system. On driving $|0\rangle \leftrightarrow |1-\rangle$, $g^{(2)}(0)$ is limited by the weak two-photon resonance to the $|2-\rangle$ state. The weak population of $|2-\rangle$ (which decays by a two-photon cascade) increases $g^{(2)}(0)$. This interpretation is confirmed by the weak oscillations in $g^{(2)}(\tau)$ (Fig. 2.4c) which arise from a quantum beat between $|1-\rangle$ and $|1+\rangle$, an oscillation which is established on decay of the $|2-\rangle$. Further confirmation of this interpretation is provided by QD3 for which g is larger. This increases the detuning of the two-photon transition and thereby weakens it. For QD3, we find a lower value of $g^{(2)}(0)$, $g^{(2)}(0) = 0.09$ (Appendix A). The Jaynes-Cummings model reproduces the $g^{(2)}(\tau)$ at photon blockade, both $g^{(2)}(0)$ and the fast oscillations.

The full dependence of $g^{(2)}(0)$ on Δ_{L} is plotted in Fig. 2.4e. In principle, $g^{(2)}(0)$ rises to extremely high values [6] as $\Delta_{\mathrm{L}} \to 0$. In practice, the scattered signal becomes weaker and weaker as $\Delta_{\mathrm{L}} \to 0$ such that $g^{(2)}(0)$ reaches a peak and is then pulled down by the poissonian statistics of the small leakage of laser light into the detector channel (Fig. 2.4e). $g^{(2)}(\tau)$ is a rich function: its Fourier transform shows in general three peaks (Fig. 2.4d). The dependence on Δ_{L} shows that these frequencies correspond to $2g$ (see Supplementary section V.D.3 in Ref. [67]), $|g - \Delta_{\mathrm{L}}|$ and $|g + \Delta_{\mathrm{L}}|$ (Fig. 2.4g). All this complexity is described by the Jaynes-Cummings model which, taking only the parameters determined by the spectroscopy experiments as input (Appendix D), gives excellent agreement with the experimental $g^{(2)}(\tau)$ in all respects (Fig. 2.3, Fig. 2.4 and Section 3.5–3.6).

2.7 Up the Jaynes-Cummings ladder

As the laser power increases, there is a spectral resonance at the first- to second-rung transitions, LP2 and UP2; and, at the highest powers, a strong resonance at $\Delta_{\mathrm{L}} = 0$ (Fig. 2.4a): this too is in precise agreement with the predictions of the Jaynes-Cummings model (Fig. 2.4a), and reflects the bosonic enhancement of the transitions between the higher lying rungs of the Jaynes-Cummings ladder. At the highest powers, $\langle n \rangle \simeq 1.7$ on driving LP1 or UP1, increasing to $\langle n \rangle \simeq 16$ on driving at the bare cavity frequency. This experiment provides an opportunity to measure the quantum efficiency of the system. Given the success of the Jaynes-Cummings model, we can calculate at each laser power the decay rate through the top mirror and hence the expected signal (Section 3.6.4). The quantum efficiency of the entire system, i.e. from an exciton in the QD to a "click" on the detector, is 8.6%. Significantly, of those photons exiting the top mirror and passing through the dark-field optics, almost all ($\sim 94\%$) make their way into the collection fibre (Section 3.7). This represents an experimental demonstration that the microcavity

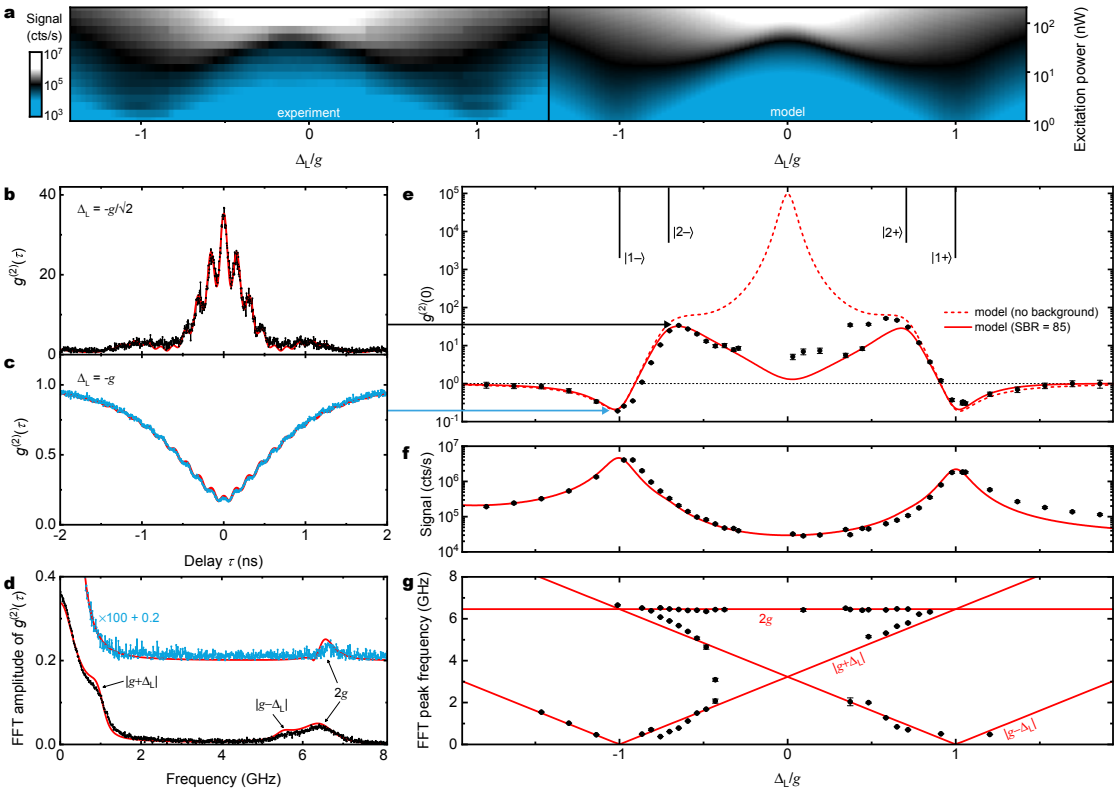

Fig. 2.4. Strong coupling versus driving frequency and power. **a**, Signal versus Δ_L for $\Delta_C = 0$. At low power, LP1 and UP1 are clearly observed. As the power increases, the higher rungs of the Jaynes-Cummings ladder are populated. **b**, $g^{(2)}(\tau)$ for $\Delta_C = 0$ and $\Delta_L = -g/\sqrt{2}$. **c**, $g^{(2)}(\tau)$ for $\Delta_C = 0$ and $\Delta_L = -g$. **d**, Fast Fourier transform (FFT) of $g^{(2)}(\tau)$ in **b** and **c**. **e**, **f**, **g**, $g^{(2)}(0)$, signal and FFT peak frequency of $g^{(2)}(\tau)$ versus Δ_L for $\Delta_C = 0$. The solid red lines in **b**–**g** ("model" in **a**) result from a calculation of $g^{(2)}(\tau)$ (signal) from the Jaynes-Cummings Hamiltonian using g, κ and γ from the spectroscopy experiments, Fig. 2.2. The Rabi coupling is $\Omega/2\pi = 0.07$–0.11 GHz (0.14–1.90 GHz). A signal-to-background ratio SBR = 85 (20) was included. In **e**, the dashed red line shows the theoretical limit without the laser background. Data in **a** from X^+ in QD1 at $B = 0.00$ T; data in **b**–**g** from X^0 in QD2 at $B = 0.50$ T.

output is close to a simple Gaussian beam.

2.8 Photon-statistics spectroscopy

In the experiments with a single laser, the second rung of the Jaynes-Cummings ladder is accessed by tuning the laser to a two-photon resonance (Fig. 2.4b). An alternative is to drive the system with two lasers in a pump-probe scheme. The strong transitions arise from the symmetric-to-symmetric and antisymmetric-to-antisymmetric couplings,

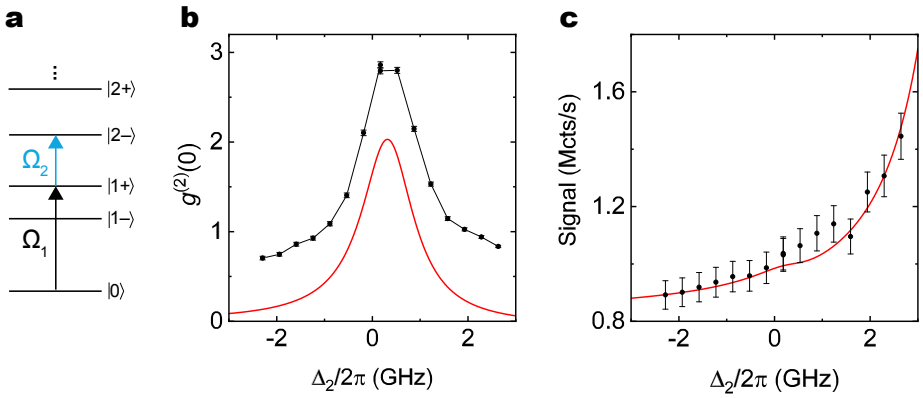

Fig. 2.5. Photon-statistics spectroscopy. **a**, Laser 1 is on resonance with the $|0\rangle \leftrightarrow |1+\rangle$ transition (black arrow, detuning $\Delta_1 = 0$); laser 2 is scanned across the $|1+\rangle \leftrightarrow |2-\rangle$ transition (blue arrow, detuning Δ_2). **b**, $g^{(2)}(0)$ versus Δ_2 showing a pronounced resonance at $\Delta_2 = 3\Delta_C/2 - \Delta_1$. The red solid line is the result of an analytical calculation based on the Jaynes-Cummings Hamiltonian (Appendix D) with Rabi couplings $\Omega_1/2\pi = 0.05$ GHz and $\Omega_2/2\pi = 0.45$ GHz. The offset in the experimental data with respect to the theory reflects additional coincidences arising from off-resonant, two-photon absorptions not included in the model. **c**, Signal versus Δ_2. The signal increases with increasing Δ_2 due to off-resonant driving of the $|0\rangle \leftrightarrow |1-\rangle$ transition by laser 2. All data for X^0 in QD2 at $B = 0.50$ T; $\Delta_C/2\pi = 0.31$ GHz, $\Delta_1/2\pi = 0.17$ GHz.

e.g. $|1-\rangle \leftrightarrow |2-\rangle$ and $|1+\rangle \leftrightarrow |2+\rangle$, which lead to measurable changes in the populations of the states [56]. We employ an alternative here, photon-statistics spectroscopy, implementing a theoretical proposal for the first time [57]. We present this experiment on the symmetric-to-asymmetric $|1+\rangle \leftrightarrow |2-\rangle$ transition. The square of the matrix element is just 3% of that associated with the $|1+\rangle \leftrightarrow |2+\rangle$ transition. A pump laser drives the $|0\rangle \leftrightarrow |1+\rangle$ transition on resonance, and a probe laser, highly red-detuned with respect to the pump, is scanned in frequency in an attempt to locate the $|1+\rangle \leftrightarrow |2-\rangle$ transition (Fig. 2.5a). There is no resonance in the scattered intensity (Fig. 2.5c): any resonance lies in the noise (a few per cent). However, there is a clear resonance in $g^{(2)}(0)$ at exactly the expected frequency $\Delta_2 = 3\Delta_C/2 - \Delta_1$ (Fig. 2.5b): at the weak $|1+\rangle \leftrightarrow |2-\rangle$ transition the number of scattered photons hardly changes but there are profound changes in their statistical correlations. Again, the Jaynes-Cummings model describes the experiment (Fig. 2.5b,c). Here, a short-time expansion in a truncated Hilbert space (first two rungs of the Jaynes-Cummings ladder) is used to calculate $g^{(2)}(0)$ (Appendix D).

Chapter 3

System design and further characterisation

Adapted from:
Daniel Najer[1], Immo Söllner[1], Pavel Sekatski[1], Vincent Dolique[3], Matthias C. Löbl[1], Daniel Riedel[1], Rüdiger Schott[2], Sebastian Starosielec[1], Sascha R. Valentin[2], Andreas D. Wieck[2], Nicolas Sangouard[1], Arne Ludwig[2], and Richard J. Warburton[1],
"A gated quantum dot far in the strong-coupling regime of cavity-QED at optical frequencies" (Supplementary Information),
arXiv:1812.08662 (2018).

[1]Department of Physics, University of Basel, Klingelbergstrasse 82, CH-4056 Basel, Switzerland
[2]Lehrstuhl für Angewandte Festkörperphysik, Ruhr-Universität Bochum, D-44780 Bochum, Germany
[3]Laboratoire des Matériaux Avancés (LMA), IN2P3/CNRS, Université de Lyon, F-69622 Villeurbanne, Lyon, France

3.1 Semiconductor heterostructure

3.1.1 Design and growth

The heterostructure is grown by molecular beam epitaxy (MBE). It consists of an n-i-p diode with embedded self-assembled InAs quantum dots grown on top of an AlAs/GaAs distributed Bragg reflector (DBR) with nominal (measured) centre wavelength of 940 nm (920 nm).

The growth on a (100)-oriented GaAs wafer is initiated by a quarter-wave layer (QWL) of an AlAs/GaAs short-period superlattice (SPS, 18 periods of 2.0 nm GaAs and 2.0 nm AlAs) for stress-relief and surface-smoothing. The growth continues with 46 pairs of

GaAs (67.9 nm) and AlAs (80.6 nm) QWLs forming the "bottom" DBR. The active part of the device consists of a QWL of GaAs (69.8 nm) followed by a 41.0 nm thick layer of Si-doped GaAs (n^+, $2 \cdot 10^{18}\,cm^{-3}$), the back-gate. 25.0 nm of undoped GaAs, the tunnel barrier, is subsequently grown, after which InAs quantum dots are self-assembled using the Stranski-Krastanow process and a flushing-step [69] to blue-shift the quantum dot emission. The layer thicknesses are such that the quantum dots are located at an antinode of the vacuum electric field. The quantum dots are capped with an 8.0 nm layer of GaAs. The growth proceeds with an $Al_{.33}Ga_{.66}As$ layer (190.4 nm), a blocking barrier to reduce the current flow through the diode structure. The heterostructure is completed by 25.0 nm C-doped GaAs (5.0 nm p^+, $2 \cdot 10^{18}\,cm^{-3}$ and 20.0 nm p^{++}, $1 \cdot 10^{19}\,cm^{-3}$), the top-gate, and, finally, a 54.6 nm GaAs capping layer. The heterostructure is shown in Fig. 3.1.

The top-gate is centred around a node of the standing wave of the vacuum electric field in order to minimise free-carrier absorption from the p-doped GaAs. A condition on the tunnel barrier thickness (it is typically $\lesssim 40$ nm thick to achieve a non-negligible tunnel coupling with the Fermi sea) prevents the back-gate being positioned likewise at a vacuum field node. However, the free-carrier absorption of n^+-GaAs is much smaller than that of p^{++}-GaAs at a photon energy of 1.3 eV ($\alpha \approx 10\,cm^{-1}$ for n^+-GaAs compared to $\alpha \approx 70\,cm^{-1}$ for p^{++}-GaAs [62]). We exploit the weak free-carrier absorption of n^+-GaAs and use a standard 25 nm thick tunnel barrier. The back-gate is thus positioned close to the node of the vacuum electric field but is not centred around the node itself.

3.1.2 Electrical contacts and surface passivation

After growth, individual $2.5 \times 3.0\,mm^2$ pieces are cleaved from the wafer. The quantum-dot density decreases from $\sim 10^{10}$ cm^{-2} to zero in an approximately centimetre-wide stripe across the wafer. The sample used in these experiments was taken from this stripe and has a density of 7×10^6 cm^{-2}. (The quantum-dot density was measured by photoluminescence imaging.)

Separate ohmic contacts are made to the n^+ and p^{++} layers; a passivation layer is added to the surface. To contact the n^+-layer, the back-gate, a local etch in citric acid is used to remove the capping layer, the p^{++}-layer as well as parts of the blocking barrier. NiAuGe is deposited on the new surface by electron-beam physical vapour deposition (EBPVD). Low-resistance contacts to the n^+-layer are formed on thermal annealing. To contact the p^{++}-layer, the top-gate, another local etch removes the capping layer. A 100 nm thick Ti/Au contact pad is deposited on the new surface by EBPVD. This contact is not thermally annealed but nevertheless provides a reasonably low-resistance

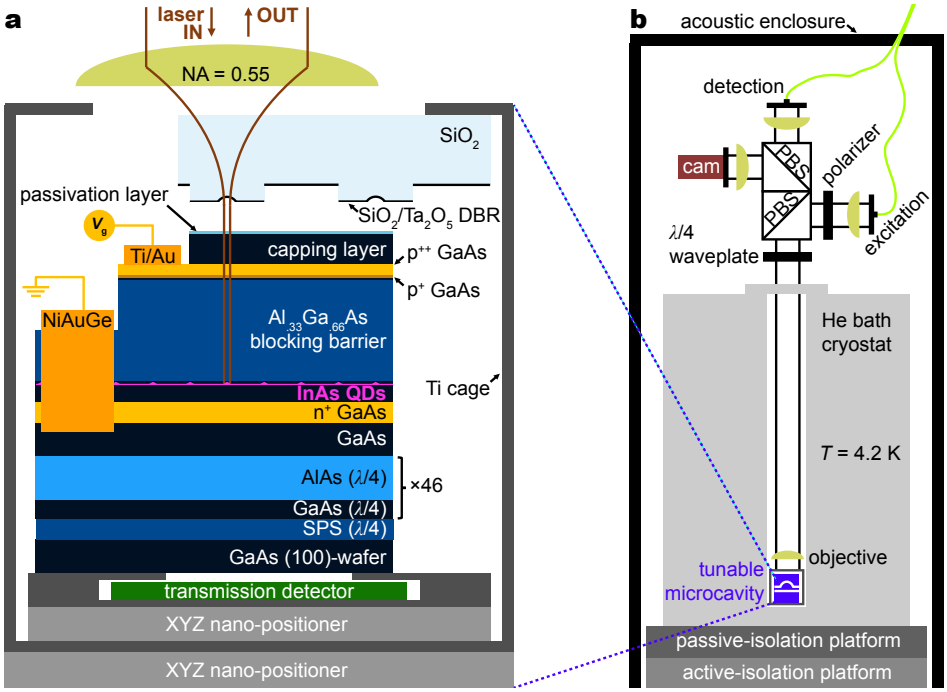

Fig. 3.1. Tunable microcavity setup. **a**, The top-mirror is fixed to the upper inner-surface of a titanium "cage". The sample is mounted on a piezo-driven XYZ nano-positioner; the nano-positioner is fixed to the bottom inner-surface of the cage. The nano-positioner allows for full *in situ* spatial and spectral tuning of the microcavity at cryogenic temperatures. The titanium cage resides on another XYZ nano-positioner allowing for close-to-perfect mode matching of the cavity mode to the external laser beam [53]. **b**, An outer Ti cage containing the inner Ti cage and second nano-positioner is fixed to an optical rod-system which is inserted into a vacuum tube filled with He exchange gas. The optical elements depicted in the image (objective lens, a quarter-wave plate, two polarising beam-splitters (PBSs), a polariser, a CMOS camera, two fibre couplers) make up the dark-field microscope for close-to-background-free detection of resonance fluorescence [64]. The back-reflected laser is suppressed by a factor up to 10^8 by choosing orthogonal polarisation states for the excitation and detection channels [64]. The optical fibre attached to the microscope's excitation (detection) arm includes a 50:50 (99:1) fibre beam-splitter in order to monitor the laser power sent into the microscope (reflected from the sample). The cryostat sits on both active- and passive-isolation platforms and is surrounded by an acoustic enclosure to minimise acoustic noise. Both images are schematic representations and are not to scale. The exact layer thicknesses and doping concentrations are found in the text.

contact to the top-gate (Fig. 3.1a).

Following the fabrication of the contacts to the back- and top-gates, the contacts themselves are covered with photoresist and the surface of the sample is passivated by chemical treatment. HCl removes a thin oxide layer and a few nm of GaAs on the sample surface. After rinsing the sample with deionised water, it is immediately put into an ammonium sulphide ($(NH_4)_2S$) bath and subsequently into an atomic layer deposition

(ALD) chamber. With ALD, 8 nm of Al_2O_3 is deposited at a temperature of 150 °C. This process is essential with the present device to reduce surface-related absorption: a high $\mathcal{Q}$-factor is only achieved with a surface passivation layer. We can only speculate on the microscopic explanation at this point. The passivation procedure reduces the surface density-of-states, leading to an unpinning of the Fermi energy at the surface. On the one hand, this reduces the Franz-Keldysh absorption in the capping layer. On the other hand, it reduces the absorption from mid-gap surface states. A clear advantage of the surface passivation is that native oxides of GaAs are removed and prevented from re-forming: this not only reduces the probability for surface absorption but also provides a robust and stable termination to the GaAs sample [43].

A sample holder contains large Au pads. The Ti/Au and NiAuGe films are connected to the Au pads by wire bonding. Silver paint is used to connect the Au pads to macroscopic wires (twisted pairs).

3.2 Dielectric top mirror

3.2.1 Curvature via CO_2-laser ablation

The template for the curved top-mirror is produced by in-house CO_2-laser ablation [53, 54] on a 0.5 mm thick fused-silica substrate. The radius of curvature of the indentation is 10.5 μm as measured by confocal scanning microscopy [53]; the depth relative to the unprocessed surface is 1.2 μm. After laser ablation, the template is coated with 22 pairs of Ta_2O_5 (refractive index $n = 2.09$) and SiO_2 ($n = 1.46$) layers (terminating with a layer of SiO_2) by ion-beam sputtering [70].

3.3 Microcavity characterisation

3.3.1 Mirror reflectance measurements and modelling

Each mirror is characterised by measuring the reflection at wavelengths outside the stop-band. The reflection oscillates as a function of wavelength. We find that these oscillations are a sensitive function of the exact layer thicknesses of the DBR. The transmission is simulated with a one-dimensional transfer matrix calculation, for instance the Essential Macleod package. A fit is generated, taking the nominal growth parameters as starting point and making the simplest possible assumption to describe systematic differences between the experiment and the calculation. In this way we find that the GaAs (AlAs) layers in the semiconductor DBR start with a physical thickness of 64.6 nm (80.2 nm)

for $n = 3.49$ ($n = 2.92$), reducing linearly to 63.9 (79.8 nm). The change arises simply because the growth rate changes slightly during the long process of growing the DBR. Accordingly, we anticipate that the layers in the active layer have actual thicknesses: n^+-layer 38.9 nm; tunnel barrier 29.4 nm; blocking barrier 183.3 nm; p^{++}-layer 19.0 nm; p^+-layer 4.8 nm; cap 55.8 nm. The main consequence of the slight change in growth rate during growth is that the stopband centre is shifted from 940 nm (design wavelength) to 920 nm. The maximum reflectivity at the stopband centre is not changed significantly by these slight deviations in layer thicknesses.

For technical reasons, the dielectric DBR has a nominal (measured) stopband centre of 1017 nm (973 nm), i.e. red-detuned from the quantum dot emission. Since the transmission could not be measured during deposition at a wavelength of 940 nm, a modified quarterwave stack was chosen which is expected to have similar transmission (87 ppm) at 1064 nm and 940 nm. A laser at 1064 nm was used for *in situ* characterisation. The displacement in stopband centres between top and bottom DBRs is an issue only at wavelengths below 915 nm where the cavity $\mathcal{Q}$-factor decreases rapidly with decreasing wavelength. Matching of the two stopband centres would give a high $\mathcal{Q}$-factor over a larger spectral range.

Further details on reflectance measurements are presented in Chapter 4.

3.3.2 Microcavity $\mathcal{Q}$-factors

A microcavity was constructed using a planar dielectric mirror and the same curved dielectric mirror used for the main quantum dot experiment. Both planar and curved silica templates were coated in the same run. With the smallest possible mirror separation of $3\lambda/2$ (limited by the indentation depth of the curved mirror) we determine $\mathcal{Q}$-factors of $1.7 \cdot 10^5$ ($1.5 \cdot 10^6$) at 920 nm (980 nm) at room temperature. The fundamental microcavity mode splits into a doublet with orthogonal polarisations. At a wavelength of 920 nm, this splitting is typically 13 GHz. These measurements demonstrate the very high quality of the dielectric mirror, in particular the curved dielectric mirror.

The microcavity consisting of the semiconductor mirror and the same curved dielectric mirror has a $\mathcal{Q}$-factor of typically $5 \cdot 10^5$ at 920 nm at 4.2 K (Fig. 2, main text), a factor of ~ 3 larger than the dielectric DBR-dielectric DBR microcavity described above. This increase can be explained by a factor of two larger effective cavity length of the semiconductor-dielectric cavity – the group delay of the semiconductor mirror is larger than that of a dielectric mirror due to the $3\lambda/2$-thick active layer – and a factor of 1.5 larger finesse. This increase in finesse suggests that at 920 nm the reflectance of the semiconductor mirror is higher than that of the dielectric mirror.

The fundamental mode at wavelength 920 nm has a polarisation splitting of typically 32 GHz. This is larger than the polarisation splitting of the dielectric DBR-dielectric DBR microcavity (13 GHz at 920 nm). This suggests that the main origin of the polarisation splitting is birefringence in the semiconductor induced by strain (AlAs is not exactly lattice-matched to GaAs).

Further details on measured $\mathcal{Q}$-factors with passivated and unpassivated semiconductor DBRs are presented in Chapter 4.

3.3.3 Low-temperature setup and stability

Both the top-mirror and the GaAs sample are firmly glued to individual titanium sample holders and mounted inside a titanium "cage" (Fig. 3.1a). The holder for the GaAs sample is fixed to a stack of piezo-driven XYZ nano-positioners while the top-mirror holder is fixed to the titanium cage via soft (indium) washers which act as a flexible material for tilt alignment at room temperature. Observing the cavity with a conventional optical microscope and tightening each screw of the mirror holder individually, Newton rings appearing between the two mirrors can be centred in order to guarantee mirror parallelism at room temperature. The entire microcavity setup is then inserted in another titanium cage. This outer cage is connected to an optical cage system inside a vacuum tube. The tube is evacuated, flushed with He exchange gas (25 mbar), pre-cooled in liquid nitrogen and finally transferred into the helium bath cryostat.

In order to minimise the exposure of the microcavity to acoustic noise, the cryostat is decoupled from floor vibrations via both active and passive isolation platforms (Fig. 3.1b). An acoustic enclosure surrounds both the entire cryostat and microscope, providing a shield against airborne acoustic noise (Fig. 3.1b). There is no active feedback mechanism acting on the microcavity's z-piezo. Nevertheless, a root-mean-square cavity length fluctuation [53] of ~ 0.5 pm was measured in the best case, limiting our $\mathcal{Q}$-factors to $\mathcal{Q} \approx 2.0 \cdot 10^6$. This corresponds to our highest measured $\mathcal{Q}$-factor of $\mathcal{Q} = 1.5 \cdot 10^6$ in the case of a microcavity consisting of the curved top mirror paired with a dielectric bottom mirror of identical coating. This suggests that in the case of a GaAs sample–curved dielectric mirror combination the $\mathcal{Q}$-factor is only slightly reduced by environmental noise.

3.4 Quantum dot characterisation without top mirror

3.4.1 Single-electron or -hole charging via gate control

To characterise quantum dot charging, photoluminescence (PL) measurements were performed using non-resonant excitation at a wavelength of 830 nm as a function of the voltage applied between top- and bottom-gates. Fig. 3.2a shows such a PL charge map taken on the sample without the top mirror. Both positive (X^+) and negative (X^-) trions as well as the neutral exciton (X^0) were identified. The charge states of a quantum dot within the cavity can be recorded in a similar way. In order to detect all the PL before filtering by the cavity, a sine wave voltage is applied to the cavity's z-piezo so that the cavity is continuously scanned through one free spectral range per integration time window of the spectrometer.

3.4.2 Resonance fluorescence via cross-polarised detection

Each quantum dot's behaviour under resonant excitation can be investigated by suppressing back-reflected laser light in the detection arm, detecting the resonance fluorescence (RF). We achieve this with a dark-field technique [64]. The optical components are shown in Fig. 3.1b. The excitation laser passes through a linear polariser with polarisation matched to the reflection of the lower polarising beam splitting (PBS). The two PBSs transmit the orthogonal polarisation in the vertical direction, the detection channel. The final polarising element of the excitation channel and the first polarising element of the detection channel is a a quarter-wave plate. It has a dual function. First, by setting the angle of the quarter-wave plate to 45°, the microscope can also be operated in bright-field mode. This is very useful for alignment purposes and for optimisation of the out-coupling efficiency. Secondly, in dark-field mode, the quarter-wave plate allows very small retardations to be introduced, correcting for the slight ellipticity in the excitation polarisation state [64]. The quarter-wave plate allows extremely high bright-field-to-dark-field extinction ratios to be achieved. The microscope can be operated in a set-and-forget mode – once the polariser and wave-plate are aligned, the laser suppression is maintained over days in the original setup [64] and even weeks in this case. This very robust operation (despite the fact that control of the wave-plate rotation at the milli-degree level is necessary [64]) is likely to be a consequence of the effective damping of acoustic and vibrational noise acting on the microscope head in the cavity experiment.

An RF scan of QD5 without top mirror is shown in Fig. 3.2b. The detuning between quantum dot and laser is controlled in this case by fixing the laser frequency and scanning

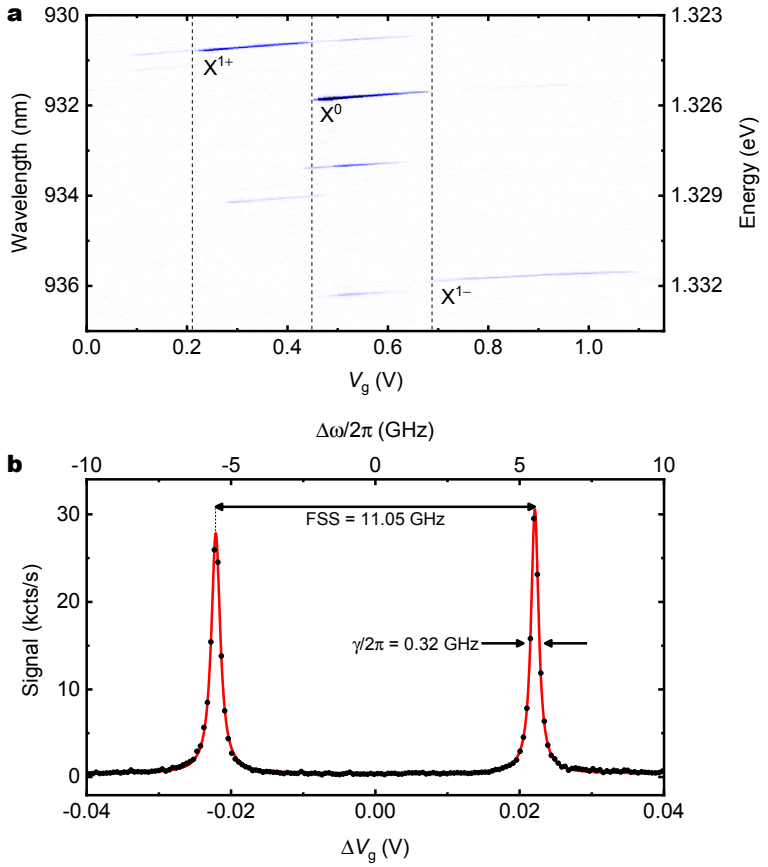

Fig. 3.2. Quantum dot charging and neutral exciton linewidth. a, Measured photoluminescence signal of non-resonantly excited QD4 ($\lambda = 830\,\text{nm}$, $P = 200$ nW, $B = 0.00$ T) as a function of gate voltage. The three main charge states of the quantum dot are the positive trion (X^+), neutral exciton (X^0) and negative trion (X^-). Dark blue: maximum counts, white: minimum counts. **b**, Resonance fluorescence on QD5 (X^0, $\lambda = 939\,\text{nm}$, $B = 0.00$ T) excited well below saturation (red solid line: Lorentzian fit). With a measured Stark shift of 240 GHz/V, a linewidth of 0.32 GHz is obtained, a value close to the typical transform limit of 0.20 GHz for these InGAs quantum dots. The splitting arises from the X^0 fine structure which for QD5 is 11.05 GHz.

the gate voltage which detunes the quantum dot resonance frequency via the dc Stark shift. Two peaks are observed from the neutral exciton, X^0. The splitting corresponds to the fine-structure splitting (FSS). Taking several scans for different laser frequencies, a dc Stark shift of 240 GHz/V is determined on this particular quantum dot. The measured full-width-at-half-maximum of each neutral exciton peak corresponds to 0.32 GHz, a value close to the transform limit of 0.20 GHz for these InAs quantum dots [71].

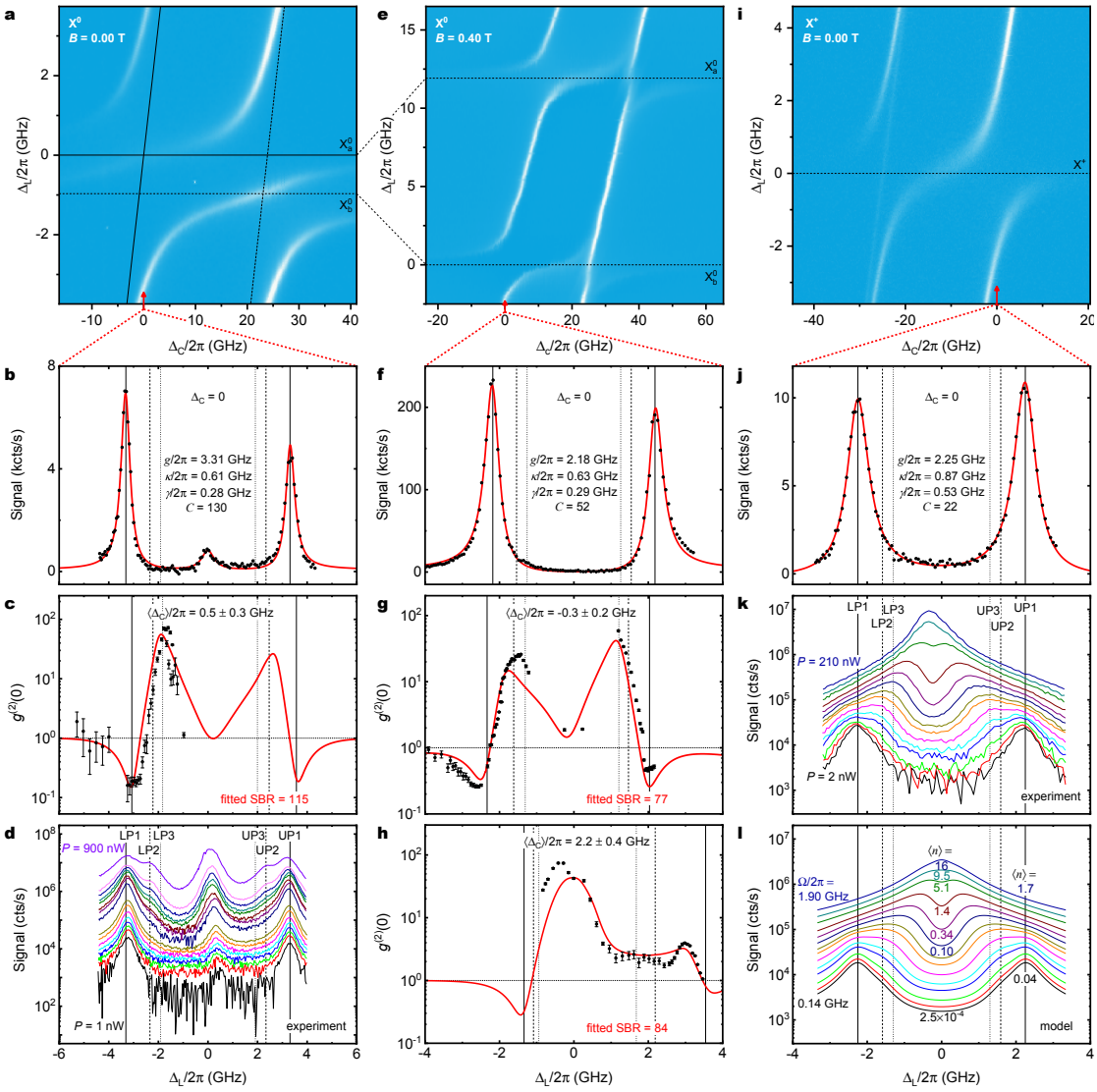

Fig. 3.3. Spectroscopy on cavity-coupled QD1. **a**, X^0 at $B = 0.00$ T: RF scan revealing two TEM_{00} cavity modes with polarisation splitting of 25 GHz (inclined lines) coupled to two fine-structure-split levels of X^0 with FSS of 1 GHz (horizontal lines). **b**, Line cut at resonance to "left" cavity mode (as indicated by red arrow). The main peaks arise from coupling of the "high" frequency X^0 transition to one cavity mode; the peak at $\Delta_L = 0$ arises from coupling of the "low" frequency X^0 transition to the same cavity mode. **c**, $g^{(2)}(0)$ versus laser detuning for a cavity detuning close to zero. **d**, Power dependence at resonance. Excitation of the second rung of the Jaynes-Cummings ladder (LP2, UP2) is evident at high powers as indicated by the dashed vertical lines. **e**, X^0 at $B = 0.40$ T: RF scan reveals that the same TEM_{00} cavity modes couple to the two X^0 transitions. The X^0 transitions are now separated by the Zeeman splitting. **f**, Line cut at resonance to "left" cavity mode. (Continued on the following page.)

Fig. 3.3. (continued). **g,h**, $g^{(2)}(0)$ versus laser detuning for two different cavity detunings, one close to zero, the other one close to g. **i**, X^+ at $B = 0.00$ T: RF scan of the X^+ transition. **j**, Line cut at resonance to "right" cavity mode. **k,l**, Experimental and theoretical power dependence at resonance, respectively. Excitation of higher rungs of the Jaynes-Cummings ladder is evident by the convergence from the two first-rung polaritons towards the bare cavity mode with increasing power leading to a calculated mean photon number in the cavity of maximum $\langle n \rangle = 16$. The Hilbert space in the model is truncated to 35 rungs of the Jaynes-Cummings ladder. The slight frequency shift of the signal peak in **k** at maximum laser power is due to an unintended drift of the cavity length during this experiment. In all figures, the vertical lines depict the resonance frequencies for the first three rungs of the Jaynes-Cummings ladder (LP1/UP1: continuous, LP2/UP2: dashed, LP3/UP3: dotted) at a particular cavity detuning.

3.5 Resonance fluorescence from a cavity-coupled quantum dot

3.5.1 Polarisation axes

The X^0 polarisation axis (or, in shortened form, "axis") varies from quantum dot to quantum dot. The cavity also has an axis. A complication is that the cavity mode splitting (32 GHz), the X^0 fine-structure (1–10 GHz), and the frequency separating the two polaritons in the strong-coupling regime (6–9 GHz) are all similar. Fig. 3.3a shows an example: full RF scans of cavity-coupled QD1 are shown, together with their respective line-cuts at zero cavity detuning (Fig. 3.3b, f, j). The fundamental cavity mode splits into two modes with linear and orthogonal polarisations. At zero magnetic field ($B = 0.00$ T) the neutral exciton X^0 also splits into two lines with linear and orthogonal polarisations. In the case of QD1 at $B = 0.00$ T, the X^0 and cavity axes are close-to-parallel such that one X^0 line couples strongly to one cavity mode, weakly to the other cavity mode, and vice versa for the other X^0 line (Fig. 3.3a). The line-cut at one particular cavity frequency shows the polaritons and a weak feature in between (Fig. 3.3b). The analysis including both cavity modes and two X^0 transitions makes it clear that in Fig. 3.3b, the two polaritons arise from strong coupling between one X^0 transition and one cavity mode. The central feature arises from an out-of-resonance response of the strong coupling between the other X^0 transition and the other cavity mode. The bare cavity mode is not observed at all in the spectral range of Fig. 3.3a.

The quantum dot-cavity couplings can be selected in a few ways in this experiment.

First, the X^0 axis varies from quantum dot to quantum dot. It is not difficult to find a quantum dot whose axis matches closely that of the cavity such that one X^0 line interacts primarily with one cavity mode, the other X^0 line interacts primarily with the other cavity mode. Fig. 3.3a depicts an example of this behaviour.

Secondly, application of a small magnetic field pushes the two X^0 lines apart in fre-

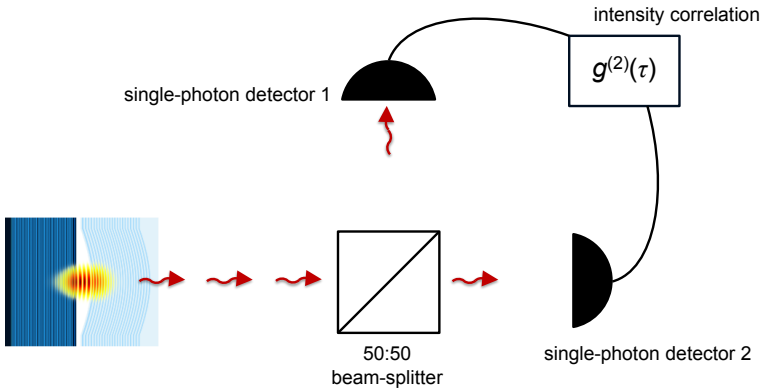

Fig. 3.4. Schematic of the Hanbury Brown-Twiss (HBT) setup. The microcavity signal is split via a 50:50 fibre beam-splitter and detected via two superconducting nanowire single-photon detectors (SNSPDs, Single Quantum Eos) connected to a time-tagging hardware (PicoHarp 300). By recording the absolute arrival time and detector channel of each detected photon, a correlation algorithm is used to calculate the second-order correlation function, $g^{(2)}(\tau)$, with a binning time of 4 or 16 ps.

quency. At a magnetic field of $B = 0.40$ T, the X^0 lines (QD1) are separated by 12 GHz such that if one X^0 line is resonant with the microcavity, the other X^0 line is far detuned. Fig. 3.3b,f show an example. At these magnetic fields, the X^0 lines become circularly polarised such that the X^0 axis plays no further role. The price to pay is a reduction by a factor of $\sqrt{2}$ in the coupling parameter g with respect to the optimal value at zero magnetic field (Fig. 3.3f).

Thirdly, the fine-structure splitting disappears on switching to a charged exciton, either X^- or X^+: there is just one peak at zero magnetic field (Fig. 3.3i,j), a Zeeman-split doublet at finite magnetic field.

To exploit all three options, we stress the power of the *in situ* cavity detuning. On applying a magnetic field or changing the voltage applied to the device, the quantum dot optical frequency changes by many cavity linewidths but in each case the cavity can be brought into resonance.

3.6 Second-order correlation measurements

3.6.1 Hanbury Brown-Twiss (HBT) setup

Second-order correlation measurements are performed with a Hanbury Brown-Twiss (HBT) setup. The resonance fluorescence signal from the detection fibre (Fig. 3.1b) is sent to a 50:50 fibre beam-splitter and then to two superconducting nanowire single-photon detectors (SNSPDs, Single Quantum Eos). In these experiments, all the photons

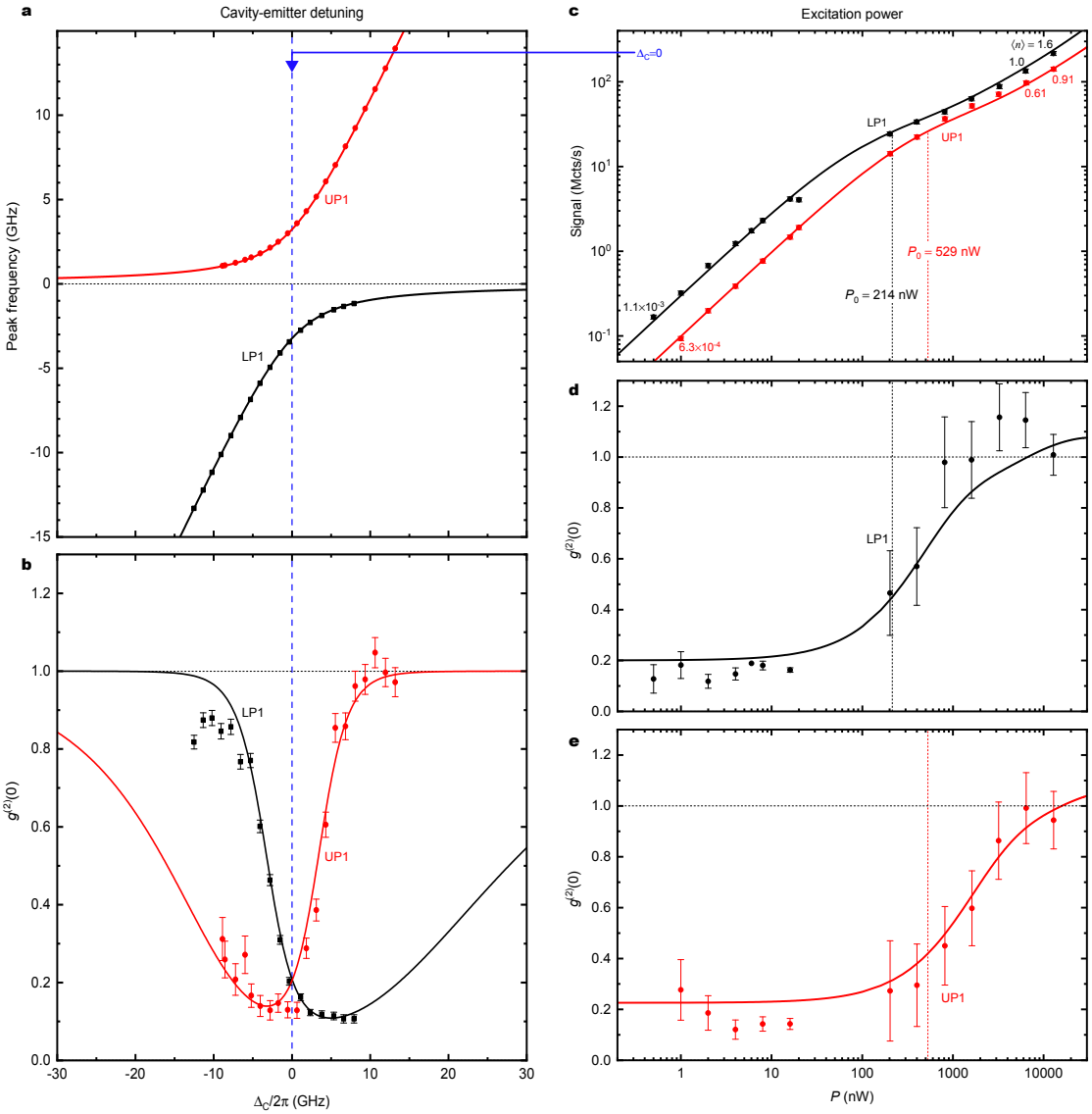

Fig. 3.5. Spectroscopy on cavity-coupled QD2. **a**, Experimental and theoretical dispersion of the lower (LP1) and the upper polariton (UP1). **b**, Corresponding experimental and theoretical $g^{(2)}(0)$ values. **c**, Intensity of scattered light from LP1 and UP1 at zero cavity detuning as a function of resonant excitation power. The absence of saturation is due to population of higher rungs of the Jaynes-Cummings ladder with increasing power. The behaviour at low powers allows the dependence of the Rabi frequency Ω on laser power P to be determined. This behaviour is parameterised with power P_0 (see text for definition of P_0): $P_0 = 214$ nW for LP1 and $P_0 = 529$ nW for UP1 (black and red dashed vertical lines, respectively). The mean photon number $\langle n \rangle$ is shown. **d,e**, corresponding experimental and theoretical $g^{(2)}(0)$ values for LP1 and UP1. All data from X^0 in QD2 at $B = 0.50$ T.

from the experiment were sent to the HBT setup: spectral selection was not employed. Each SNSPD has a detector efficiency of $\eta_{\text{detector}} \approx 85\%$ and a negligible dark count rate (10–40 cts/s). The total timing resolution in the $g^{(2)}$-mode includes the timing resolution of both SNSPDs and the resolution of the time-tagging hardware. In total, it is ≈ 35 ps (FWHM) which is well below the measured vacuum Rabi-periods in this work.

The dead time of the time-tagging hardware is $\simeq 95$ ns which sets a limit for the maximally detectable count rate. In order to measure higher count rates than ~ 5 Mcts/s per detector, the 1%-arm of the detection fibre is used instead of the 99%-arm and the counts are calibrated accordingly.

For the evaluation of $g^{(2)}(\tau)$ we use a time window of 100 ns. For all presented $g^{(2)}(\tau)$ data, we use a bin size of 4 ps. For all presented $g^{(2)}(0)$ values, we perform a fast Fourier transform (FFT) of $g^{(2)}(\tau)$ (bin size: 16 ps), we then cut all frequency components above 14 GHz and calculate the inverse FFT. In this way, we make sure that the $g^{(2)}(0)$ values are averaged over a time of 35 ps, a time large with respect to the original binning 16 ps, but small with respect to the period of the vacuum Rabi-oscillations.

3.6.2 Vacuum Rabi-frequency versus cavity detuning

Fig. 2.3 shows $g^{(2)}(\tau)$ as a function of delay τ for a cavity which is detuned by $\Delta_{\text{C}} = 0.73g$ with respect to the emitter. Here we show that vacuum Rabi-oscillations in $g^{(2)}(\tau)$ are observed for different values of Δ_{C} and that the frequency of these oscillations changes according to the change in polariton splitting in the $|1\pm\rangle$ manifold for different values of Δ_{C} (see Fig. 3.6 and section V for analytical calculations for the case of $\Delta_{\text{C}} = 0$). The dashed vertical line in Fig. 3.6 depicts the cavity detuning for the data shown in Fig. 2.3. Consistent with the excellent agreement of the numerical model for $g^{(2)}(\tau)$ with the experiment, an analytical approach to determine the vacuum Rabi-period yields $T = 220$ ps in exact agreement with the experimental observations.

3.6.3 $g^{(2)}(0)$ versus laser- and cavity detuning

In the experiment, three frequencies can be tuned *in situ*: the laser frequency ω_L, the emitter frequency ω_C (via the gate voltage) as well as the cavity frequency ω_0 (via tuning of the cavity length).

Fig. 2.4e shows $g^{(2)}(0)$ as a function of laser detuning Δ_{L} for a cavity detuning $\Delta_{\text{C}} = 0$ on QD2 at $B = 0.50$ T. $g^{(2)}(0)$ can be described well with the model and a small laser background. This point is investigated also in other cases. In Fig. 3.3c,g and h, more

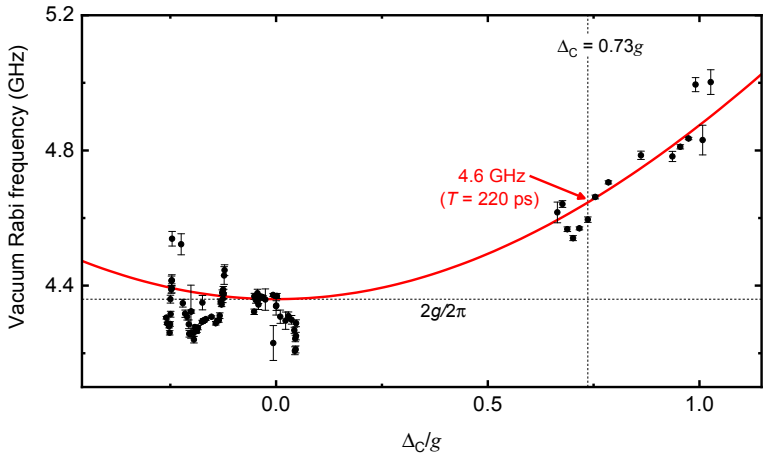

Fig. 3.6. Vacuum Rabi-frequency versus Δ_C. The data points correspond to measured vacuum Rabi-frequencies (determined via FFT of $g^{(2)}(\tau)$) for different cavity detunings Δ_C. The red solid-line is an analytical calculation of the polariton splitting in the $|1\pm\rangle$ manifold for different values of Δ_C (see Supplementary section IV in Ref. [67]) using a coupling strength measured via spectroscopy (Fig. 3.3f). Data from X^0 in QD1 at $B = 0.40$ T.

$g^{(2)}(0)$ measurements of the neutral excition of QD1 at $B = 0.00$ T and 0.40 T are shown: c and g are recorded with close-to-zero cavity detuning, h with a cavity detuning of $\Delta_C \approx g$.

The *in situ* tunability of the microcavity can be exploited by an alternative experiment in which the cavity is detuned and the polaritons are driven resonantly at each cavity detuning. Fig. 3.5a,b show exactly this, specifically the behaviour of the first-rung polaritons (LP1 in black, UP1 in red) as a function of Δ_C. Also in this case, the model reproduces the experimental results well. The reason for the slight discrepancy in $g^{(2)}(0)$ of the lower polariton at large and negative Δ_C is the fact that the laser starts driving the second fine-structure level which is weakly coupled to the same cavity mode. This increases slightly the number of single photons in the detection signal as evidenced by the slight anti-bunching in the experimental data.

3.6.4 Power dependence of $g^{(2)}(0)$ and signal

The experiments in Fig. 2.1–2.4(b–g), Fig. 3.3a–c,e–j and Fig. 3.5a,b are all recorded with a weak driving laser, i.e. with a mean photon number in the cavity well below one. We present here the behaviour as the power of the driving laser increases.

In Fig. 3.5c we plot the measured and calculated scattering signal on driving LP1 (black) and UP1 (red) with increasing excitation power. A striking feature is that the

system does not saturate (Fig. 3.5c). This is evidence that the full ladder of Jaynes-Cummings levels exists. To model the power dependence, it is necessary to determine the connection between the Rabi frequency Ω, the input parameter to the model, and the laser power P, the control parameter in the experiment. Clearly, $\Omega \propto \sqrt{P}$. At the lowest powers, only the zeroth and first rungs of the Jaynes-Cummings ladder are populated such that the $|0\rangle \leftrightarrow |1-\rangle$ and $|0\rangle \leftrightarrow |1+\rangle$ transitions behave like two-level systems: the scattered signal increases linearly with laser power, as expected (Fig. 3.5c).

We parameterise the link between Ω and P by adopting the link for a two-level system, namely $\Omega = \sqrt{\frac{P}{P_0}}\frac{\kappa+\gamma}{2}\frac{1}{\sqrt{2}}$, where P is the laser power (monitored at the 50:50 fibre beam-splitter) and P_0 is a reference power. The signal S is equal to the steady-state photon occupation in the cavity multiplied by the cavity loss-rate (κ) and the cavity-to-detector system efficiency (η_{system}), $S = \eta_{\text{system}} \cdot \kappa \cdot \langle n \rangle$. We calculate $\langle n \rangle$ from the Jaynes-Cummings model with (g, κ, γ)-parameters determined from the spectroscopy experiment and $(\Delta_{\text{C}}, \Delta_{\text{L}}) = (0, \pm g)$.

The nonlinear power-dependence (Fig. 3.5c) enables both P_0 and η_{system} to be determined. A fit to the experimental data leads to $P_0 = 214$ nW ($P_0 = 529$ nW) for LP1 (UP1) and $\eta_{\text{system}} = 12\%$. The difference in powers P_0 for LP1 and UP1 results in an unequal population of the polaritons at constant input powers, as seen in Fig. 2.2f,g. The difference in P_0-values probably arises from a polarisation-dependent chromaticity in the throughput of the microscope's excitation channel. The same model gives excellent agreement with the experimental $g^{(2)}(0)$ both for the LP1 and UP1 (Fig. 3.5d,e).

The behaviour as a function of driving power can also be explored by measuring the Δ_{L}-dependence of the scattered intensity for $\Delta_{\text{C}} = 0$. Fig. 3.3d,k show power-dependent RF scans when the bare exciton and cavity are resonant. At low power, LP1 and UP1 are clearly resolved. At higher power, bumps appear at the two-photon LP2 and UP2 resonances. In Fig. 3.3k, there is no resonance close to the bare cavity mode at low power, enabling us to explore the full behaviour even at very large driving powers. At the highest powers, the response is dominated by a feature at $\Delta_{\text{L}} \approx 0$ (Fig. 3.3k). This too is evidence that the full Jaynes-Cummings ladder can be accessed. At the highest powers, the system "climbs" the Jaynes-Cummings ladder on account of the bosonic enhancement of photons such that the average photon occupation is large and the polariton resonances become closer in frequency to the bare cavity mode. This power dependence can also be described with the model and very good agreement between our numerical model and the data in Fig. 3.3k is found. (Due to the presence of the second fine-structure level in Fig. 3.3d, our numerical model is incomplete in this case.)

3.7 Cavity-to-detector efficiency and overall quantum efficiency

The power dependence, Section 3.6.4, enables us to determine $\eta_{\text{system}} = 12\%$. η_{system} is the quantum efficiency of the entire detection system, the probability that a photon in the cavity is detected by the detector (cavity-to-detector efficiency).

One contribution to η_{system} is the outcoupling efficiency [32], which is defined as the fraction of photons in the κ-channel leaving through the top mirror (rate κ_{top}):

$$\eta_{\text{out}} = \frac{\kappa_{\text{top}}}{\kappa} = \frac{T_{\text{top}}}{T_{\text{top}} + T_{\text{bottom}} + A}. \tag{3.1}$$

Using the modelling of the mirrors (Section 4.2), we determine $(T_{\text{top}}, T_{\text{bottom}}, A) = (116, 1, 373)\,\text{ppm}$ at wavelength $\lambda = 923\,\text{nm}$. Here, T_{top} (T_{bottom}) and A are the fractional intensity losses per round trip via transmission through the top (bottom) mirror and absorption/scattering losses, respectively. This gives $\eta_{\text{out}} = 24\%$.

The system efficiency can be described with a number of additional factors. If the cavity and microscope axes lie at $\phi = 45^\circ$ to each other, $\eta_{\text{dark-field}} = 50\%$. This is not exactly the case in practice. For X^0 in QD2 ($B = 0.50$ T), $\phi = 37^\circ \pm 6^\circ$ resulting in $\eta_{\text{dark-field}} = (63 \pm 10)\%$. Once a photon has entered the detection channel after the dark-field polarisation-optics, it is coupled into the collection fibre with probability η_{fibre}. Overall,

$$\eta_{\text{system}} = \eta_{\text{out}} \cdot \eta_{\text{dark-field}} \cdot \eta_{\text{fibre}} \cdot \eta_{\text{detector}}. \tag{3.2}$$

The detector has a quantum efficiency of $\eta_{\text{detector}} = 85\%$ (Section 3.6.1). From these results, we find that $\eta_{\text{fibre}} = (94 \pm {}^{6}_{15})\%$.

The collection fibre is a single-mode optical fibre and supports a propagating Gaussian-mode. The high value of η_{fibre} is only possible with excellent mode-matching between the cavity-output and the optical fibre: it constitutes experimental proof that the cavity output is described extremely well by a Gaussian-mode.

Note that the exciton-to-photon quantum efficiency (the probability of an exciton producing a photon which exits via the κ-channel) of the microcavity [31] is

$$\eta_{\text{cavity}} = \beta \cdot \frac{\kappa}{\kappa + \gamma}, \tag{3.3}$$

which is 72% for QD2 ($B = 0.50$ T). The overall exciton-to-detector quantum efficiency reads

$$\eta_{\text{exciton}} = \eta_{\text{cavity}} \cdot \eta_{\text{system}}, \tag{3.4}$$

which is 8.6% in this case.

Chapter 4

Surface passivation as key to $\mathcal{Q}$-factors up to one million

4.1 Summary

We present a surface passivation method that reduces surface-related losses in a highly miniaturised Fabry-Pérot cavity by almost two orders of magnitude. The fully tunable microcavity consists of a curved (radius $\sim 10\,\mu$m) dielectric distributed Bragg reflector (DBR) paired with an n-i-p diode containing self-assembled quantum dots on top of a semiconductor DBR. Positioning the highly p- and n-doped layers close to a node of the vacuum electric field is essential to minimize free-carrier absorption in the gates. By passivating the semiconductor DBR, we find experimentally that the remaining absorption losses originate from the semiconductor surface itself or the GaAs "capping" layer below the surface. We interpret surface passivation to reduce the surface density of states and thus the surface-related absorption. Leading to an unpinning of the surface Fermi-level, the electric field in the capping layer and thus below-band-gap absorption via the Franz-Keldysh effect are reduced. Our findings are not only of importance for the realization of efficient single-photon sources in the solid state [32, 41] but paved the way for achieving high splitting-to-linewidth ratios in a strongly coupled cavity-QED system (Chapter 3).

4.2 Introduction

Minimizing the absorption and scattering losses in a microcavity is an ultimate goal of cavity quantum electrodynamics (cavity-QED). First, for single-photon sources in the weak-coupling regime, an efficient photon extraction is needed [32, 41]. Secondly, a coherent exchange between an ("artificial") atom and a cavity-confined vacuum electric

field in the strong-coupling regime is only useful if the coherent coupling rate g dominates over all loss mechanisms via the cavity (photon loss rate κ) or the atom's spontaneous decay rate (γ) by a large margin. This requires a small mode volume together with either moderate $\mathcal{Q}$-factors limited by transmission losses only (weak coupling) or ultrahigh $\mathcal{Q}$-factors combined with ultralow emitter linewidths (strong coupling). Reaching the strong-coupling regime of cavity-QED at optical frequencies with a high splitting-to-linewidth ratio has been a major challenge in atomic [5–8] and solid-state physics [9, 10, 16, 49]. It has been shown with GaAs microdisk resonators [43] that surface passivation is crucial for achieving $\mathcal{Q}$-factors in the order of a few million. The combination of an ultrahigh-$\mathcal{Q}$-factor microcavity with an emitter featuring ultralow linewidths close to the radiative limit has however been missing so far. Radiatively limited emission from a semiconductor quantum dot can be obtained by embedding the quantum dots within an n-i-p diode [40].

In this work, we embed an n-i-p diode containing InAs quantum dots in a fully tunable microcavity which exhibits a $\mathcal{Q}$-factor close to 10^6 despite the absorbing gates suffering from free-carrier absorption [62]. Obtaining an ultrahigh $\mathcal{Q}$-factor close to the one expected from the DBR layer design is based on two crucial steps. First, the n-i-p heterostructure is designed in a way that the highly absorbing gates lie in (or close to*) a node of the vacuum electric field to reduce free-carrier absorption (which is around $\alpha \sim 69$ cm^{-1} for p^{++}-GaAs and $\alpha \sim 69$ cm^{-1} for n^{+}-GaAs, 0.17 eV below the bandgap of GaAs [62]). Secondly, the semiconductor surface has to be passivated in order to reduce surface-related absorption losses [43]. We present below-bandgap absorption via the Franz-Keldysh (F-K) effect [72–76] in the capping layer as one possible explanation for the highly reduced $\mathcal{Q}$-factors in the unpassivated case.

The microcavity [52, 53] consists of a curved dielectric DBR (produced by CO_2-laser ablation [54]) paired with an n-i-p heterostructure embedding InAs quantum dots (QDs) on top of a semiconductor DBR ("nip-DBR", Fig. 4.1a). Terminating with SiO_2, the dielectric DBR is composed of 22 layer pairs of $SiO_2(\lambda/4)$ and $Ta_2O_5(\lambda/4)$, where λ depicts the wavelength in each material. The stopband (SB) centre† is 973 nm. The semiconductor DBR consists of 46 layer pairs of AlAs($\lambda/4$) and GaAs($\lambda/4$). The heterostructure is a 1.5λ-layer of GaAs including doped layers acting as top-gate (p^{++}, 10^9 cm^{-3}) and back-gate (n^{+}, $2 \cdot 10^8$ cm^{-3}). The quantum dot layer is placed at an antinode

*Due to a restriction to the tunnel barrier thickness between back-gate and quantum dot layer, the backgate is positioned slightly off-center with respect to the vacuum electric field node.

†Note that in this work, we define the SB centre in the 1D transfer matrix model (Appendix B) as the mean value of the two wavelengths that correspond to the local minima (with $R < 90\%$) of the calculated reflectance spectrum that are closest to the maximum mirror reflectance (Fig. 4.1b).

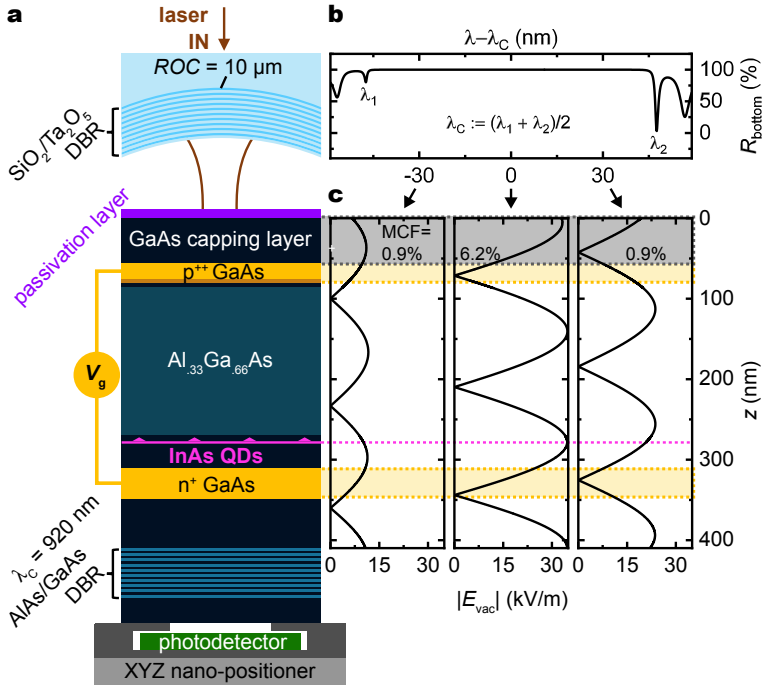

Fig. 4.1. Ultrahigh-$\mathcal{Q}$ optical microcavity as sensitive probe for surface-related absorption. **a**, Schematic of the microcavity involving a curved dielectrid DBR and an n-i-p heterostructure with self-assembled InAs quantum dots on top of a semiconductor DBR ("nip-DBR"). **b**, Simulated reflectance of the nip-DBR with stopband (SB) centre $\lambda_C = 920\,\text{nm}$. **c**, Calculated vacuum-field amplitude across the heterostructure for three different wavelengths $(-30, 0, +30)\,\text{nm}$ from the SB centre. As the antinodes of the vacuum-field amplitude shift with wavelength changing the modal confinement factor (MCF) in the GaAs capping layer, surface-related absorption in the capping layer (10^{-10}–$10^{-8}\,\text{cm}^{-1}$) can be probed via the microcavity by measuring its $\mathcal{Q}$-factor across the SB. At λ_C, where the coupling to the QDs is maximised, free-carrier absorption in the highly doped p- and n-gates is minimised by placing them close to a vacuum-field node. Note that the highly reduced vacuum-field at $\lambda - \lambda_C = -30\,\text{nm}$ arises from a shift of the vacuum energy into the vacuum-gap.

of the vacuum electric field (at a distance λ below the surface). The intrinsic region between quantum dots and back-gate acts as tunnel barrier for electrons based on Coulomb blockade [22]. Using a piezo-based XYZ nano-positioner, the microcavity features full *in situ* tunability at room and cryogenic temperatures. Measuring the $\mathcal{Q}$-factor across the nip-DBR's SB (Fig. 4.1b) reveals possible sources of loss in the heterostructure due to the fact that the standing wave inside the cavity shifts with wavelength (Fig. 4.1c). Losses in the capping layer for instance depend on the exact wavelength: close to $(-30, 0, 30)\,\text{nm}$ from the nip-DBR's SB centre the calculated modal confinement factor (MCF *) of the

*The MCF is defined as the electromagnetic energy confined in the layer-of-interest divided by the energy of $\hbar\omega/2$ confined by the entire vacuum-field mode [43].

capping layer is $(0.9\%, 6.2\%, 0.9\%)$, respectively.

4.3 GaAs surface passivation

The surface passivation recipe to unpin the Fermi level at the semiconductor surface is partly oriented towards one of the procedures in Ref. [77], for instance. As a first cleaning step, the post-processed semiconductor sample (already containing Au contact pads) is successively immersed in acetone, isopropanol and ethanol inside an ultrasonic bath at $T = 40°\mathrm{C}$. To prevent surface passivation on the contact pads, they are covered by a manually applied drop of photoresist (AZ1512HS, Microchemicals GmbH) and baked for 10 min at $T = 100°\mathrm{C}$. At room temperature, the sample is dipped into an HCl solution (25%) for 1 min in order to remove the native oxide [77]. The sample is then rinsed with deionized water for $\sim$ 1s and immediately soaked in an $(NH_4)_2S$ solution (20%) for 10 min. Without rinsing the sample, it is blown dry by nitrogen and immediately transferred into an ALD chamber (Savannah 100, Cambridge NanoTech Inc.).

The following ALD recipe is chosen to deposit $\sim 8\,\mathrm{nm}$ of Al_2O_3 onto the sample surface: $T = 150°\mathrm{C}$, first pulse 50 ms (water), wait 12 s, second pulse 40 ms (TMA), wait for 10 s, cycle 80 times. The Al_2O_3 layer acts as diffusion barrier for oxygen [78], thus preventing reoxidation of the etched GaAs surface.

After surface passivation, the remaining challenge is to remove the photoresist that has been crosslinked at $T = 150°\mathrm{C}$ inside the ALD chamber. The use of *N*-Methyl-2-pyrrolidone (NMP) at elevated temperatures has shown to successfully remove the crosslinked photoresist. The sample is immersed in NMP for 9–20h (while 20h yielded a better result) at $T = 40°\mathrm{C}$ and then successively cleaned for 5 min in NMP, acetone, isopropanol and methanol inside an ultrasonic bath at $T \sim 56°\mathrm{C}$. As a final step, a polymeric strip coating (First Contact, Photonic Cleaning Technologies) is used to remove final residues from the sample surface.

4.4 Individual mirror characterisation: stopband oscillations

As depicted in Fig. 4.2, the cavity's top and bottom mirror are characterised at $T = 4.2\,\mathrm{K}$ by a broadband light source (white LED or halogen lamp) and a dark-field confocal microscope [40]. The light from the source is coupled into a single-mode optical fibre leading to a collimator, an objective lens (NA=0.55) and finally the sample surface. Cross-polarising elements are used in the beam path to distinguish the normally reflected light from the normally incident light. The detection fibre is connected to a

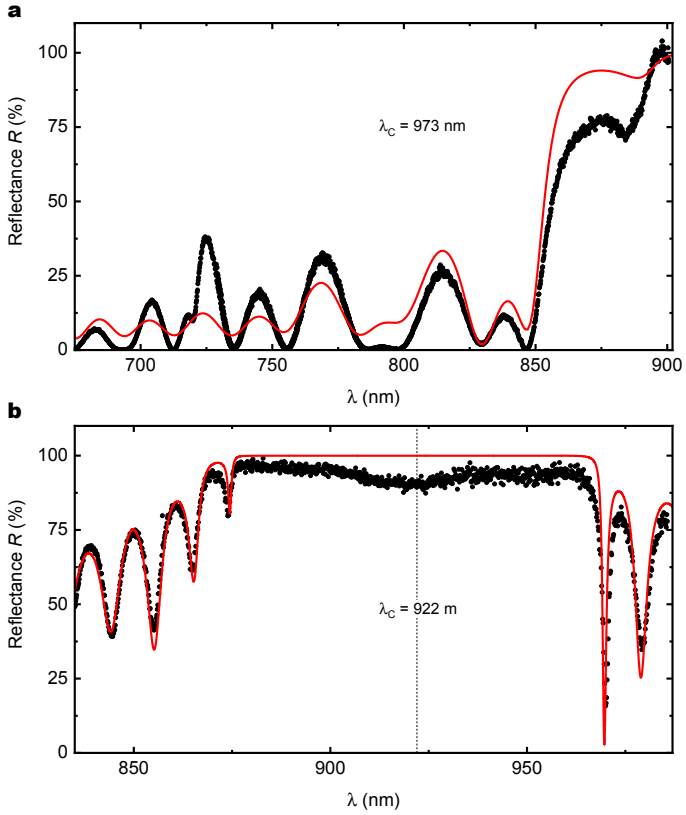

Fig. 4.2. Mirror characterisation via reflection measurements. Each mirror is investigated at $T = 4.2\,\mathrm{K}$ by recording white light (fibre-coupled white LED or halogen lamp) reflected off the sample on the spectrometer using a dark-field confocal microscope [40]. Via 1D transfer matrix methods (The Essential Macleod), the designed layer thicknesses can be refined to fit the experimentally observed oscillations outside the stopband. **a**, Curved dielectric DBR with 22 pairs of SiO_2/Ta_2O_5, terminated with SiO_2. The reflected signal is recorded on a flat surface away from the curved microstructure and normalized by the white light spectrum (an exponentially decaying function based on the measured signal reflected off the metallic mirror in **b**). **b**, Unpassivated nip-DBR. Here, the reflectance is obtained normalizing the DBR's reflected signal by the signal reflected from an Au contact pad on the same DBR (by moving piezo-nanopositioner laterally by a few microns).

spectrometer [40]. In order to determine the reflectance of each mirror across a wavelength range that includes several oscillations outside the SB ("SB oscillations"), we use the reflected light from a metallic mirror (which in our case is the Au contact pad on the nip-DBR) to record a reference spectrum. The nip-DBR's reflectance spectrum is obtained by normalizing its reflected signal by the reference spectrum. Due to the absence of a metallic reference surface on top of the dielectric DBR in Fig. 4.2a, an exponential fit of the reference spectrum from Fig. 4.2b is used instead and the maximum reflectance is normalized to 1. Due to the fact that all reflectance spectra obtained on

any surface depends on the settings of the microscope and exact Z-position of the beam focus, the exponential reference spectrum for Fig. 4.2a inevitably leads to a larger discrepancy between the modelled and measured reflectance curves in Fig. 4.2a compared to Fig. 4.2b.

Via 1D transfer matrix methods (The Essential Macleod) the designed layer thicknesses can be refined in order to fit the experimentally observed SB oscillations. The obtained model for each DBR (red solid lines in Fig. 4.2) can be used to simulate the cavity performance, in particular to calculate $\mathcal{Q}$-factors and transmittance values at resonance for different wavelengths by adjusting the vacuum-gap between the mirrors (Appendix B). The slight discrepancy in the obtained reflectance in Fig. 4.2b with respect to the model comes from the fact that the collection efficiency of the confocal microscope is highly dependent on the Z-position of the focus – which is different for the nip-DBR and Au contact pad not only due to different focus penetration depths but different Z-positions of the Au and GaAs surface itself.

4.5 Microcavity characterisation: $\mathcal{Q}$-factors

A microcavity is built using passivated and unpassivated nip-DBRs and curved dielectric DBRs ($R \sim 7$–$16\,\mu$m) similar to the ones characterized in Fig. 4.2. Via laser transmission measurements at the Si photodetector below the nip-DBR, each microcavity is characterised by determining its $\mathcal{Q}$-factor across the nip-DBR's SB. The transmission signal is measured as a function of laser wavelength keeping the cavity length fixed (Fig. 4.3a). To change the cavity's resonance frequency, the mirror separation is changed by means of the Z nano-positioner.

A $\mathcal{Q}$-factor is obtained for every pair of longitudinal (TEM_{00}) modes at minimum mirror separation of ~ 2–$4\,\mu$m (depending on wavelength and mirror depression depth [53]) by fitting a double-Lorentzian. Fig. 4.3a,b show the results for an electrically contacted passivated sample* (black circles), a unpassivated bare wafer sample without contacts (blue triangles) as well as an unpassivated sample with contacts (red squares). Around the SB centre, where the coupling to the QD layer is maximised ($\lambda_\mathrm{C} = 915$–$925\,$nm), the $\mathcal{Q}$-factor experiences an increase of almost two orders of magnitude after surface passivation. In Fig. 4.3c, extracted absorption coefficients α from the model (Appendix B) are plotted for single datasets of Fig. 4.3b.

The drastic increase of that the $\mathcal{Q}$-factors after surface passivation inevitably leads

*Note that the measured $\mathcal{Q}$-factors obtained with a passivated contacted sample or a passivated bare wafer piece were similar, which is why the latter are not shown in Fig. 4.3b.

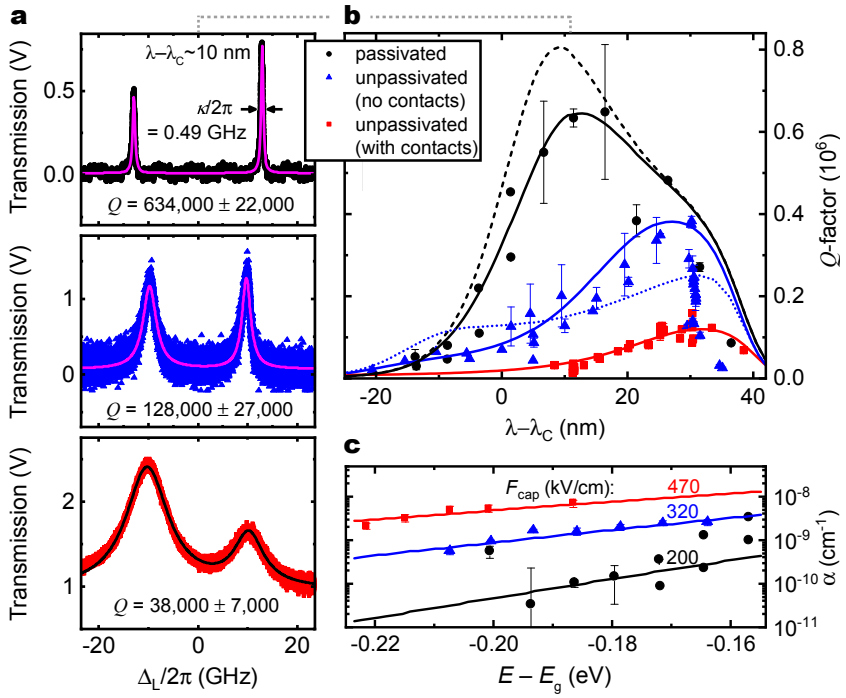

Fig. 4.3. Microcavity characterisation via $\mathcal{Q}$-factor measurements. Microcavities with three different nip-DBRs are tested at $T = 4.2\,\mathrm{K}$: a passivated DBR with contacts (black circles), an unpassivated DBR "A" without contacts (blue triangles) and an unpassivated DBR "B" with contacts (red squares). **a**, Measured transmission signal from a laser at $\lambda - \lambda_\mathrm{C} \sim 10\,\mathrm{nm}$ as a function of laser detuning at a fixed (minimum) mirror separation. In each case a mean $\mathcal{Q}$-factor for the two longitudinal modes is determined by a double-Lorentzian fit (solid lines). **b**, Evaluated $\mathcal{Q}$-factors for several wavelengths. In both unpassivated cases, two (A) and six (B) datasets from similar microcavities ($\lambda_\mathrm{C} = 915$–$925\,\mathrm{nm}$) are overlapped. The solid (dashed) lines are calculated $\mathcal{Q}$-factors taking into account free-carrier absorption coefficients based on literature [62] and calculated Franz-Keldysh absorption coefficients [75, 76] for electric fields $F_\mathrm{cap} = (200, 320, 470)\,\mathrm{kV/cm}$ ($F_\mathrm{cap} = 0$) in the capping layer. A maximum $\mathcal{Q}$-factor increase of almost two orders of magnitude is found comparing the model curves for passivated and unpassivated samples with contacts. In order to rule out surface scattering [79] as the dominant absorption mechanism, the blue dotted line indicates the calculated $\mathcal{Q}$-factors taking into account a GaAs surface roughness of $\sigma = 0.5\,\mathrm{nm}$ (Fig. 4.5b) instead of F-K absorption. **c**, Determined absorption coefficients of the capping layer (single datasets only). By comparing the measured and simulated $\mathcal{Q}$-factors, an extinction coefficient k for the capping layer material (GaAs) can be fitted yielding an absorption coefficient α via $\alpha = 4\pi k/\lambda$. The solid lines are fitted absorption values based on the Franz-Keldysh effect [75, 76] (Eqs. 4.1–4.5).

to the conclusion that the losses limiting the $\mathcal{Q}$-factors of unpassivated microcavities are related to the semiconductor surface: they either originate from the semiconductor surface itself or the GaAs layer below the surface, the capping layer.

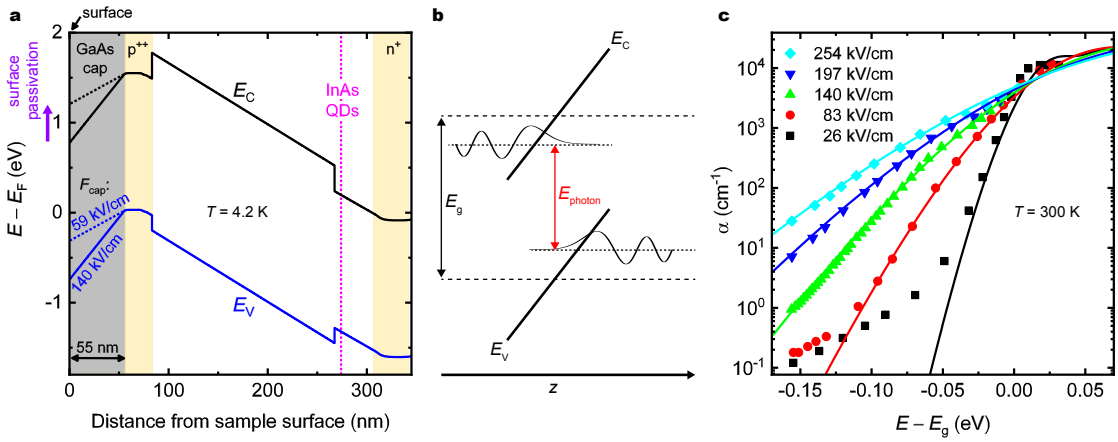

Fig. 4.4. Simulated nip-DBR band structure and Franz-Keldysh effect. **a**, Simulation of the conduction and valence band in the n-i-p diode (nextnano) at $T = 4.2\,\mathrm{K}$. The surface is modelled via a Schottky barrier of $E_\mathrm{g}/2 = 0.76\,\mathrm{eV}$ reflecting the mid-gap Fermi-level pinning at the GaAs surface [77]. The effect of surface passivation is modelled via a reduced Schottky barrier of 0.32 eV taking into account the experimentally observed factor of 2.4 reduction of the electric field in the capping layer after surface passivation. **b**, Schematic of the Franz-Keldysh effect [72, 73]. An electric field inside a semiconductor, i.e. a tilted conduction-(valence-)band edge, allows for electrons (holes) to tunnel into the forbidden energy gap E_g, leading to below-gap absorption processes. **c**, Room-temperature Franz-Keldysh absorption coefficients reported in literature [76] for different electric fields inside a p-i-n double heterostructure. The solid lines correspond to calculated absorption coefficients according to Ref. [74, 75] (Eqs. 4.1–4.5).

4.6 Microscopical explanation for the nip-DBR losses

As a last step, we give a possible microscopical explanation for the losses in the investigated nip-DBRs and why surface passivation significantly reduces them. In Fig. 4.4a, the calculated valence- and conduction-band edges in the heterostructure are shown, a solution to the 1D poisson equation (obtained via the nextnano software). In the unpassivated case, we simulate the mid-gap Fermi-level pinning via a Schottky barrier of 0.76 eV on the sample surface. This yields an electric field in the capping layer ("capping field") of $F_\mathrm{cap} = 140\,\mathrm{kV/cm}$. The effect of surface passivation is modelled via a reduced Schottky barrier of 0.32 eV taking into account the experimentally observed factor of 2.4 reduction of the electric field in the capping layer after surface passivation.

An electric field inside a semiconductor leads to F-K absorption below the bandgap of the material [72, 73]: due to a tilt in valence- and conduction-band edges, the electron and hole wavefunctions can be described by Airy functions (similar to a particle in a triangular well [80]) with an exponential tail in the forbidden bandgap. This increases the overlap of the electron and hole wavefunctions within the bandgap, which leads to

absorption processes at photon energies $E_{\mathrm{photon}} < E_{\mathrm{g}}$. The situation is schematically depicted in Fig. 4.4b.

According to Ref. [74], F-K absorption at energy E due to the presence of an electric field F can be described via the absorption coefficient

$$\alpha(E,F) = \frac{2\pi e^3}{ncm_0^2\hbar}\cdot\frac{F}{E}\sum_{i=\mathrm{lh,hh}}\frac{\mu_i|M_i|^2}{\hbar\theta_i}\Big(|\mathrm{Ai}'(x_i)|^2 - x_i|\mathrm{Ai}(x_i)|^2\Big), \tag{4.1}$$

where

$$\hbar\theta_i = \Big(\frac{(eF\hbar)^2}{2\mu_i}\Big)^{1/3}, \tag{4.2}$$

$$x_i = \frac{E_{\mathrm{g}} - E}{\hbar\theta_i}, \tag{4.3}$$

e being the elementary charge, n the refactive index, c the speed of light in vacuum, m_0 the free electron rest mass, $\mu_{\mathrm{lh}} = 0.037m_0$ ($\mu_{\mathrm{hh}} = 0.058m_0$) the reduced mass of an electron–light-hole pair (electron–heavy-hole pair) and $|M_{\mathrm{lh}}|^2$ ($|M_{\mathrm{hh}}|^2$) the momentum matrix elements for the light (heavy) holes. $\mathrm{Ai}(z)$ is an Airy function* (with derivative $\mathrm{Ai}'(z)$).

We make use of the momentum matrix elements derived in Ref. [75] for different polarisations of the radiation field. For light polarised in the XY plane, the momentum matrix elements for the light and heavy holes read

$$|M_{\mathrm{lh}}|^2 = P^2/3, \tag{4.4}$$

$$|M_{\mathrm{hh}}|^2 = P^2, \tag{4.5}$$

where $P = 0.692$ is a typical value for GaAs [75].

The model for F-K absorption is fitted to room-temperature experiments on a p-i-n double heterostructure [76] (Fig. 4.4c). There is a compelling overlap between theory and experiment. Small discrepancies are discussed below.

In order to estimate F-K absorption coefficients in our nip-DBR at 4.2 K (Fig. 4.3b,c), we make use of Eqs. 4.1–4.5 and an adjusted GaAs bandgap of 1.519 eV. Comparing the obtained model for low-temperature F-K absorption to the experimental data presented in Fig. 4.3b,c, we fit capping fields a factor of 3.4 above the one expected from the 1D poisson equation (Fig. 4.4a) in the unpassivated case. The origin of this discrepancy is not fully understood at this point, however we note several points here.

*The Airy function $\mathrm{Ai}(z)$ is defined as $\mathrm{Ai}(z) = \frac{1}{2\pi}\int_{-\infty}^{\infty} e^{i(zt+t^3/3)}dt$.

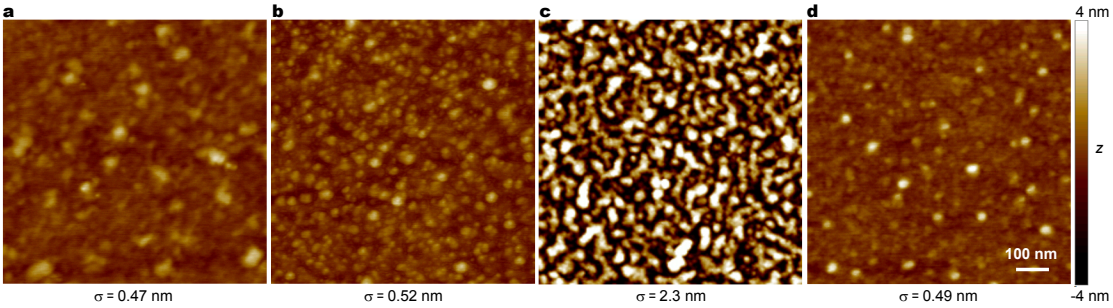

Fig. 4.5. Atomic force microscropy (AFM) images of different semiconductor samples. Each image depicts the same scan area of $0.8 \times 0.8\,\mu\text{m}^2$ (obtained in tapping mode) and scale bar from a height of -4 to 4 nm. **a**, Passivated bare wafer piece. **b**, Unpassivated bare wafer piece (no contacts). **c**, Unpassivated sample with contacts. **d**, Undoped semiconductor DBR (unpassivated). The samples in **a**, **b** and **d** reveal similar rms surface roughnesses around $\sigma = 0.5\,\text{nm}$, while the sample shown in **c** exhibits a larger roughness around $\sigma = 2\,\text{nm}$.

First, there are no F-K absorption experiments reported in literature at low temperature (4.2 K) far below the bandgap E_g of GaAs (at $E - E_\text{g} \sim -0.17\,\text{eV}$ corresponding to $\lambda \sim 920\,\text{nm}$). Our approach here is to fit the theory presented in Ref. [74, 75] to the room-temperature experiments of Ref. [76] (Fig. 4.4c) and extrapolate the absorption coefficients to 4.2 K and $\sim 0.17\,\text{eV}$ below the corresponding GaAs bandgap of 1.519 eV. We already see from this fit that the overlap of the experimentally found below-gap absorption coefficients in Ref. [76] with the F-K theory decreases as the energy E decreases; the exponential reduction of the absorption coefficient below the bandgap flattens out with decreasing energy [76].

Secondly, there are room-temperature experiments on F-K oscillations (FKOs) in similar GaAs heterostructures than reported in this work (a 25–80 nm thick, undoped GaAs capping layer on top of an n^+-doped $Al_{.32}Ga_{.68}As$ layer [81]) that report surface electric field values a factor 1.8–3.8 above the expected ones, too*.

A remaining question is why the bare wafer sample without passivation shows higher $\mathcal{Q}$-factors than the electrically contacted sample without passivation. We speculate that the F-K effect (i.e. the capping field) is reduced due to the higher surface quality (similar surface-density of states but spread differently in energy, thus a reduced Fermi-level pinning [77]) of the bare wafer sample compared to the unpassivated, contacted nip-DBR.

This statement is based on atomic force microscopy (AFM) measurements performed in tapping mode (Bruker Dimension 3100) on the different samples presented in this

*In order to estimate the capping fields in Ref. [81], we simply divide the capping layer thicknesses reported in [81] by half the bandgap $E_\text{g}/2 = 0.71\,\text{eV}$ of GaAs at 300 K.

chapter: the bare wafer sample exhibits a similar surface texture and roughness of $\sigma \sim 0.5\,\mathrm{nm}$ (Fig. 4.5b) than the investigated undoped semiconductor DBR (Fig. 4.5d), but much less surface texture and lower roughness than the unpassivated, contacted nip-DBR (Fig. 4.5c). Still, this surface roughness of $\sigma \sim 0.5\,\mathrm{nm}$ introduced in the model does not account for the measured low $\mathcal{Q}$-factors of the bare wafer sample at the SB centre (Fig. 4.3b, blue dotted line).

Note that a surface roughness σ translates into a total integrated scatter (TIS) of TIS $\approx (4\pi\sigma/\lambda)^2$ [82] and can be modelled by an extinction coefficient k (for the 1D transfer matrix methods) according to Ref. [79],

$$k = \frac{\pi(n_1 - n_2)^2(n_1 + n_2)d}{\lambda\sqrt{8(n_1^2 + n_2^2)}}, \tag{4.6}$$

where $d = 2\sigma$ is the thickness of the scatter layer corresponding to twice the rms surface roughness σ, n_1 and n_2 are the refractive indices of the two layers surrounding the scatter layer and λ is the free-space wavelength.

4.7 Comparison to an undoped semiconductor DBR

In order to confirm that the losses obtained with a doped semiconductor DBR are indeed a consequence of the gates, we compare our results to a microcavity consisting of an undoped semiconductor DBR. The heterostructure in this case is a λ-layer of GaAs (with embedded InAs QDs in the centre) on top of a 33-pair AlAs/GaAs DBR [49, 52]. First, we repeat the mirror characterisation procedure described above and find a suitable model for the semiconductor layer thicknesses (Fig. 4.6a). Then, we pair this mirror with the same dielectric top mirror used for the experiments with the doped semiconductor DBR. Fig. 4.6b depicts the measured $\mathcal{Q}$-factors as a function of wavelength.

We find that in this case, surface scattering due to a measured GaAs surface roughness of $\sigma \sim 0.5\,\mathrm{nm}$ (Fig. 4.5d) via AFM can explain the observed reduction of $\mathcal{Q}$-factors around the semiconductor's SB centre (solid line in Fig. 4.6b). The measurements with the nip-DBR however show that surface scattering is irrelevant. To explain this, we speculate that either the surfaces of both doped and undoped wafers are not identical or that the losses in the undoped semiconductor DBR arise from AlAs/GaAs interface roughness [83]. The first statement is based on the fact that the undoped semiconductor wafer was not grown with the same MBE than the nip-DBR. The second statement is based on simulations that take into account an interface roughness of $\sigma = 1.0\,\mathrm{nm}$ on top of each AlAs layer (dotted line in Fig. 4.6b) instead of a rough surface – yielding a

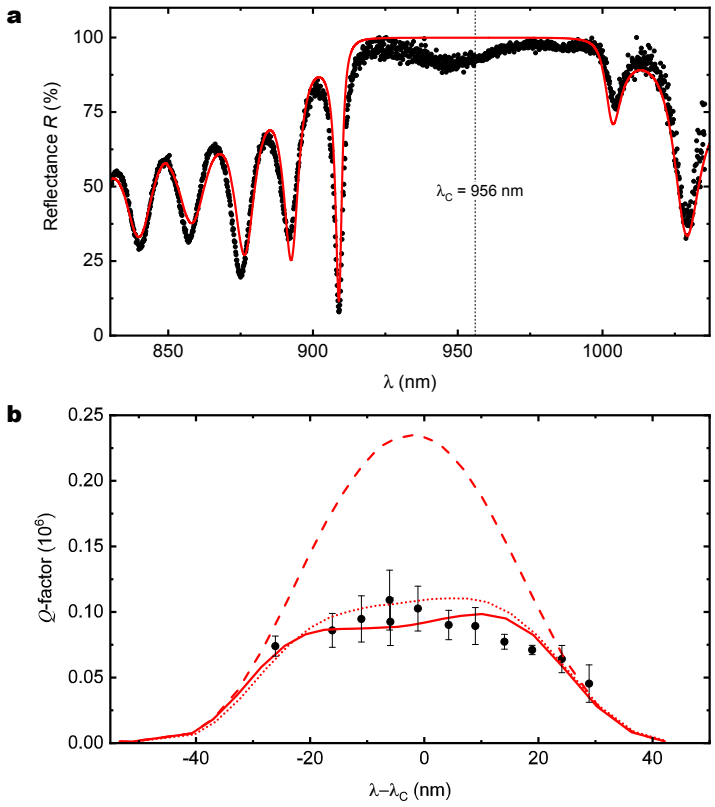

Fig. 4.6. Undoped semiconductor DBR: reflectance and $\mathcal{Q}$-factor measurements. **a**, Reflectance measurement of an undoped semiconductor DBR ($\lambda_C = 956\,\text{nm}$) at $T = 4.2\,\text{K}$. The DBR contains a λ-layer of GaAs and QDs embedded $\lambda/2$ below the surface on top of 33 pairs of AlAs($\lambda/4$)/GaAs($\lambda/4$). In order to record a reference spectrum from a metallic mirror here, parts of the sample were covered by an Au film using electron-beam evaporation. **b**, Measured $\mathcal{Q}$-factors of a microcavity at $T = 4.2\,\text{K}$ consiting of an undoped semiconductor DBR paired with a dielectric top mirror ($\lambda_C = 973\,\text{nm}$). In **b**, the reduction of $\mathcal{Q}$-factors around the SB centre can be explained by a semiconductor surface roughness of $\sigma = 0.5\,\text{nm}$ (solid line) or an interface roughness of $\sigma = 1.0\,\text{nm}$ on top of every AlAs layer (dotted line). The dashed line corresponds to the case without any losses in the semiconductor DBR.

similar result.

We note that although the measured $\mathcal{Q}$-factors with the undoped semiconductor DBR can be modelled by surface scattering alone, we have no experimental data to proof that the losses there originate indeed from the surface – we speculate that the surfaces of both wafers are not exactly identical.

Finally, we stress that the model for surface scattering can in no way reproduce the extreme (exponential) wavelenegth dependence of the measured $\mathcal{Q}$-factors in the doped nip-DBR (Fig. 4.3b, blue dotted line) – due to the weak wavelength dependence of the

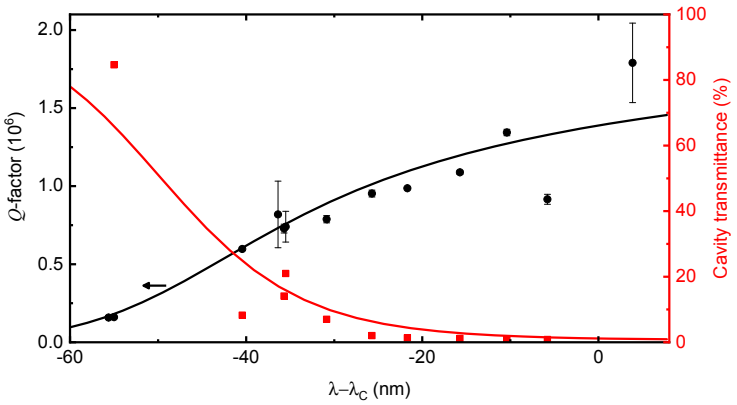

Fig. 4.7. Measured Q-factors and cavity transmittance of a purely dielectric microcavity. Dielectric top mirror ($\lambda_C = 973\,\text{nm}$) paired with a dielectric bottom mirror (shifted to $\lambda_C = 976\,\text{nm}$) of same coating at $T = 300\,\text{K}$. The black (red) solid line is a calculation of the $\mathcal{Q}$-factor (cavity transmittance) taking into account a material extinction coefficient of $k_{SiO2} = 4 \cdot 10^{-7}$ and $k_{Ta2O5} = 4.5 \cdot 10^{-7}$ for SiO_2 and Ta_2O_5, respectively [70]. Additionally, an interface roughness of $\sigma = 0.25\,\text{nm}$ above each of the five last grown Ta_2O_5 layers and $k = 4k_{Ta2O5}$ in the last grown Ta_2O_5 layer are heuristically introduced in order to fit the experimental data. A cavity transmittance is measured relating the transmitted power at resonance to the laser power before the objective lens times a fitted in-coupling efficiency of 59%.

TIS ($\sim 1/\lambda^2$). Not even a different model based on Rayleigh scattering (wavelength dependence $\sim 1/\lambda^4$) would account for the steep decrease of the measured $\mathcal{Q}$-factors towards the SB centre. An exponential wavelength dependence of the absorption losses is the most plausible one.

4.8 Model for the curved dielectric mirror

Fig. 4.7 shows the measured $\mathcal{Q}$-factors of a purely dielectric microcavity (identical coatings on top and bottom DBR, but bottom shifted by 3 nm*) with a maximum $\mathcal{Q}$-factor of up to $2.0 \cdot 10^6$ at the SB centre (973 nm) measured at room temperature. A rough interface below each of the five lowest Ta_2O_5 layers shown in Fig. 4.1 (extinction coefficients corresponding to an interface roughness [79] of 0.25 nm) and $k = 4k_{Ta2O5}$ inside the lowest Ta_2O_5 layer are heuristically introduced in the model to fit the measured $\mathcal{Q}$-factors and later get a reasonable model for describing the measured microcavities involving semiconductor DBRs (Fig. 4.3b,c and Fig. 4.7b).

*A relative shift of 3 nm between top and bottom mirror was introduced in order to account for the high cavity transmittance measured at low wavelengths. This is done with reason as recorded reflectance spectra (Fig. 4.2a) on different wafer samples with the same dielectric coating exhibited up to 6 nm shifts in wavelength, most probably due to thickness variations across the wafer.

Chapter 5

Fabrication methods to reduce the microcavity mode volume

Adapted from:
Daniel Najer[1,*], Martina Renggli[1,*], Daniel Riedel[1], Sebastian Starosielec[1], and Richard J. Warburton[1],
"Fabrication of mirror templates in silica with micron-sized radii of curvature",
Appl. Phys. Lett. 110, 011101 (2017).

[1]Department of Physics, University of Basel, Klingelbergstrasse 82, CH-4056 Basel, Switzerland

[*]contributed equally to this work

5.1 Summary

We present the fabrication of exceptionally small-radius concave microoptics on fused silica substrates using CO_2 laser ablation and subsequent reactive ion etching. The protocol yields on-axis near-Gaussian depressions with radius of curvature $\lesssim 5\,\mu m$ at shallow depth and low surface roughness of 2 Å. This geometry is appealing for cavity quantum electrodynamics where small mode volumes and low scattering losses are desired. We study the optical performance of the structures within a tunable Fabry-Pérot type microcavity, demonstrate near-coating-limited loss rates ($\mathcal{F} = 25\,000$) and small focal lengths consistent with their geometrical dimensions.

5.2 Introduction

The physics of single emitters strongly coupled to optical resonators offers a rich variety of quantum applications, including high-brightness indistinguishable single photon sources, single-photon transistors, and photon-mediated emitter-emitter coupling. A significant but challenging area is the application of these concepts, initially developed in the context of atomic physics, to solid-state systems such as quantum dots, nitrogen-vacancy centers in diamond or localization centers in 2D materials. The key requirements to achieve a high Purcell enhancement or a coherent exchange of energy quanta—the so-called weak and strong coupling regimes of cavity quantum electrodynamics, respectively—are a small mode volume (V, the effective extension of the confined electromagnetic field), a high resonator quality factor ($\mathcal{Q}$, the average number of coherent oscillations) as well as a precise in-situ tuning between emitter and resonator [84]. Various high-$\mathcal{Q}$ microresonator concepts exists, e.g. micropillars [9] or photonic crystal cavities [10]. The tunable Fabry-Pérot type microcavity uniquely offers full spectral and spatial tuning to the emitter [85, 86] as well as highly efficient external mode-matching in the free-beam version [52]. Already, significant emitter-cavity cooperativity has been achieved with scaled down dimensions [49]. For these tunable plano-concave microcavities, the route to high coupling rates lies within the strong confinement of the resonant mode which is achieved by reducing the curved mirror's radius of curvature (R).

5.3 Previous methods

Only a few fabrication methods are known to produce concave microoptics with radii of curvature $R \leq 5\,\mu\text{m}$, e.g. focussed ion beam (FIB) milling [87, 88], femtosecond laser wet etching [89] and proximity-effect-assisted reflow techniques [90]. For an optical cavity with total round-trip losses L_{tot} and ultra-high finesse $\mathcal{F} \approx \pi/L_{\text{tot}} \approx 10^5$, acceptable round-trip scattering losses are below $S \approx (4\pi\sigma/\lambda)^2 = 30\,\text{ppm}$, setting the upper limit for the surface roughness to a demanding $\sigma = 2 \ldots 6\,\text{Å}$ in the VIS–NIR spectral range [91]. The two latter approaches suffer from a too high surface roughness on the scale of a few nanometers. For FIB milling, microoptics fabrication benefits from full shape control and low surface roughness, and indeed depressions with curvatures as low as $R = 1.5\,\mu\text{m}$ have been reported recently [87]. Yet FIB represents a production method at significant investment costs.

CO_2-laser ablation on silica has turned out to be a low-cost alternative providing near-Gaussian shaped concave depressions at ultra-low surface roughness. In the conventional

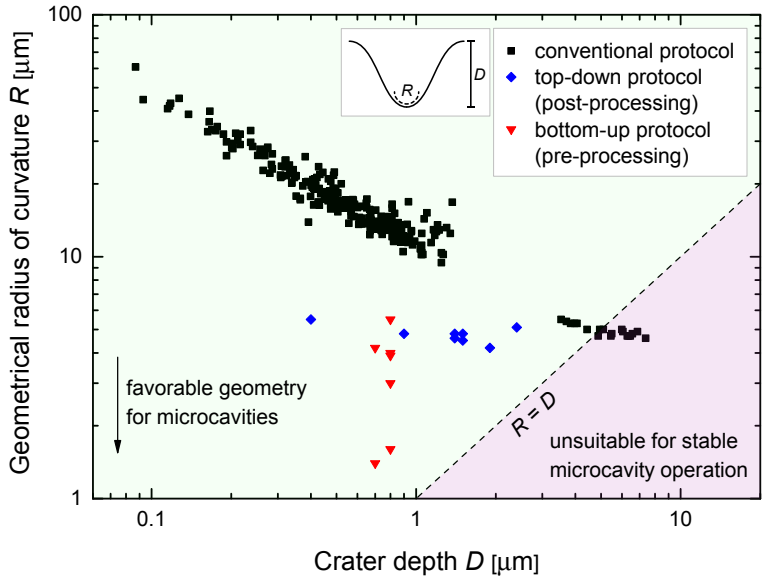

Fig. 5.1. Geometry parameters of craters produced by different fabrication methods. Conventional CO_2-laser ablation on polished fused silica substrates (black dots) shows a strong correlation between geometrical radius of curvature R and depth D. Reproduced from Ref. [53], with the permission of AIP Publishing. In this work, the favourable regime of low R at shallow D becomes accessible by both post-processing ("top-down", blue dots) and pre-processing ("bottom-up", red dots) methods with a minimum radius of curvature $R = 1.2 \pm 0.1\,\mu\text{m}$.

fabrication protocol, short pulses of CO_2 laser light are focussed onto either a polished fused silica substrate or the end facet of an optical fibre [54]. At these wavelengths ($\lambda \approx 10\,\mu\text{m}$), the light is efficiently absorbed by the material. While the dynamics of the process are complex, the following phenomenological description is well accepted: above a certain local temperature threshold, local evaporation results in a concave landscape roughly following the spatial irradiance distribution. The strong surface tension of the molten material then leads to a very smooth solidification process, with excellent surface roughness routinely at $1 \ldots 2\,\text{Å}$ [53, 54].

The established CO_2-laser ablation process can produce a large range of depression geometries (black dots in Fig. 5.1), yet with a strong but unfortunate correlation between radius R and depression depth D (from Ref. [53]) irrespective of varying fabrication parameters (intensity, pulse duration and pulse train length). While the radius seems to stagnate at $R \approx 5\,\mu\text{m}$ or slightly below, a formed microcavity resonance becomes intrinsically unstable for cavity lengths $L > R$ (or $2R$) in a plano-concave (or biconcave) geometry from Gaussian optics theory. In practice, the finite lateral extent of the mirrors makes this transition between stable and unstable cavity modes less abrupt. In addition,

deviations of the concave mirror surface geometry from the isophase plane of the cavity field can induce a mode-mixing between transversal modes [92], acting as additional loss channels and further restricting the stability region to $L \lesssim R/2$. Those constraints further limit the established ablation protocol to geometries of $R \gg 5\,\mu\text{m}$.

5.4 Two new methods

In this work we present a post-processing ("top-down") protocol which lifts this rigid link between radius and depth in the conventional ablation method. The key concept is to introduce an etch step post-ablation to reduce the crater depth, while preserving the high-grade geometry of the conventional ablation. In addition, we demonstrate first steps towards greater shape control at very small radii by pre-processing the substrates (a "bottom-up" approach) with standard photolithography and subsequent CO_2-laser polishing. While optical polishing has been demonstrated [93, 94] with convex features down to 9.4 µm in radius [95], our bottom-up approach achieves much smaller radii, down to 1.2 µm. We characterize the structures formed by both protocols by confocal scanning microscopy and atomic force microscopy, and find radii of curvature $R \approx 5\,\mu\text{m}$ at shallow depths $D \approx 1\,\mu\text{m}$, as shown in Fig. 5.1 (blue and red dots). We apply a reflective coating to our structures and record optical transmission spectra of the formed microcavities. We verify the geometrical radii and show high-$\mathcal{Q}$ performance of a microcavity fabricated by the top-down protocol.

5.5 Protocol 1: top-down approach

The top-down approach is based on the conventional ablation method in the regime of large depth and small radius ($R \approx 5\,\mu\text{m}$) followed by a post-processing etching step to reduce the large depth by means of reactive ion etching (RIE), see Fig. 5.2(a–e). After initial ablation with an FWHM beam diameter of 20 µm (a), the depression is spin-coated with AZ1512HS photoresist (Microchemicals, Germany), which partially reflows into the depression (b). The first RIE etching step (Ar/O_2) has a preferred selectivity towards the photoresist, and after calibrated removal leaves a self-centered mask at the crater center (c). The second RIE step ($CHF_3/Ar/O_2$) preferentially etches the exposed silica substrate and thus reduces the effective depth of the ablation crater, while the crater center's ultralow-roughness surface and geometry are protected (d). A standard solvent stripping of the residual photoresist then reveals the original ablation crater bottom with radius $R \approx 5\,\mu\text{m}$ at a reduced depth of $D \approx 1\,\mu\text{m}$ with unaffected surface quality (e).

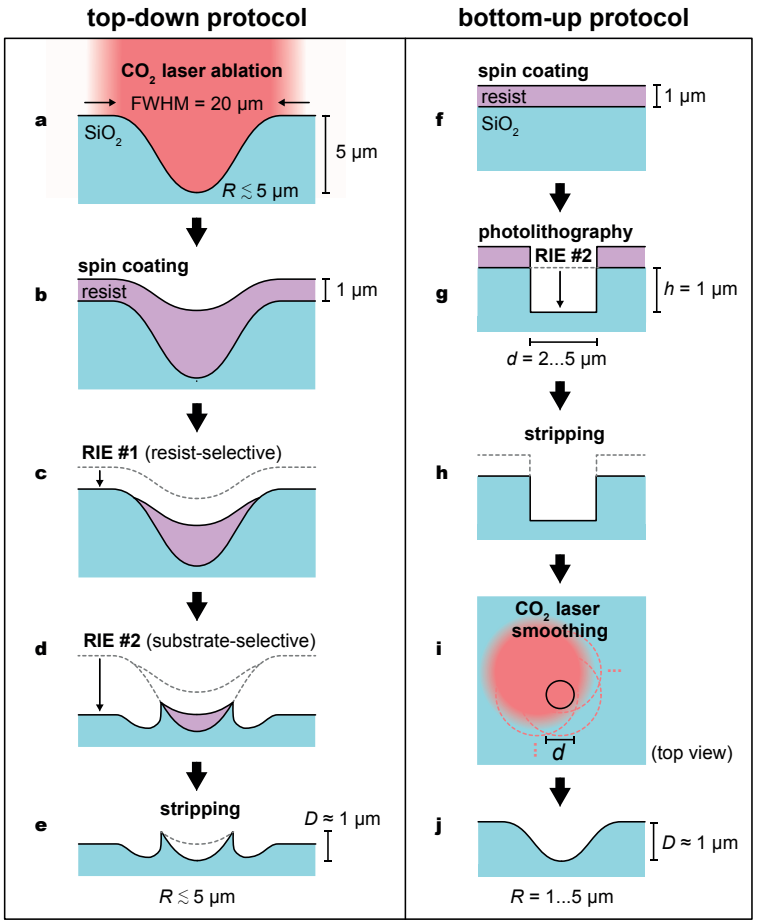

Fig. 5.2. Protocol for both processing schemes. **a**, The top-down approach starts from a small-radius crater at large depth produced by conventional high-power CO_2-laser ablation with an FWHM beam diameter of 20 µm. **b**, With spin-coating of photoresist, the crater becomes partially filled. **c**, Reactive ion etching (RIE) with high selectivity for the resist consumes the resist homogeneously, implementing a self-centered mask for the crater. **d**, A second RIE step of low resist-selectivity attacks the exposed silica substrate, reducing the crater's depth. **e**, Stripping of the residual resist produces a crater at reduced depth, maintaining the original surface quality. **f**, **g** and **h**, The bottom-up approach starts from a flat silica substrate, where a step-like crater template is formed by conventional photolithography. **i**, **j**, A coarsely scanned low-power CO_2 laser locally melts the silica surface smoothing out the template shape into the desired form.

Both RIE step durations are calibrated to the spin coating thickness, crater depth, and their corresponding etching rates.

5.6 Protocol 2: bottom-up approach

The bottom-up approach, a first step towards shape control at $R \ll 5\,\mu\text{m}$ using CO_2-laser ablation, relies on the optical polishing effect [96] on a pre-structured fused silica substrate. With low irradiation, ablation becomes negligible whereas surface-tension-induced smoothing remains effective [97]. The protocol is sketched in Fig. 5.2. Photoresist (AZ1512HS) is spun onto a flat silica substrate (f) and locally removed by means of standard photolithography in order to expose the underlying silica for a substrate-selective RIE step ($CHF_3/Ar/O_2$) (g). After dissolving the residual resist, a binary structure with well-controlled width d and height h results (h). The pre-structured substrate is then optically polished by coarsely scanning the low intensity CO_2-laser irradiation (i) over the fabricated areas. Phenomenologically, the polished surface profile can be well described by a convolution of the template pattern with a Gaussian kernel of a remarkably small RMS width parameter ($s = 0.4 \ldots 1\,\mu\text{m}$). For given s and target radius R we analytically estimate optimal template parameters (d,h) for a target paraboloid-like shape, i.e. we aim at creating a target depression shape with vanishing fourth order derivative at the crater center. For production values $s = 1\,\mu\text{m}$ and target $R = 3\,\mu\text{m}$ the best estimates of the feature dimensions are $d = 3.5\,\mu\text{m}$ and $h = 1.0\,\mu\text{m}$, a binary pattern easily accessible by standard photolithography.

Both protocols yield depressions with a small geometrical R at shallow depth suited for a stable microcavity. For the main top-down protocol, the near-Gaussian shape, the low surface roughness as well as the high axial symmetry originating from the initial ablation process is well conserved. The prototype bottom-up protocol results in features with remarkably small radii $R = 1 \ldots 5\,\mu\text{m}$ while exhibiting a reduced axial symmetry and a slightly increased surface roughness. We argue that these problems can be eliminated with a better smoothing procedure, as pointed out below.

5.7 Geometrical analysis

We investigate the geometrical shape of the fabricated craters with confocal scanning microscopy and the surface roughness by atomic force microscopy. We describe the surface profile $z(r)$ as a function of radial displacement r by means of a modified ellipsoid,

$$z(r) = \frac{r^2/R}{1 + \sqrt{1 - \epsilon\, r^2/R^2 + \delta\, r^4/R^4}}\,, \tag{5.1}$$

where R represents the geometrical radius of curvature, and the dimensionless parameter ϵ is related to the conicity of the ellipsoid (e.g. $\epsilon = 1$ for a sphere, and $\epsilon = 0$ for a

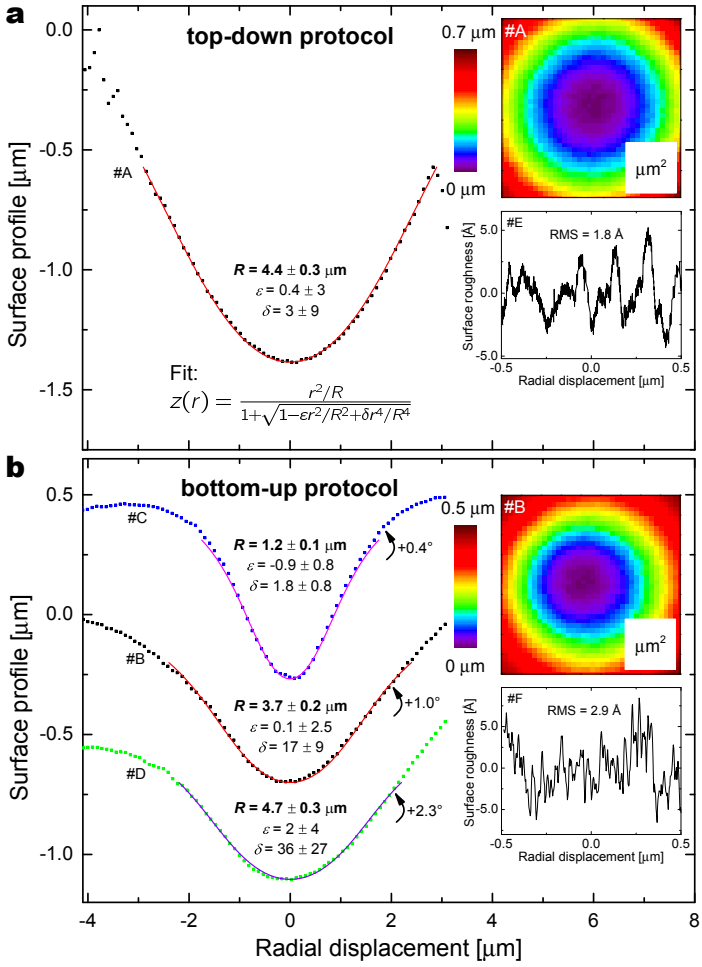

Fig. 5.3. Geometrical characterisation. Line scans (points) through top-down (**a**) and bottom-up (**b**) craters measured by confocal microscopy (blue and green curves shown with an offset). Axial asymmetry is compensated by introducing a small tilt to the data before fitting (see curved arrows). The solid lines depict cuts through the fits in which the surface is modelled by a modified ellipsoid $z(r)$. The uncercainty in the fitting parameters accounts for the variation on the fitting range around the center of the craters ($3 \ldots 6\,\mu\text{m}$). The insets show contour plots (non-tilted data) and AFM surface roughness measurements of selected craters revealing atomically smooth surfaces.

paraboloid). An ellipsoid is often used in the quantitative description of spherical and aspherical surfaces (e.g. ref. 91 and 98), however this description becomes inappropriate at large r when the optical surface converges into the unmachined flat substrate. We thus heuristically modify the ellipsoid description by another dimensionless parameter $\delta > 0$ to respect the surface asymptotics at $r \gg R$. For $r \ll R$ the ellipsoid is recovered.

Line scans through the center of craters #A (fabricated by the top-down protocol), #B, #C and #D (fabricated by the bottom-up protocol) are shown in Fig. 5.3. As

seen from the area scan (insets), top-down crater #A exhibits a high axial symmetry, while the axial symmetry of bottom-up crater #B is slightly reduced. In order to fit the axially symmetric model to the bottom-up craters and extract the relevant geometric parameters, we apply a small tilt (up to 2.3°) to the profile data. As a result we retrieve $R^{\#A} = 4.4 \pm 0.3\,\mu\text{m}$ for a top-down crater and $R^{\#B} = 3.7 \pm 0.2\,\mu\text{m}$ for a bottom-up crater. The surface roughness measured by atomic force microscopy is 1.8 Å (top-down crater #E*) and 2.9 Å (bottom-up crater #F).

5.8 Optical analysis

For optical characterization of the radius, the fabricated craters are coated with Ti(5 nm)/Au(80 nm) by electron beam evaporation and paired with a polished silica substrate (with same coating) to form a tunable Fabry-Pérot type microcavity. The cavity transmission, with respect to length detuning induced by a piezo nanopositioner, is then measured (see Fig. 5.4) at wavelength $\lambda = 940\,\text{nm}$. From Gaussian optics, TEM_{qnm} resonator modes appear at cavity lengths

$$L_{qnm} = \left(q + \frac{n+m+1}{\pi} \cos^{-1} \sqrt{g} \right) \frac{\lambda}{2} \,, \tag{5.2}$$

where q is the longitudinal mode index and n, m are the transversal mode indexes. In the plano-concave cavity geometry, the confocal parameter is $g = 1 - L_{qnm}/R_{\text{eff}}$, which itself depends on the cavity length and allows for the extraction of an effective radius of curvature R_{eff}.

As the mode overlap of the probing Gaussian laser beam to TEM_{q00} is largest, an identification of the fundamental cavity modes ($n + m = 0$) is straightforward. An intentionally poor mode-matching reveals the higher-order transversal cavity modes ($n + m \geq 1$) whose degeneracy is slightly lifted, indicating a small axial asymmetry of the crater. The (integer) longitudinal mode index q is extracted from a wavelength detuning $\Delta\lambda$ ($\lambda = 918 \ldots 974\,\text{nm}$) and corresponding resonance shift ΔL via $q = \lfloor 2\Delta L/\Delta\lambda \rfloor$, where the non-integer residual of the right hand side originates from the $n + m + 1$ contribution. The cavity length L is calibrated from the experimental control parameter (the nanopositioner's piezo voltage) by extrapolation of the resonance modes to the (unphysical) limit $n + m + 1 \to 0$ where $L_{qnm} \equiv q\lambda/2$. For each individual mode L_{qnm} an effective radius R_{eff} of curvature can be determined, with an uncertainty induced by

*The tested top-down crater #E belongs to an earlier fabrication batch than #A, where the photoresist was manually applied as a droplet. The resulting geometry, i.e. radius and depth, remains the same

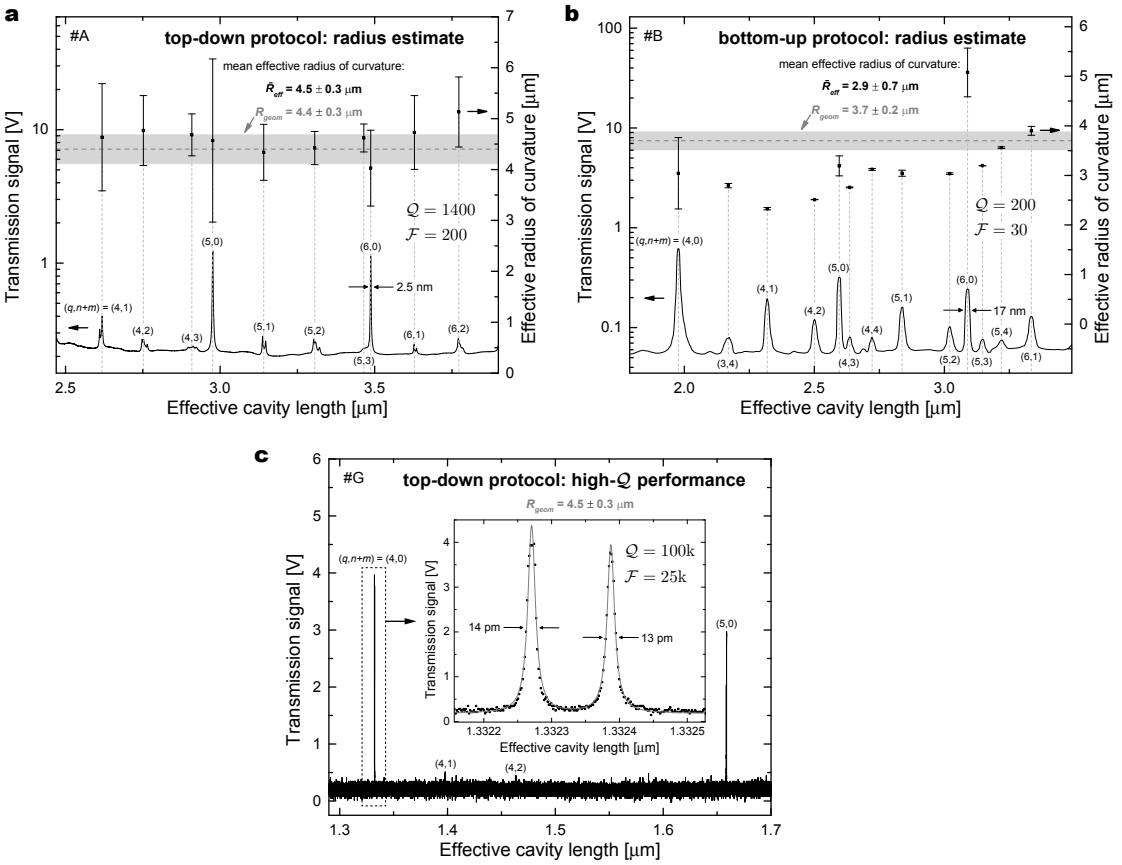

Fig. 5.4. Optical characterisation. Optical transmission spectra of tunable microcavities formed by fabricated top-down (**a**,**c**) and bottom-up (**b**) craters coated with Ti/Au by electron beam evaporation (**a**,**b**), or a Ta_2O_5/SiO_2 quarter-wave stack by ion beam sputtering (**c**). The curved mirrors are paired with a polished silica substrate with the same coating. The mode-matching in **a** and **b** is intentionally poor in order to couple the Gaussian input laser mode ($\lambda = 940\,\mathrm{nm}$) to a large number of transversal cavity modes thus enabling the transversal mode splitting to reveal an effective radius of curvature R_{eff}. The high-$\mathcal{Q}$ configuration in **c** ($\lambda = 637\,\mathrm{nm}$) shows a double-Lorentzian fine structure with a large quality factor $\mathcal{Q} = 10^5$ and high finesse $\mathcal{F} = 2.5 \times 10^4$.

the cavity length calibration procedure.

From cavity #A (formed by the main top-down protocol), a mean effective radius of $\bar{R}_{\mathrm{eff}}^{\#A} = 4.5 \pm 0.3\,\mu\mathrm{m}$ is found consistently across all probed cavity resonances (Fig. 5.4a), which closely matches the crater geometry $R^{\#A} = 4.4 \pm 0.3\,\mu\mathrm{m}$. The measured quality factor $\mathcal{Q} = 1400$ for the TEM_{600} mode translates to a mirror reflectance of 98.6 % and a finesse of $\mathcal{F} = \lambda\mathcal{Q}/2L_{\mathrm{qnm}} = 200$, typical values expected for an evaporated Au coating [99].

In contrast to these results, cavity #B (formed by the prototype bottom-up protocol)

shows a much broader range of effective radii with a mean of $\bar{R}_{\mathrm{eff}}^{\#B} = 2.9 \pm 0.7\,\mu\mathrm{m}$ and significantly lower quality factors ($\mathcal{Q} = 200$ for the TEM_{600} mode resulting in $\mathcal{F} = 30$). While the mean effective radius lies significantly below the top-down threshold (5 µm), which is also apparent from the geometrical analysis $R^{\#B} = 3.7 \pm 0.2\,\mu\mathrm{m}$, the strong fluctuation with cavity length indicates a deviation from a spherical geometry from the paraxial Gaussian beam theory. The reduction in the $\mathcal{Q}$ of the bottom-up cavity likely arises from an axial asymmetry and waviness which coincides with the coarse-scanned pitch (4 µm) of the optical polish matrix. We expect this defect to be considerably lifted by a finer pitch in a refined fabrication run, the focus of further study.

We test the high-$\mathcal{Q}$ performance of top-down crater #G* with a commercial high-reflectivity quarter-wave stack Ta_2O_5/SiO_2 coating, produced by ion beam sputtering, at a wavelength of $\lambda = 637\,\mathrm{nm}$. In Fig. 5.4(c), two adjacent longitudinal modes $(q, 0)$ are recorded, each split into a linear-polarised fine structure likely originating from the slightly elliptical mirror surface [100]. For the TEM_{400} mode, we demonstrate a large quality factor of $\mathcal{Q} = 10^5$ and high finesse $\mathcal{F} = 2.5 \times 10^4$, very well suitable for the target applications in cavity quantum electrodynamics. The measured finesse is close to the one expected from the bare mirror reflectivity (99.9925 %, measured on a fused silica witness sample by the manufacturer).

*The tested top-down crater #G belongs to an earlier fabrication batch than #A, where the photoresist was manually applied as a droplet. The resulting geometry, i.e. radius and depth, remains the same

Chapter 6

Summary and Future Prospects

Chapter 2 and 3 of this thesis presented the realisation of a highly coherent atom-photon interface despite the complexity of the solid-state environment. From a physics point-of-view, we observe a striking vacuum Rabi-oscillation, a coherent exchange of a single quantum between the cavity and the quantum dot. Such clear oscillations have not been observed before in any system. (In the microwave domain, the absence of single-photon detectors has precluded this experiment; in the optical domain, the noise was too severe: wiggling of the atom in the trap potential in the case of cold atoms smearing out the oscillations; charge noise in the semiconductor host in the case of semiconductor quantum dots) In addition, we observe pristine anti-crossings without cavity-feeding. This allows us to probe our microcavity at high excitation powers, where the higher rungs of the Jaynes-Cummings ladder become populated. The compelling agreement with the "standard model" of cavity-QED, the Jaynes-Cummings model, is further evidence for the coherence of the presented exciton-photon interface.

From a quantum technology point-of-view, we present an extremely low-noise single photon-single "atom" interface with cooperativity $C = 150$ in a semiconductor. A high cooperativity without cavity-feeding is unprecedented for optical quantum dot devices. The cooperativity is much larger than that achieved with electrically-defined quantum dots in the microwave domain. The cooperativity is also much larger than that achieved in state-of-the-art optical experiments on single atoms.

To make this step-change in cooperativity and noise, we present several innovations. The most important is that the quantum dots are embedded in a gated structure. The gates have two consequences. First, cavity-feeding, the source of noise which has plagued almost all previous implementations of strong-coupling cavity-QED with semiconductor quantum dots, is completely eliminated. Secondly, the quantum dot linewidths are extremely close to the transform-limit: even in the microcavity structure, the linewidths match the very best quantum dot linewidths ever reported. Gates result in free-carrier absorption and below-gap absorption via the Franz-Keldysh effect – they are not obvi-

ously compatible with a high $\mathcal{Q}$-factor microcavity. We have found a way, passivation of the GaAs surface, to solve this problem: the microcavity has gates *and* an ultra-high $\mathcal{Q}$-factor, $\mathcal{Q} \simeq 10^6$. Details on the surface passivation procedure were presented in Chapter 4. With this, we have found evidence for the origin of the losses in the doped semiconductor DBR: the losses arise either from the semiconductor surface itself or the GaAs layer below the surface.

In Chapter 5, two fabrication methods to further decrease the microcavity mode volume were presented. Both protocols yield low-roughness, shallow, micrometer-sized concave mirror templates, thereby overcoming the present geometrical limits of conventional CO_2-laser ablation on polished fused silica substrates and on cleaved optical fibres. For the main method (top-down), we demonstrate high-finesse, stable microcavity operation at shallow depth and extract effective radii of curvature $\lesssim 5\,\mu\text{m}$ consistent with their geometrical shape. The top-down protocol relies on the conventional ablation process and thus conserves its excellent geometrical properties such as a high axial symmetry and ultra-low surface roughness. The prototype bottom-up protocol demonstrates the early steps towards shape control at the few-micrometer level, presently unachieved by conventional CO_2-laser ablation alone.

A reduction of the top mirror's curvature radius to $5\,\mu$m (at low crater depth and thus minimum vacuum-gap between the mirrors) will lead to a 2.3-fold reduction in mode-volume (Appendix C.4) which comes with a 1.5-fold increase of the coherent coupling strength. With this improvement, and taking into account the optimum parameters $(g, \kappa, \gamma)/2\pi \approx (4.4, 0.61, 0.28)\,\text{GHz}$ achieved in this work (Fig. 2.2h), cooperativities of $C \simeq 500$ are within reach.

The system opens the possibility of creating a photon-photon gate. A key advance here is the coherent exciton-photon interaction. This can be potentially exploited in the Duan-Kimble scheme [3]: reducing the intrinsic cavity loss by a factor of ten (which is feasible with a more advanced semiconductor design with narrower gates, for instance), the fidelity could be increased to $F_{\text{pp}} = 92\%$ by choosing $\kappa/(2\pi) = 3.8\,\text{GHz}$ (Appendix E.4). In this scheme, one arm of a Λ-transition is coupled to the cavity. This concept can be implemented with a QD spin. With respect to the present experiment, the missing ingredient is the capability of initialising the spin and performing spin rotations in the microcavity. We propose that this can be achieved by embedding the QD in a relatively large lateral waveguide, launching light into the waveguide either via edge-excitation or via etched gratings. With lateral excitation, the dark-field technique is no longer necessary. Also, the cavity can be designed with imbalanced reflectivities such that many more photons exit the top mirror than the bottom mirror. These two steps will

allow the system efficiency to be much increased over the present experiment.

The device is a potentially excellent single-photon source. On the one hand, the experiment establishes the value of electrical gates in the strong-coupling regime of cavity-QED. These advantages, in particular control of charge and close-to-transform-limited linewidths, are also important for a single-photon source operating in the weak-coupling regime of cavity-QED. Incorporating gates is relatively straightforward here but much more involved for micropillar and photonic-crystal cavity devices. On the other hand, the efficiency is potentially very high. For a fixed g and γ, the photon extraction efficiency via the cavity [31] can be maximised by designing the mirrors such that the condition $\kappa = 2g$ is satisfied. Taking the g from this experiment, this maximum efficiency corresponds to $\mathcal{Q} = 3.7 \cdot 10^4$. In practice, this can achieved with the present semiconductor mirror and a top mirror with reduced reflectivity. At this relatively low $\mathcal{Q}$, the residual absorption losses in the semiconductor are negligible and following exciton creation, the photon extraction efficiency via the top mirror should be as high as 94%*. This concept can also be profitably combined with lateral excitation, an "atom drive" [7, 101]. For instance, exploitation of the spin enables the efficient creation of shaped-waveform single photons.

The microcavity can be simplified: a monolithic design could exploit strain tuning of the QD rather than position-based tuning of the cavity. Also, the splitting of the cavity mode (into two modes with linear, orthogonal polarisations) can be eliminated by applying a bias across the semiconductor DBR [102]. Based on these considerations, a compact, on-chip, high-C single photon-single atom interface is within reach.

*For a maximum $g/2\pi = 4.4\,\mathrm{GHz}$ and minimum $\gamma/2\pi = 0.28\,\mathrm{GHz}$ in this work and choosing the top mirror reflectivity so that $\kappa = 2g$ is fulfilled (which corresponds to $C = 16$), we find $\eta = 94\%$ according to Eq. 1.8.

Appendix A

Measurements on cavity-coupled QD3

In this chapter, the main measurements on cavity-coupled QD3 are presented. A resonance-fluorescence scan is shown in Fig. A.1a. A line-cut reveals the maximum measured coupling rate of $g/2\pi = 4.4\,\mathrm{GHz}$ in this work. The FSS is only 5.75 GHz, such that the X_a^0-related polaritons overlap with a weakly coupled exciton transition (X_b^0). This prevents the application of the numerical model developed in Appendix D.

A strong beating with a period of $T = 654\,\mathrm{ps}$ (frequency 1.53 GHz) is clearly visible at photon blockade (Fig. A.1f), besides a minimum anti-bunching of $g^{(2)}(0) = 0.090 \pm 0.005$ measured in this work. We attribute this beat frequency to $\Delta_L + 1.31g = 1.53\,\mathrm{GHz}$ ($\Delta_L = -4.21\,\mathrm{GHz}$), the beating of the coherently scattered laser light at the X_a^0-related lower polariton with the emission from the weakly coupled transition X_b^0 at $-1.31g$ (black arrow in Fig. A.1d). We speculate that, for $\Delta_C = 0$, the additional resonance at $\Delta_L = -1.31g$ due to X_b^0 weak coupling leads to additional beatings around $1.31g \pm g$, $\Delta_L \pm 1.31g$ and $-\Delta_L - 1.31g$ (Fig. A.1d).

As in Chapter 3, the measured oscillation period in Fig. A.1e corresponds exactly to the vacuum Rabi frequency of $2g/2\pi = 8.8\,\mathrm{GHz}$. Fig. A.1e,f confirm once more the capability of this system: simply by sweeping the laser frequency by $\sim 1\,\mathrm{GHz}$, the $g^{(2)}(0)$-value changes by more than three orders of magnitude.

Note that in Fig. A.1a, the "right" cavity mode reveals the polaritons with much less clarity. A reason might be that a transverse mode is overlapping with this longitudinal mode. Around these wavelengths ($\lambda \sim 920\,\mathrm{nm}$) and this particular cavity length, overlap of a higher order transverse mode with one of the longitudinal cavity modes has been seen with different QDs.

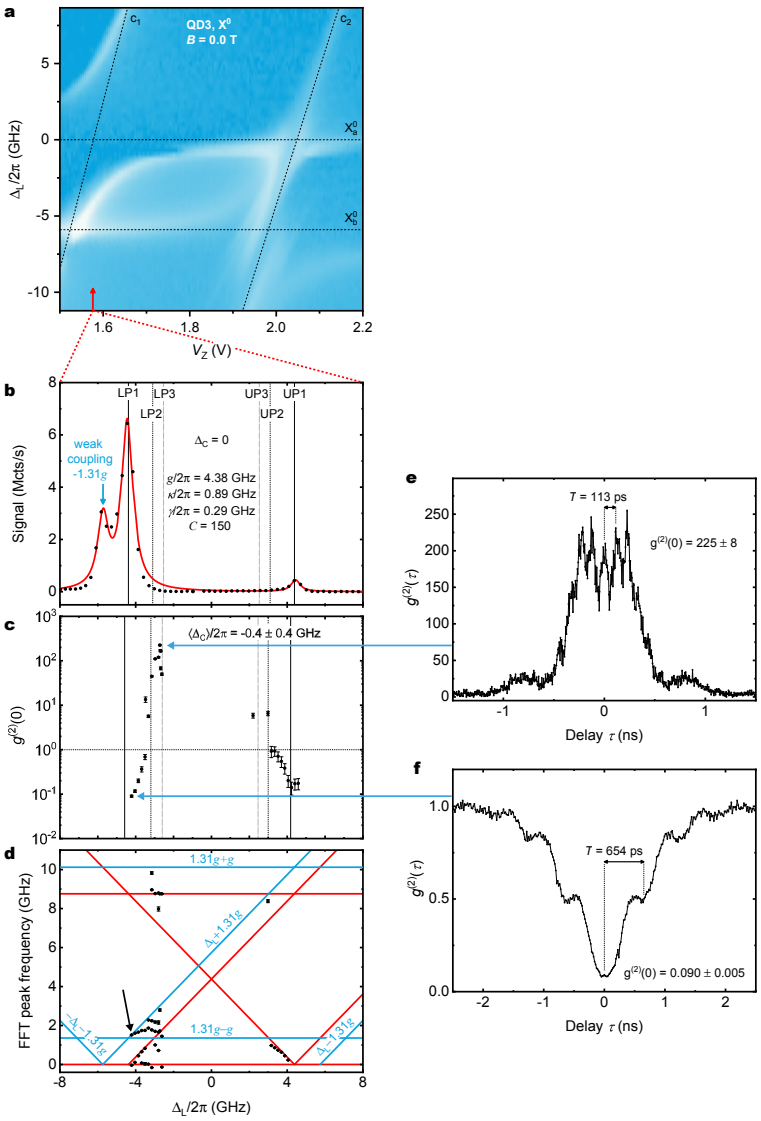

Fig. A.1. Spectroscopy on cavity-coupled QD3. **a**, X^0 at $B = 0.00$ T: RF scan revealing two TEM_{00} cavity modes c_1 and c_2 (inclined lines) coupled to two X^0 transitions with FSS of 5.75 GHz (horizontal lines). Logarithmic color scale (0.01–7 Mcts/s). **b**, Line cut at resonance to "left" cavity mode (as indicated by red arrow). The main peaks arise from strong coupling of X^0_a to one cavity mode revealing the maximum measured coupling rate of $g/2\pi = 4.4$ GHz in this work; the peak at $\Delta_L = -1.31g$ arises from weak coupling of X^0_b to the same cavity mode. Red solid line: triple-Lorentzian fit. **c**, $g^{(2)}(0)$ versus laser detuning for $\Delta_C \approx 0$. **d**, FFT peak frequency of $g^{(2)}(\tau)$ versus Δ_L for $\Delta_C \approx 0$. Additionally to the beat frequencies (red solid lines, $\Delta_C = 0$) between the two polaritons and the Rayleigh-scattered laser light, we speculate to observe other beat frequencies (blue solid lines, $\Delta_C = 0$) due to the overlap with the weakly coupled transition. This statement is supported by the observed beating in **f** with a period of $T = 654$ ps (frequency 1.53 GHz, black arrow in **d**), which corresponds exactly to $\Delta_L + 1.31g$ ($\Delta_L = -4.21$ GHz). **e** (**f**), $g^{(2)}(\tau)$ for $\Delta_C \approx 0$ and $\Delta_L \approx -g/\sqrt{2}$ ($\Delta_L \approx -g$) revealing the maximum (minimum) photon (anti-)bunching of $g^{(2)}(0) = 225 \pm 8$ ($g^{(2)}(0) = 0.090 \pm 0.005$) measured in this work. In **c**, **e** and **f**, the model developed in Appendix D is not applicable in this case due to the small FSS $< 2g$ and thus high overlap between the strongly (X^0_a) and weakly (X^0_b) coupled transitions.

Appendix B

1D transfer matrix calculation of the microcavity $\mathcal{Q}$-factors

In this chapter, the relevant parameters used for most of the $\mathcal{Q}$-factor calculations (via 1D transfer matrix methods, for instance the "Essential Macleod" package) presented in this work are listed. The following tables present the used materials, refractive indices n at $\lambda = 920\,\text{nm}$ and physical layer thicknesses d for three different microcavities investigated in this work: a dielectric top mirror ($\lambda_\text{C} = 973.0\,\text{nm}$, same as described in Section 3.3 and Fig. 4.7) paired with an nip-DBR ($\lambda_\text{C} = 919.0\,\text{nm}$, Tab. B.1), an undoped semiconductor DBR ($\lambda_\text{C} = 956.4\,\text{nm}$, Tab. B.2) and a dielectric DBR with an SB centre shifted by 3 nm ($\lambda_\text{C} = 976.1\,\text{nm}$, Tab. B.3).

Extinction coefficients in different materials are introduced as follows: $k_\text{SiO2} = 4 \cdot 10^{-7}$ for SiO_2 [70], $k_\text{Ta2O5} = 4.5 \cdot 10^{-7}$ for Ta_2O_5 [70], $k_\text{p++} = 5.2 \cdot 10^{-4}$ for p^{++}-GaAs, $k_\text{p+} = 1.9{\cdot}10^{-4}$ for p^{+}-GaAs and $k_\text{n+} = 0.7{\cdot}10^{-4}$ for n^{+}-GaAs [62]. $k = 4k_\text{Ta2O5}$ is used in the last grown Ta_2O_5 layer (close to vacuum-gap) of each dielectric DBR. An extinction coefficient of $k = \alpha_\text{FK}\lambda/(4\pi)$ due to a Franz-Keldysh absorption coefficient α_FK can be introduced in the capping layer. Surface roughness is introduced via "Scatter(l)"-layers of thickness $d = 2\sigma$, where σ is the rms surface/interface roughness [79].

In analogy to the experiment, a $\mathcal{Q}$-factor can be determined for a fixed "vacuum-gap" layer thickness* by calculating a cavity transmittance spectrum. A Lorentzian fit is used to determine the resonance frequency as well as the $\mathcal{Q}$-factor of the transmitted mode. The procedure is repeated for different vacuum-gaps, yielding a $\mathcal{Q}$-factor spectrum around the wavelengths of interest.

The resulting $\mathcal{Q}$-factors are presented in Chapter 4 (Fig. 4.3, Fig. 4.6 and Fig. 4.7).

*The minimum vacuum-gap is 1.2 μm due to the finite depth of the microcavity craters (Fig. C.1a).

Layer	Material	n	d (nm)	Layer	Material	n	d (nm)	Layer	Material	n	d (nm)
Medium	SiO2	1.45		61	GaAs	3.49	66.26	122	AlAs	2.92	79.65
1	Ta2O5	2.09	124.13	62	AlAs	2.92	80.76	123	GaAs	3.49	63.67
2	SiO2	1.46	175.47	63	GaAs	3.49	63.22	124	AlAs	2.92	79.17
3	Ta2O5	2.09	132.59	64	AlAs	2.92	79.16	125	GaAs	3.49	63.69
4	SiO2	1.46	178.68	65	GaAs	3.49	63.23	126	AlAs	2.92	79.21
5	Ta2O5	2.09	133.64	66	AlAs	2.92	79.17	127	GaAs	3.49	63.98
6	SiO2	1.46	184.76	67	GaAs	3.49	63.25	128	AlAs	2.92	80.76
7	Ta2O5	2.09	115.59	68	AlAs	2.92	79.17	129	GaAs	3.49	65.01
8	SiO2	1.46	172.34	69	GaAs	3.49	63.26	130	AlAs	2.92	80.76
9	Ta2O5	2.09	129.59	70	AlAs	2.92	80.06	131	GaAs	3.49	65.02
10	SiO2	1.46	164.08	71	GaAs	3.49	64.56	132	AlAs	2.92	80.76
11	Ta2O5	2.09	111.21	72	AlAs	2.92	80.76	133	GaAs	3.49	65.04
12	SiO2	1.46	154.75	73	GaAs	3.49	64.57	134	AlAs	2.92	80.76
13	Ta2O5	2.09	117.84	74	AlAs	2.92	80.76	135	GaAs	3.49	64.98
14	SiO2	1.46	168.51	75	GaAs	3.49	64.59	136	AlAs	2.92	79.82
15	Ta2O5	2.09	115.19	76	AlAs	2.92	79.84	137	GaAs	3.49	63.78
16	SiO2	1.46	174.29	77	GaAs	3.49	63.48	138	AlAs	2.92	79.17
17	Ta2O5	2.09	115.36	78	AlAs	2.92	79.17	139	GaAs	3.49	63.8
18	SiO2	1.46	170.25	79	GaAs	3.49	63.34	140	AlAs	2.92	79.17
19	Ta2O5	2.09	105.27	80	AlAs	2.92	79.17	141	GaAs	3.49	63.81
20	SiO2	1.46	170.29	81	GaAs	3.49	63.35	142	AlAs	2.92	79.17
21	Ta2O5	2.09	105.01	82	AlAs	2.92	79.18	143	GaAs	3.49	64.91
22	SiO2	1.46	166.26	83	GaAs	3.49	63.39	144	AlAs	2.92	80.76
23	Ta2O5	2.09	109.31	84	AlAs	2.92	79.2	145	GaAs	3.49	65.13
24	SiO2	1.46	169.05	85	GaAs	3.49	63.46	146	AlAs	2.92	80.76
25	Ta2O5	2.09	115.8	86	AlAs	2.92	79.79	147	GaAs	3.49	65.15
26	SiO2	1.46	162.8	87	GaAs	3.49	64.13	148	AlAs	2.92	80.76
27	Ta2O5	2.09	118.37	88	AlAs	2.92	80.16	149	GaAs	3.49	65.16
28	SiO2	1.46	177.77	89	GaAs	3.49	64.7	150	AlAs	2.92	80.25
29	Ta2O5	2.09	119.62	90	AlAs	2.92	80.18	151	GaAs	3.49	63.89
30	SiO2	1.46	159.75	91	GaAs	3.49	64.2	152	AlAs	2.92	79.17
31	Ta2O5	2.09	116.42	92	AlAs	2.92	79.98	153	GaAs	3.49	63.9
32	SiO2	1.46	175.72	93	GaAs	3.49	63.95	Substrate	GaAs	3.51	
33	Ta2O5	2.09	125.73	94	AlAs	2.92	79.77				
34	SiO2	1.46	182.1	95	GaAs	3.49	63.74				
35	Ta2O5	2.09	122.59	96	AlAs	2.92	79.43				
36	Scatter(I)		0.5	97	GaAs	3.49	63.97				
37	SiO2	1.46	168.45	98	AlAs	2.92	79.76				
38	Ta2O5	2.09	128.11	99	GaAs	3.49	64.18				
39	Scatter(I)		0.5	100	AlAs	2.92	79.99				
40	SiO2	1.46	184.38	101	GaAs	3.49	64.47				
41	Ta2O5	2.09	113.42	102	AlAs	2.92	80.52				
42	Scatter(I)		0.5	103	GaAs	3.49	64.81				
43	SiO2	1.46	175.89	104	AlAs	2.92	80.58				
44	Ta2O5	2.09	132.57	105	GaAs	3.49	64.82				
45	Scatter(I)		0.5	106	AlAs	2.92	80.75				
46	SiO2	1.46	171.29	107	GaAs	3.49	64.84				
47	Ta2O5	2.09	167.07	108	AlAs	2.92	80.76				
48	Scatter(I)		0.5	109	GaAs	3.49	64.15				
49	SiO2	1.46	170.41	110	AlAs	2.92	79.88				
50	Vacuum-gap	1.00	x	111	GaAs	3.49	63.75				
51	Al2O3	1.65	10	112	AlAs	2.92	79.54				
52	GaAs	3.49	55.82	113	GaAs	3.49	63.97				
53	GaAs (p++)	3.49	18.98	114	AlAs	2.92	80.05				
54	GaAs (p+)	3.49	4.75	115	GaAs	3.49	64.9				
55	GaAs	3.49	4.75	116	AlAs	2.92	80.76				
56	AlGaAs	3.32	183.32	117	GaAs	3.49	64.91				
57	GaAs	3.49	7.07	118	AlAs	2.92	80.76				
58	GaAs (QDs)	3.49	1.07	119	GaAs	3.49	64.93				
59	GaAs	3.49	28.91	120	AlAs	2.92	80.76				
60	GaAs (n+)	3.49	38.94	121	GaAs	3.49	64.95				
								Total:			15,500.50

Table B.1. Parameters used to simulate an nip-DBR microcavity. The tables show the used materials, refractive indices $n = n(920\,\mathrm{nm})$ and physical layer thicknesses d for a dielectric top mirror ($\lambda_\mathrm{C} = 973.0\,\mathrm{nm}$) paired with an nip-DBR ($\lambda_\mathrm{C} = 919.0\,\mathrm{nm}$).

Layer	Material	n	d (nm)	Layer	Material	n	d (nm)
Medium	SiO2	1.45		61	GaAs	3.53	68.33
1	Ta2O5	2.09	124.13	62	AlAs	3.01	80.8
2	SiO2	1.46	175.47	63	GaAs	3.53	68.33
3	Ta2O5	2.09	132.59	64	AlAs	3.01	80.8
4	SiO2	1.46	178.68	65	GaAs	3.53	68.31
5	Ta2O5	2.09	133.64	66	AlAs	3.01	80.74
6	SiO2	1.46	184.76	67	GaAs	3.53	68.23
7	Ta2O5	2.09	115.59	68	AlAs	3.01	80.79
8	SiO2	1.46	172.34	69	GaAs	3.53	68.33
9	Ta2O5	2.09	129.59	70	AlAs	3.01	80.8
10	SiO2	1.46	164.08	71	GaAs	3.53	68.33
11	Ta2O5	2.09	111.21	72	AlAs	3.01	80.8
12	SiO2	1.46	154.75	73	GaAs	3.53	68.33
13	Ta2O5	2.09	117.84	74	AlAs	3.01	80.8
14	SiO2	1.46	168.51	75	GaAs	3.53	68.33
15	Ta2O5	2.09	115.19	76	AlAs	3.01	80.8
16	SiO2	1.46	174.29	77	GaAs	3.53	68.33
17	Ta2O5	2.09	115.36	78	AlAs	3.01	80.8
18	SiO2	1.46	170.25	79	GaAs	3.53	68.33
19	Ta2O5	2.09	105.27	80	AlAs	3.01	80.8
20	SiO2	1.46	170.29	81	GaAs	3.53	68.33
21	Ta2O5	2.09	105.01	82	AlAs	3.01	80.8
22	SiO2	1.46	166.26	83	GaAs	3.53	68.33
23	Ta2O5	2.09	109.31	84	AlAs	3.01	80.8
24	SiO2	1.46	169.05	85	GaAs	3.53	68.26
25	Ta2O5	2.09	115.8	86	AlAs	3.01	80.5
26	SiO2	1.46	162.8	87	GaAs	3.53	66.97
27	Ta2O5	2.09	118.37	88	AlAs	3.01	79.2
28	SiO2	1.46	177.77	89	GaAs	3.53	66.97
29	Ta2O5	2.09	119.62	90	AlAs	3.01	79.2
30	SiO2	1.46	159.75	91	GaAs	3.53	66.97
31	Ta2O5	2.09	116.42	92	AlAs	3.01	79.2
32	SiO2	1.46	175.72	93	GaAs	3.53	68.25
33	Ta2O5	2.09	125.73	94	AlAs	3.01	79.78
34	SiO2	1.46	182.1	95	GaAs	3.53	68.32
35	Ta2O5	2.09	122.59	96	AlAs	3.01	79.22
36	Scatter(l)		0.5	97	GaAs	3.53	67
37	SiO2	1.46	168.45	98	AlAs	3.01	79.22
38	Ta2O5	2.09	128.11	99	GaAs	3.53	66.98
39	Scatter(l)		0.5	100	AlAs	3.01	79.21
40	SiO2	1.46	184.38	101	GaAs	3.53	66.98
41	Ta2O5	2.09	113.42	102	AlAs	3.01	80.8
42	Scatter(l)		0.5	103	GaAs	3.53	66.98
43	SiO2	1.46	175.89	104	AlAs	3.01	79.2
44	Ta2O5	2.09	132.57	105	GaAs	3.53	66.97
45	Scatter(l)		0.5	106	AlAs	3.01	79.2
46	SiO2	1.46	171.29	107	GaAs	3.53	66.97
47	Ta2O5	2.09	167.07	108	AlAs	3.01	79.2
48	Scatter(l)		0.5	109	GaAs	3.53	66.97
49	SiO2	1.46	170.41	110	AlAs	3.01	79.2
50	Vacuum-gap	1.00	x	111	GaAs	3.53	66.97
51	Scatter(l)		0	112	AlAs	3.01	79.2
52	GaAs	3.51	10	113	GaAs	3.53	66.97
53	GaAs	3.53	123.42	114	AlAs	3.01	79.2
54	GaAs (QDs)	3.53	1.07	115	GaAs	3.53	67.28
55	GaAs	3.53	133.42	116	AlAs	3.01	80.8
56	AlAs	3.01	79.2	117	GaAs	3.53	68.33
57	GaAs	3.53	66.98	118	AlAs	3.01	80.8
58	AlAs	3.01	80.8	119	GaAs	3.53	68.33
59	GaAs	3.53	68.33	120	AlAs	3.01	80.8
60	AlAs	3.01	80.8	Substrate	GaAs	3.51	
				Total:			13,631.54

Table B.2. Parameters used to simulate an undoped semiconductor microcavity. The tables show the used materials, refractive indices $n = n(920\,\mathrm{nm})$ and physical layer thicknesses d for a dielectric top mirror ($\lambda_\mathrm{C} = 973.0\,\mathrm{nm}$) paired with an undoped semiconductor DBR ($\lambda_\mathrm{C} = 956.4\,\mathrm{nm}$).

Layer	Material	n	d (nm)	Layer	Material	n	d (nm)
Medium	SiO2	1.45		61	Scatter(l)		0.5
1	Ta2O5	2.09	124.13	62	Ta2O5	2.09	128.51
2	SiO2	1.46	175.47	63	SiO2	1.46	168.98
3	Ta2O5	2.09	132.59	64	Scatter(l)		0.5
4	SiO2	1.46	178.68	65	Ta2O5	2.09	122.99
5	Ta2O5	2.09	133.64	66	SiO2	1.46	182.69
6	SiO2	1.46	184.76	67	Ta2O5	2.09	126.13
7	Ta2O5	2.09	115.59	68	SiO2	1.46	176.29
8	SiO2	1.46	172.34	69	Ta2O5	2.09	116.8
9	Ta2O5	2.09	129.59	70	SiO2	1.46	160.26
10	SiO2	1.46	164.08	71	Ta2O5	2.09	120
11	Ta2O5	2.09	111.21	72	SiO2	1.46	178.34
12	SiO2	1.46	154.75	73	Ta2O5	2.09	118.74
13	Ta2O5	2.09	117.84	74	SiO2	1.46	163.32
14	SiO2	1.46	168.51	75	Ta2O5	2.09	116.16
15	Ta2O5	2.09	115.19	76	SiO2	1.46	169.58
16	SiO2	1.46	174.29	77	Ta2O5	2.09	109.66
17	Ta2O5	2.09	115.36	78	SiO2	1.46	166.79
18	SiO2	1.46	170.25	79	Ta2O5	2.09	105.34
19	Ta2O5	2.09	105.27	80	SiO2	1.46	170.83
20	SiO2	1.46	170.29	81	Ta2O5	2.09	105.6
21	Ta2O5	2.09	105.01	82	SiO2	1.46	170.79
22	SiO2	1.46	166.26	83	Ta2O5	2.09	115.73
23	Ta2O5	2.09	109.31	84	SiO2	1.46	174.84
24	SiO2	1.46	169.05	85	Ta2O5	2.09	115.55
25	Ta2O5	2.09	115.8	86	SiO2	1.46	169.05
26	SiO2	1.46	162.8	87	Ta2O5	2.09	118.22
27	Ta2O5	2.09	118.37	88	SiO2	1.46	155.24
28	SiO2	1.46	177.77	89	Ta2O5	2.09	111.57
29	Ta2O5	2.09	119.62	90	SiO2	1.46	164.6
30	SiO2	1.46	159.75	91	Ta2O5	2.09	130
31	Ta2O5	2.09	116.42	92	SiO2	1.46	172.89
32	SiO2	1.46	175.72	93	Ta2O5	2.09	115.96
33	Ta2O5	2.09	125.73	94	SiO2	1.46	185.35
34	SiO2	1.46	182.1	95	Ta2O5	2.09	134.07
35	Ta2O5	2.09	122.59	96	SiO2	1.46	179.25
36	Scatter(l)		0.5	97	Ta2O5	2.09	133.02
37	SiO2	1.46	168.45	98	SiO2	1.46	176.02
38	Ta2O5	2.09	128.11	99	Ta2O5	2.09	124.53
39	Scatter(l)		0.5	Substrate	SiO2	1.45	
40	SiO2	1.46	184.38				
41	Ta2O5	2.09	113.42				
42	Scatter(l)		0.5				
43	SiO2	1.46	175.89				
44	Ta2O5	2.09	132.57				
45	Scatter(l)		0.5				
46	SiO2	1.46	171.29				
47	Ta2O5	2.09	167.07				
48	Scatter(l)		0.5				
49	SiO2	1.46	170.41				
50	Vacuum-gap	1.00	x				
51	SiO2	1.46	170.95				
52	Scatter(l)		0.5				
53	Ta2O5	2.09	167.6				
54	SiO2	1.46	171.83				
55	Scatter(l)		0.5				
56	Ta2O5	2.09	132.98				
57	SiO2	1.46	176.45				
58	Scatter(l)		0.5				
59	Ta2O5	2.09	113.78				
60	SiO2	1.46	184.97				
				Total:			14,615.60

Table B.3. Parameters used to simulate a purely dielectric microcavity. The tables show the used materials, refractive indices $n = n(920\,\mathrm{nm})$ and physical layer thicknesses d for a dielectric top mirror ($\lambda_C = 973.0\,\mathrm{nm}$) paired with a dielectric DBR with a SB centre shifted by 3 nm ($\lambda_C = 976.1\,\mathrm{nm}$).

Appendix C

FEM simulation of the microcavity (2D-axisymmetric)

Using a finite element method (FEM*), the complex eigenfrequency ω of an electromagnetic wave confined by the microcavity is calculated. The motivation is to compute cavity properties that depend most obviously on its geometry: the vacuum-electric field amplitude at the location of the quantum dots as well as the cavity's effective mode volume. Note that the calculated $\mathcal{Q}$-factors presented in this thesis are not computed via the FEM method, since 1D transfer matrix methods (Appendix B) have shown to be much less time-consuming and agree well with the measured $\mathcal{Q}$-factors.

C.1 Geometry and meshing

The geometry shown in Fig. 2.1a is based on the mirror profile (measured via scanning confocal microscopy) of the crater which was most often used for the strong-coupling experiments – the crater which revealed a $\mathcal{Q}$-factor up to $2.0 \cdot 10^6$ in the dielectric-dielectric case (Fig. 4.6a). A "modified ellipsoid" is fitted to the measured profile, similarly to Fig. 5.3, yielding a radius of curvature of $R = (10.46 \pm 0.14)\,\mu$m, $\epsilon = -4.841$ and $\delta = -2.587$. Together with the designed cavity layers refined according to Section 4.4, a geometry as depicted in Fig. C.1 is obtained. The symmetry axis corresponds to the optical axis of the cavity.

A perfectly matched layer (PML) around the simulation area accounts for an open boundary – it prevents electromagnetic waves reaching the end of the simulation area to be reflected [103]. A PML has typically a thickness d on the order of the wavelength of the computed electromagnetic wave. Here, $d = \lambda_C$ is chosen (λ_C being the stopband centre of the semiconductor DBR). The PML is truncated with an outer boundary,

*COMSOL Multiphysics, "Wave Optics Module", "Electromagnetic Waves, Frequency Domain interface"

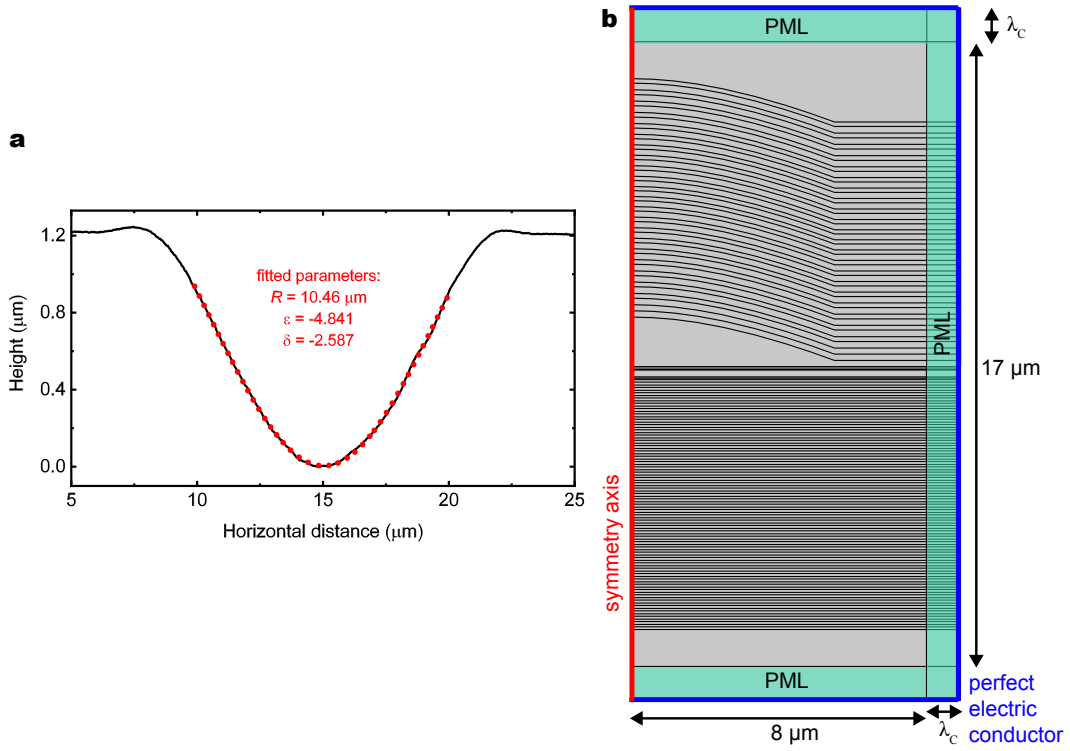

Fig. C.1. Geometrical model of the microcavity. a, Measured height profile of the coated mirror template used for the strong-coupling experiments revealing a radius of curvature $R = (10.46 \pm 0.14)\,\mu$m and crater depth $D = 1.24\,\mu$m. **b**, Geometry used for the 2D-axisymmetric FEM method (COMSOL Multiphysics). The simulation width is chosen to be in the order of a few beam waists of the near-Gaussian cavity mode. A perfectly matched layer (PML) is used to prevent back-reflections from the simulation boundaries (perfect electric conductor).

typically a conducting surface [104]. A 1 μm thick layer is used to simulate the bottom mirror and top mirror substrates.

The PML is meshed as a "mapped mesh" in order to prevent reflections in the PML due to numerical discretization and the rest of the geometry as a "free triangular mesh". The maximum (minimum) element size is defined as $\frac{\lambda_C}{m_1 n}$ ($\frac{\lambda_C}{m_2 n}$), where n is the refractive index of each layer and m_1, m_2 are integers to be chosen.

The $\mathcal{Q}$-factor of a computed cavity mode is derived as $\mathcal{Q} = \frac{\mathrm{Re}(\omega)}{2\,\mathrm{Im}(\omega)}$. It is found that the calculated $\mathcal{Q}$-factors of the cavity's longitudinal modes converge for a mesh parameter of $m > 12$. For the results presented in this work, a mesh parameter varying between $m_1 = 28$ and $m_2 = 35$ is used due to the fact that there are nanometer-sized layer thicknesses involved in the geometry.

C.2 Vacuum electric field amplitude

The vacuum electric field amplitude at the location of the quantum dot is derived by normalizing the total electromagnetic energy of the simulated mode by the vacuum energy of the electromagnetic field, $\hbar\omega/2$. The result is shown in Fig. 2.1a,b for an experimental vacuum-gap of 1885 nm. A value of $E_{\mathrm{vac}} = 3.0 \cdot 10^4\,\mathrm{V/m}$ at the quantum-dot location is calculated. Together with Eq. 1.3 and a typical dipole moment of an InAs quantum dot of $0.6\,\mathrm{nm}\times e$ [21] (e being the elementary charge), this yields $g/2\pi = 4.4\,\mathrm{GHz}$, exactly as measured with QD3 (Fig. 2.2h and Appendix A).

C.3 Effective mode volume

The microcavity's effective mode volume V is derived by dividing the total electromagnetic energy stored in the simulated mode by the electromagnetic energy density at the location of the quantum dot. With this method and cavity length according to the experiment (Fig. 2.1a), a mode volume of $V = 1.1\,\mu\mathrm{m}^3 = 1.4\lambda_0^3 \approx 59(\lambda/n)^3$ (λ_0 being the free-space wavelength) is obtained, a number which is consistent with Eq. 1.4 using the value for $g/2\pi = 4.4\,\mathrm{GHz}$ from above.

C.4 The case of reduced mode volume

With the results presented in Chapter 5, a simultaneous reduction of radius and depth of the curved mirror templates is realistic. Using the parameters $R = 5.22\,\mu\mathrm{m}$, $\epsilon = -1.989$, $\delta = -2.587$ and a vacuum-gap of 733 nm, a mode volume of $V = 0.49\,\mu\mathrm{m}^3 = 0.63\lambda_0^3 \approx 26(\lambda/n)^3$ and a coupling rate of $g/2\pi = 6.6\,\mathrm{GHz}$ is computed. Together with optimum parameters $(\kappa, \gamma)/2\pi \approx (0.61, 0.28)\,\mathrm{GHz}$ achieved in this work (Fig. 2.2h), this corresponds to a calculated cooperativity of $C = 510$.

Appendix D

Theory: laser driven atom-cavity system

Partially adapted from:
Daniel Najer, Immo Söllner, Pavel Sekatski, Vincent Dolique, Matthias C. Löbl, Daniel Riedel, Rüdiger Schott, Sebastian Starosielec, Sascha R. Valentin, Andreas D. Wieck, Nicolas Sangouard, Arne Ludwig, and Richard J. Warburton,
"A gated quantum dot far in the strong-coupling regime of cavity-QED at optical frequencies" (Supplementary Information),
arXiv:1812.08662 (2018).

D.1 Hamiltonians

Firstly, the free Hamiltonian of the atom-cavity system is stated. The quantum dot (QD) is modelled as a two-level system with energy levels $|\mathrm{g}\rangle$ and $|\mathrm{e}\rangle$ separated by an energy ω_0 (here and in the rest of the section, $\hbar = 1$ is used), i.e.

$$H_0 = \omega_\mathrm{e} |\mathrm{e}\rangle\langle\mathrm{e}| + \omega_\mathrm{g} |\mathrm{g}\rangle\langle\mathrm{g}| . \tag{D.1}$$

$\omega_\mathrm{e} = \omega_0$ and $\omega_\mathrm{g} = 0$ is used to simplify the notations. For the cavity, a single mode with associated creation and annihilation operators $a^\dagger$ and a is considered. If the frequency of the cavity field is resonant with the frequency separation of the two-level atom, the corresponding Hamiltonian reads

$$H_\mathrm{C} = \omega_0 a^\dagger a. \tag{D.2}$$

When the cavity frequency is detuned with respect to the atomic energy, ω_0 has to be replaced by ω_C. The interaction between the QD and the cavity mode is described by $g(|\mathrm{e}\rangle\langle\mathrm{g}| + |\mathrm{g}\rangle\langle\mathrm{e}|)(a^\dagger + a)$, where g is the coupling constant between the QD and the bare cavity mode. In the limit $g \ll \omega_0$, this coupling Hamiltonian is well approximated by

the Jaynes-Cummings Hamiltonian

$$H_{\text{int}} = g\Big(|\text{g}\rangle \langle \text{e}| \, a^\dagger + |\text{e}\rangle \langle \text{g}| \, a \Big). \tag{D.3}$$

The free Hamiltonian of the atom-cavity system is thus given by

$$H_{\text{free}} = H_0 + H_{\text{C}} + H_{\text{int}}. \tag{D.4}$$

D.2 Eigenstates and eigenvectors

To simplify the problem, it is convenient to choose a basis where the free Hamiltonian is diagonal. This basis can be easily found by noticing that H_{free} is block diagonal with blocks of size two spanned by $|\text{g}, n\rangle$ and $|\text{e}, n-1\rangle$, and a single block of size one spanned by $|\text{g}, 0\rangle$ with eigenvalue zero. $|n\rangle$ here denotes the Fock state for the light field with n excitations. Hence, using the basis $\{|\text{g}, n\rangle, |\text{e}, n-1\rangle\}$ for each block, the free Hamiltonian can be written as

$$H_{\text{free}} = \begin{pmatrix} 0 & & \\ & \bigoplus_{n=1}^{\infty} \begin{bmatrix} n\omega_0 & \sqrt{n}g \\ \sqrt{n}g & n\omega_0 \end{bmatrix} & \end{pmatrix}, \tag{D.5}$$

which can be easily diagonalised. The eigenstates of H_{free} are given by

$$|n\pm\rangle = \frac{|\text{g}, n\rangle \pm |\text{e}, n-1\rangle}{\sqrt{2}}, \tag{D.6}$$

with energies

$$E_n^{\pm} = n\omega_0 \pm \sqrt{n}g, \tag{D.7}$$

for $n \geq 1$ and $|0\rangle = |\text{g}, 0\rangle$ with $E_0 = 0$. As a result,

$$H_{\text{free}} = \sum_{n,\pm} E_n^{\pm} \, |n\pm\rangle\langle n\pm| \, . \tag{D.8}$$

One notes that in the case where the cavity mode frequency ω_{C} is not exactly equal to the atomic frequency ω_0 the free Hamiltonian reads

$$H_{\text{free}} = \begin{pmatrix} 0 & & \\ & \bigoplus_{n=1}^{\infty} \begin{bmatrix} n\omega_{\text{C}} & \sqrt{n}g \\ \sqrt{n}g & n\omega_{\text{C}} + (\omega_0 - \omega_{\text{C}}) \end{bmatrix} & \end{pmatrix}, \tag{D.9}$$

which affects both the spectrum and the eigenbasis, as is seen later.

D.3 Master equation

Consider the case where the atom-cavity system is driven by a laser through

$$H_{\mathrm{L}}(t) = \Omega(t)a + \Omega^{\star}(t)a^{\dagger}, \tag{D.10}$$

where $\Omega(t)$ is proportional to the complex light field amplitude incident on one of the cavity mirrors at time t. The cavity photons can leak out of the cavity via a beam-splitter type interaction. This leads to a decay channel entering in the master equation via a Lindblad operator $L_{\kappa} = \sqrt{\kappa}a$. Similarly, the spontaneous decay of the level $|\mathrm{e}\rangle$ to $|\mathrm{g}\rangle$ appears in the master equation via $L_{\gamma} = \sqrt{\gamma}\,|\mathrm{g}\rangle\langle\mathrm{e}|$. The evolution of this driven system is thus given by the following master equation

$$\dot{\rho} = -\mathrm{i}[H_{\mathrm{tot}}, \rho] + \sum_{L=L_{\kappa},L_{\gamma}} \left(L\rho L^{\dagger} - \frac{1}{2}L^{\dagger}L\rho - \frac{1}{2}\rho L^{\dagger}L \right) \tag{D.11}$$

with $H_{\mathrm{tot}} = H_{\mathrm{free}} + H_{\mathrm{L}}(t)$.

D.4 Numerical solutions

Analytical solutions of the master equation can be found by focusing on the relevant atom-cavity energy states and discarding the remaining states. The truncation of the Hilbert space in the analytical models is less severe in a fully numerical model. The Quantum Toolbox in Python (QuTiP)[105] is used and the Hilbert space is truncated in order to model the experimental results. Consider the case where the QD-cavity system is driven by a single monochromatic laser with frequency ω_L. Eq. (D.10) becomes

$$H_{\mathrm{L}}(t) = \Omega e^{\mathrm{i}\omega_{\mathrm{L}}t}a + \Omega e^{-\mathrm{i}\omega_{\mathrm{L}}t}a^{\dagger}. \tag{D.12}$$

As Ω is time independent, the explicit time dependence of the total Hamiltonian can be eliminated by considering the frame rotating at ω_L:

$$\begin{aligned} H_{\mathrm{rf}} =& \Omega\left(a + a^{\dagger}\right) + (\Delta_{\mathrm{C}} - \Delta_{\mathrm{L}})a^{\dagger}a - \Delta_{\mathrm{L}}\,|\mathrm{e}\rangle\langle\mathrm{e}| \\ &+ g\Big(\,|\mathrm{g}\rangle\langle\mathrm{e}|\,a^{\dagger} + |\mathrm{e}\rangle\langle\mathrm{g}|\,a\Big). \end{aligned} \tag{D.13}$$

The laser detuning relative to the emitter is denoted by $\Delta_{\mathrm{L}} = \omega_{\mathrm{L}} - \omega_0$, while the cavity detuning is denoted by $\Delta_{\mathrm{C}} = \omega_{\mathrm{C}} - \omega_0$. To simulate the experimental results the procedure outlined in Refs. [7, 106] is followed. First, the two collapse operators which determine the decay to the environment, i.e. out of the Jaynes-Cummings system, are defined. These are the two Lindblad operators L_κ and L_γ for the decay process out of the cavity mode and the decay of the QD into leaky modes, respectively. Next, exploiting the quantum regression theorem, one can solve for the normalized second order correlation function,

$$g^{(2)}(\tau) = \frac{\langle a^\dagger a^\dagger(\tau) a(\tau) a\rangle}{\langle a^\dagger a\rangle^2} = \frac{\mathrm{Tr}(a^\dagger a \mathrm{e}^{\mathcal{L}\tau}[a\rho_* a^\dagger])}{\left(\mathrm{Tr}(a^\dagger a \rho_*)\right)^2}, \tag{D.14}$$

where $\mathcal{L}$ is the Lindblad superoperator and ρ_* is the steady-state solution of the master equation.

For the experiments at low power (Figs. 2.1–2.3, 2.4b-g, 3.3a–c, 3.3e–j, 3.5a–b, 3.6) the Hilbert space is truncated at $n = 15$. However, the zeroth, first and second rungs (i.e. number of excitations $n = 0, 1, 2$) are sufficient to explain the results of Fig. 2.3 and Fig. 2.4b-g. The higher rungs result in changes to $g^{(2)}(\tau)$ which are smaller than the error bars of the experiment. However, on going to higher power, more rungs are necessary. In the power dependence (Fig. 2.4a and Fig. 3.3l), the simulations converge only for $n \geq 30$.

D.4.1 The role of laser background

In the experiments, even a small amount of mixing of the signal from the QD-cavity system with a laser background can play an important role. This can be included in the model via a simple beam-splitter. The creation and annihilation operators for the input and output modes are denoted a/b and c/d, respectively. The transmission and reflection coefficients are given by $t = t' = \sqrt{\eta}$ and $r = r' = i\sqrt{1-\eta}$.

$$\begin{pmatrix} \hat{c}^\dagger \\ \hat{d}^\dagger \end{pmatrix} = \hat{U}_{\mathrm{bs}} \begin{pmatrix} \hat{a}^\dagger \\ \hat{b}^\dagger \end{pmatrix}, \tag{D.15}$$

where

$$\hat{U}_{\mathrm{bs}} = \begin{pmatrix} t' & r \\ r' & t \end{pmatrix} = \begin{pmatrix} \sqrt{\eta} & i\sqrt{1-\eta} \\ i\sqrt{1-\eta} & \sqrt{\eta} \end{pmatrix}. \tag{D.16}$$

The creation and annihilation operators of output mode c are given by

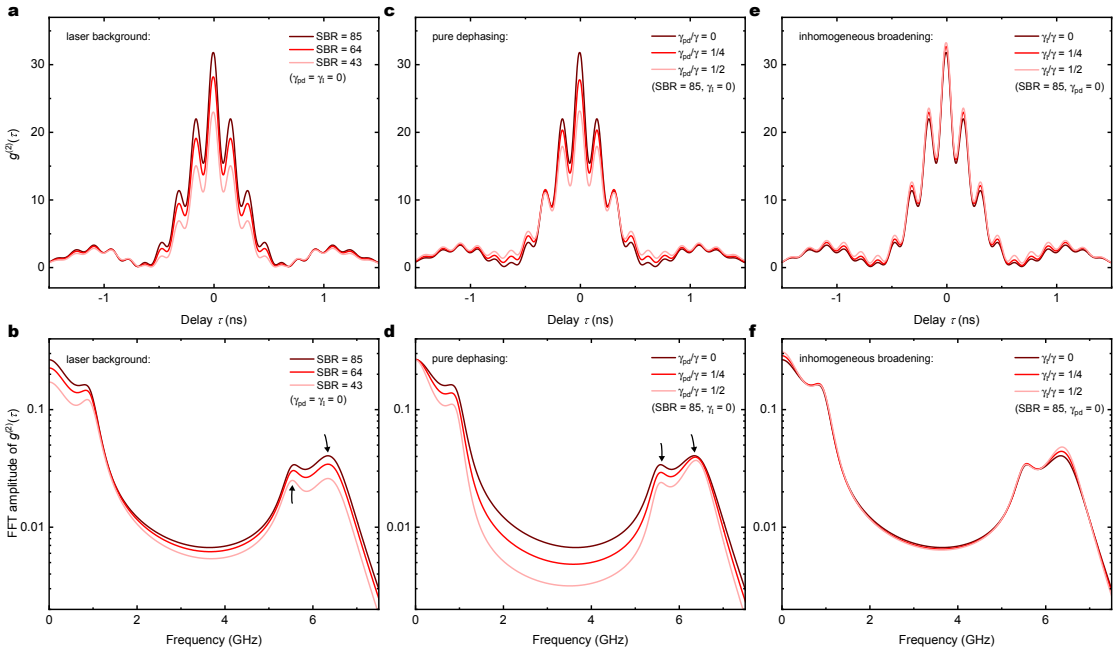

Fig. D.1. Effects of laser background, pure dephasing and inhomogeneous broadening of the exciton on $g^{(2)}(\tau)$ and its FFT. All dark red solid lines correspond to the model in Fig. 4b ($\Delta_{\rm L} = -g/\sqrt{2}, \Delta_{\rm C} = 0$) of the main paper which ignores pure dephasing and inhomogeneous broadening of the exciton. **a,b**, Same model but with different signal-to-background ratios (SBRs). The laser background mainly reduces the amplitude of the vacuum Rabi-oscillations but, in addition, increases the visibility of the beatings with the coherent laser field in $g^{(2)}(\tau)$ (black arrows). **c,d**, Same model including different pure dephasing rates $\gamma_{\rm pd}$ while fixing the spectroscopy-linewidth, $\gamma = \gamma_R + 2\gamma_{\rm pd}$ and laser background (γ_R is the radiative decay rate). Pure dephasing washes out all the oscillations in $g^{(2)}(\tau)$ in a similar way. **e,f**, Same model with $\gamma_{\rm pd} = 0$ including different values of inhomogeneous broadening, $\gamma_{\rm I}$: $\gamma = \gamma_{\rm R} + \gamma_{\rm I}$. Inhomogeneous broadening generally affects the $g^{(2)}(\tau)$ less than laser background and pure dephasing.

$$\hat{c}^\dagger = \sqrt{\eta}\ \hat{a}^\dagger + i\sqrt{1-\eta}\ \hat{b}^\dagger, \tag{D.17}$$

$$\hat{c} = \sqrt{\eta}\ \hat{a} - i\sqrt{1-\eta}\ \hat{b}, \tag{D.18}$$

and similarly for the output mode d. Input mode b, which is introduced to model the laser background, is in a coherent state with an average photon number, $|\alpha|^2$.

Experimentally, it is straightforward to determine what percentage of the observed count rate is due to the laser background. By choosing $|\alpha|^2$ to be the photon number expectation value when the system is driven on resonance ($\Delta_{\rm L} = g$), the mixing parame-

ter $1-\eta$ determines what percentage of counts comes from the laser background and its inverse value corresponds to the signal-to-background ratio (SBR). It should be noted that this is a good way of including the background in the low excitation regime where the relationship between incident power and count rate is constant such that η remains constant.

In order to model background counts (which are proportional to the incoming laser power) for the entire power range (e.g. for calculations in Figs. 2.4a, 3.3l and 3.5c–e), a fixed $\eta = 0.999$ and a second beam-splitter before input mode b with transmission $t_2 = t_2' = \sqrt{\eta_2}$ is used. $\alpha_2 = \sqrt{1000 P \eta_2}$ is chosen, where P is the monitored laser power in the excitation arm of the microscope.

Laser background affects $g^{(2)}(\tau)$ (and its FFT) mainly in two ways. First, it reduces the photon bunching around $g^{(2)}(0)$ (Fig. 2.4e and Fig. D.1a). Secondly, it washes out all vacuum Rabi-oscillations (6.5 GHz in Fig. D.1b) but, relative to that, increases the "laser" beatings arising from the mixing of polariton photons with Rayleigh-scattered laser photons (5.6 GHz and 0.8 GHz in Fig. D.1b).

D.4.2 The role of pure dephasing

The excited atom may undergo a dephasing process in addition to its decay. We consider this possibility. We introduce pure dephasing of the exciton [30, 107] at rate γ_{pd} via an additional Lindblad operator $L_{\gamma_{\mathrm{pd}}} = \sqrt{\gamma_{\mathrm{pd}}}\,|\mathrm{e}\rangle\langle\mathrm{e}|$ in the master equation (D.11). We find that the oscillations in $g^{(2)}(\tau)$ are sensitive to this process. Pure dephasing of the exciton washes out all vacuum Rabi-oscillations in $g^{(2)}(\tau)$ (the peak at 6.5 GHz in the Fourier transform of Fig. D.1d). Likewise, pure dephasing of the exciton decreases the amplitude of the beatings with the coherent laser field (features at 5.6 GHz and 0.8 GHz in Fig. D.1d).

The laser background also washes out the vacuum Rabi-oscillations (Fig. D.1a). However, the laser background increases the visibility of the beatings with the coherent laser field. This difference between pure dephasing of the exciton and the laser background allows the two mechanisms to be distinguished from each other. Including γ_{pd} as another fitting parameter to the experimental data in Fig. 2.3 and Fig. 2.4b of the main paper yields $\gamma_{\mathrm{pd}} = (0.034 \pm 0.002)\,\mathrm{GHz}$ and $\gamma_{\mathrm{pd}} = (0.022 \pm 0.003)\,\mathrm{GHz}$, respectively, where the errors refer to the random errors generated by the fit. Including pure dephasing of the exciton to the model improves slightly the fidelity of the fit. The fitted γ_{pd}-values are less than the radiative decay rate and much less than the cavity decay rate. The conclusion is that pure dephasing of the exciton makes at most a small contribution to

the overall dephasing rate of the system.

D.4.3 The role of inhomogeneous broadening and the transform limit

According to previous experiments [65], the radiative decay time of X^0 in the wavelength range of the QDs presented in the paper (919–933 nm) is on average 530 ps with QD-to-QD fluctuations [65] of ±80 ps. This corresponds to a transform-limited optical-linewidth of (300 ± 50) MHz. The measured X^0 linewidths of 280–290 MHz lie exactly within this range. This demonstrates that the linewidths are close to the transform-limit.

Exciton linewidths are determined by rather slow spectroscopy experiments: they are susceptible to an inhomogeneous broadening, here a spectral fluctuation of the emitter frequency on timescales large with respect to radiative decay but small with respect to experimental integration times. The oscillations in $g^{(2)}(\tau)$ (Fig. 2.3) are sensitive to exciton dephasing ("pure dephasing" of the emitter, Fig. D.1c,d). We find that these oscillations are very weakly influenced by an inhomogeneous broadening (Fig. D.1e,f). (To account for an inhomogeneous broadening, the calculated $g^{(2)}(\tau, \delta_{\mathrm{QD}})$ is convoluted with a (Lorentzian) probability distribution $P(\delta_{\mathrm{QD}}, \gamma_{\mathrm{I}})$. δ_{QD} is the QD detuning with respect to its time-averaged value.) On the one hand, this result strengthens the result on γ_{pd} from Appendix D.4.2. On the other hand, this result makes it difficult to determine γ_{I}, the contribution to γ from an inhomogeneous broadening. Likewise, the photon blockade experiment (Fig. 2.4c) is also insensitive to an inhomogeneous broadening.

Appendix E

Theory: photon-photon gate fidelity

A photon-photon gate as proposed by Duan and Kimble [3] is considered here. The basic idea is to use single-photon polarisations as photonic qubits for quantum computation [1, 2]. Using photonic qubits offers the advantage of scalability – the number of qubits can easily be scaled up by the generation of many single-photon pulses [3].

Photons do not interact with each other. This is where the strongly coupled atom-cavity system* comes into play: it acts as mediator between two photonic qubits by providing controlled gate operations between them [3]. A measure for how well these gate operations can be performed is the (gate) fidelity.

One crucial component for these operations is an atom-photon gate that performs a quantum controlled phase-flip (CPF) on a combined atom-photon state [109]: depending on the state of the atom and input photon, the phase of the combined atom-photon state is flipped or not. This depends on the cooperativity as the reflection off a strongly coupled atom-cavity system depends on the cooperativity [4], as is seen in the following. The aim of this chapter is to clarify the dependence of the gate fidelity on the cooperativity for an atom-photon gate and ultimately, a photon-photon gate.

E.1 Duan-Kimble scheme for an atom-photon gate

The scheme of Duan and Kimble [3] for an atom-photon gate (and ultimately, a photon-photon gate) is depicted in Fig. E.1 for the case of pure input states (for clarity). A single photon represents the input. A beam-splitter transmits a horizontally-polarised photon in (pure) state $|H\rangle$ while a photon with a vertical polarisation $|V\rangle$ is reflected undergoing a phase-shift of π. The transmitted part interacts with a resonant cavity.

*Note that strong coupling is a sufficient but not necessary condition to realise an atom-photon or photon-photon gate. A high cooperativity is the important ingredient – no matter if the atom-cavity system is strongly or weakly coupled [39, 108]. However, with the current microcavity parameters (g, κ, γ) presented in this work, a high cooperativity is only possible with strong coupling.

The two mirrors in the cavity have imbalanced reflectivities R, so that the decay rate through the left mirror (corresponding to the"top" mirror in our experiment) is given by κ. A three-level atom is placed inside the cavity, the cavity field being resonant with the $|1\rangle \leftrightarrow |\mathrm{e}\rangle$ transition. The line of the excited state is considered to have a Lorentzian lineshape $\frac{\gamma}{2\pi}\frac{1}{\omega^2+(\gamma/2)^2}$ given by a full-width-at-half-maximum of γ.

First, consider the case where the atom is initially in the (pure) state $|0\rangle$ (Fig. E.1a). The cavity field does not see the atom and since a photon in state $|H\rangle$ is resonant with the bare cavity, it will have a longer path than a photon $|V\rangle$ (while undergoing a phase-shift of 2π). Due to the difference of π in acquired phase by the two photons $|H\rangle$ and $|V\rangle$ upon reflection, this translates into the following phase term

$$\boxed{\begin{aligned} |0\rangle|V\rangle &\rightarrow \quad |0\rangle|V\rangle, && \text{(E.1a)}\\ |0\rangle|H\rangle &\rightarrow e^{i\pi}|0\rangle|H\rangle. && \text{(E.1b)}\end{aligned}}$$

Now consider the case where the atom is initially in (pure) state $|1\rangle$ (Fig. E.1b). Since the atom-field are potentially strongly coupled, the relevant energies are the atomic energies dressed by the cavity field. The first two energies are given by the cavity frequency shifted by the atom–single-photon coupling rate $\pm g$. Hence, a photon in (pure) state $|H\rangle$ at the cavity frequency is prevented from entering the cavity by strong coupling – it is directly reflected with probability amplitude (see for example Ref. [4])

$$\frac{2C-1}{2C+1}, \tag{E.2}$$

where C is the cooperativity. For large enough cooperativity, the light is completely reflected such that

$$\boxed{\begin{aligned} |1\rangle|V\rangle &\rightarrow |1\rangle|V\rangle, && \text{(E.3a)}\\ |1\rangle|H\rangle &\rightarrow |1\rangle|H\rangle. && \text{(E.3b)}\end{aligned}}$$

Taking the two polarization modes and the two atomic ground states as qubit states, it is clear that this protocol operates as a CPF atom-photon gate between the atom and the single-photon pulse: the phase of the mutual atom-photon state is flipped depending on the mutual atom-photon state. Note that in the case where the horizontal light is not reflected, which-path information is made available e.g. by absorption followed by spontaneous emission.

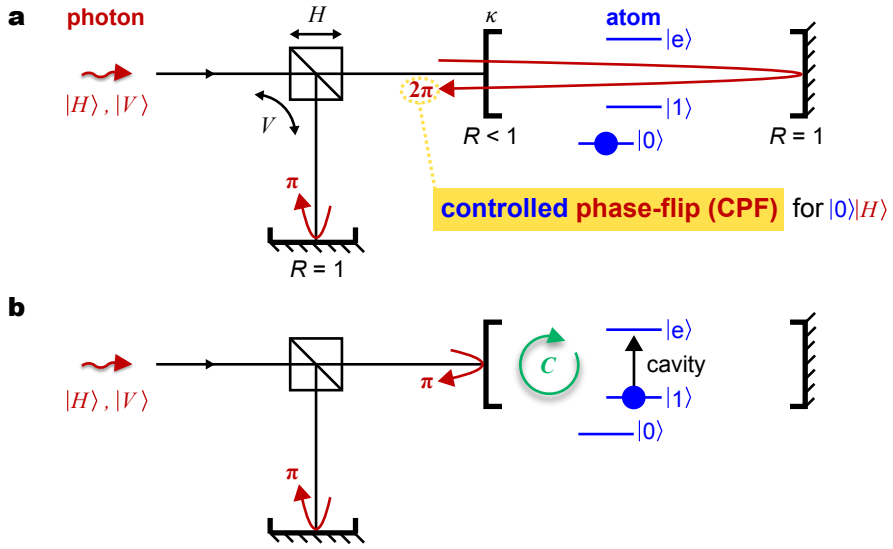

Fig. E.1. Setup for implementing an atom-photon gate (controlled phase-flip) from a strongly coupled atom-cavity system [3]. A single photon is sent into a polarising beam-splitter (PBS). The PBS reflects vertically polarised photons $|V\rangle$ while transmitting horizontally polarised ones, $|H\rangle$. **a**, For an atom in pure state $|0\rangle$, a photon in pure state $|H\rangle$ resonant with the cavity will undergo several round-trips in the cavity picking up a phase of 2π. **b**, For an atom in pure state $|1\rangle$, the same photon is directly reflected from the atom-cavity system (with a probability related to the cooperativity C only) ungergoing a phase-shift of π, similarly to a V-polarised reflected from the single mirror (independent on the state of the atom). The composition of those sub-processes **a** and **b** results in a quantum controlled phase-flip (CPF) gate between the atom an the photon: the phase of the mutual atom-photon state is flipped if and only if the atom-photon is in the state $|0\rangle\,|H\rangle$.

E.2 Atom-photon gate fidelity

To quantify the imperfection on the fidelity (the Uhlmann-Jozsa fidelity*) as a function of C, the two Kraus operators in the basis $\{|0,H\rangle, |0,V\rangle, |1,H\rangle, |1,V\rangle, |1,x\rangle\}$ are considered, where x stands for a spontaneously emitted photon:

$$K_0 = \begin{pmatrix} e^{i\pi} & 0 & 0 & 0 & 0 \\ 0 & 1 & 0 & 0 & 0 \\ 0 & 0 & \frac{2C-1}{2C+1} & 0 & 0 \\ 0 & 0 & 0 & 1 & 0 \\ 0 & 0 & 0 & 0 & 1 \end{pmatrix} \tag{E.4}$$

*The Uhlmann-Jozsa fidelity between two generic quantum states ρ and σ is defined as $F(\rho,\sigma) = \left(\mathrm{Tr}\sqrt{\sqrt{\rho}\sigma\sqrt{\rho}}\right)^2$ [110].

and

$$K_1 = \begin{pmatrix} 0 & 0 & 0 & 0 & 0 \\ 0 & 0 & 0 & 0 & 0 \\ 0 & 0 & 0 & 0 & 0 \\ 0 & 0 & 0 & 0 & 0 \\ 0 & 0 & \sqrt{1-\frac{(2C-1)^2}{(2C+1)^2}} & 0 & 0 \end{pmatrix}. \tag{E.5}$$

For any input state ρ, the previously described operation gives

$$\bar{\rho} = K_0 \rho K_0^\dagger + K_1 \rho K_1^\dagger. \tag{E.6}$$

The fidelity for the Bell states $\{\psi^-, \psi^+, \phi^-, \phi^+\}$ acting as input states is

$$F_{\psi^-} = F_{\psi^+} = \frac{1}{4}\left(1 + \frac{2C-1}{2C+1}\right)^2 = \left(\frac{2C}{1+2C}\right)^2, \tag{E.7}$$

$$F_{\phi^-} = F_{\phi^+} = 1, \tag{E.8}$$

which yields a mean fidelity

$$\overline{F}_{\text{ap}}(C) = \frac{1}{4}(F_{\psi^-} + F_{\psi^+} + F_{\phi^-} + F_{\phi^+}) \tag{E.9}$$

$$= \frac{1}{2}\left[1 + \left(\frac{2C}{1+2C}\right)^2\right] \tag{E.10}$$

$$\approx 1 - \frac{1}{2C}. \tag{E.11}$$

Note that the mean fidelity gives the same result to first order in $1/C$ as the Choi fidelity [111]. For $C = 5$, $F_{\text{ap}} \approx 90\%$ while for $C = 150$, $F_{\text{ap}} \approx 99.7\%$. Note that these results come from the first-order expansion in $1/C$ which is not very accurate for small C.

E.3 Extension to photon-photon gate

A photon-photon (CPF) gate between two single-photon pulses j and k can described by the unitary operator $U_{jk}^{\text{CPF}} = e^{i\pi|H\rangle_j\langle H|\otimes|H\rangle_k\langle H|}$ that flips the phase of the input state (a mutual state of j and k) if and only if both photonic qubits are H-polarised. Duan and Kimble showed that this can be realised by applying an atom-photon gate on both of photonic qubits while performing some single-bit rotations ($R_a(\theta)^*$) on the atom [3]:

*$R_a(\theta)$ corresponds to a single-bit rotation on the atom transforming as $R_a(\theta)\,|0\rangle = \cos\theta/2\,|0\rangle + \sin\theta/2\,|1\rangle$ and $R_a(\theta)\,|1\rangle = -\sin\theta/2\,|0\rangle + \cos\theta/2\,|1\rangle$.

First, a pulse j is reflected from the cavity (atom-photon gate $U_{aj}^{\mathrm{CPF}} = e^{i\pi|0\rangle_a\langle 0|\otimes|H\rangle_j\langle H|}$). Secondly, a $\pi/2$ laser pulse is applied on the atom, $R_a(\pi/2)$. Thirdly, a pulse k is reflected from the cavity (atom-photon gate U_{ak}^{CPF}). Fourthly, a $-\pi/2$ laser pulse is applied on the atom, $R_a(-\pi/2)$. And finally, the pulse j is again reflected from the cavity (atom-photon gate U_{aj}^{CPF}) in order to restore the initial state of the atom, i.e. to disentangle the state of the atom from the state of the two photons [108]. All in all, this corresponds to the operator identity [3]

$$U_{jk}^{\mathrm{CPF}}\,|\psi_{jk}\rangle\otimes|\Phi_{ai}\rangle = U_{aj}^{\mathrm{CPF}} R_a\left(-\tfrac{\pi}{2}\right) U_{ak}^{\mathrm{CPF}} R_a\left(\tfrac{\pi}{2}\right) U_{aj}^{\mathrm{CPF}}|\psi_{jk}\rangle\otimes|\Phi_{ai}\rangle\,, \tag{E.12}$$

where ψ_{jk} corresponds to the state of the photonic qubits (j and k) and $|\Phi_{ai}\rangle = \frac{|0\rangle+|1\rangle}{\sqrt{2}}$ is the initial state of the atom, i.e. an equal superposition of the atom's two ground states.

Assuming that the atomic rotations are carried out perfectly but the cooperativity is the limiting factor for the CPF gate, the Choi fidelity [111] of such a photon-photon process is

$$F_{\mathrm{pp}}(C) = \frac{\left[4C^2+1\right]\left[4C\Big(2C+1\Big)\Big(8C(C+1)+1\Big)+1\right]}{4\,(2C+1)^6} \tag{E.13}$$

$$\approx 1-\frac{3}{2C}. \tag{E.14}$$

For $C=5$, $F_{\mathrm{pp}}\approx 70\%$ while for $C=150$, $F_{\mathrm{pp}}\approx 99\%$.

E.4 Intrinsic cavity loss

So far we assumed that whenever a photon leaks from the cavity, it is emitted in the right mode through the left mirror, i.e. $\kappa = \kappa_{\mathrm{top}}$. In practice, the cavity also has some intrinsic loss characterized by the decay rate κ_i. Hence, the total cavity decay rate has two contributions

$$\kappa = \kappa_{\mathrm{top}} + \kappa_i. \tag{E.15}$$

In our setup, κ_{top} is related to the reflectivity of the top mirror, and the intrinsic loss rate κ_i is dominated by the loss through the bottom mirror. We introduce

$$\eta_{\mathrm{out}} = \frac{\kappa_{\mathrm{top}}}{\kappa_{\mathrm{top}}+\kappa_i} \tag{E.16}$$

which characterises the probability of photon collection from the cavity. Note that η_{out} can be adjusted in our setup by varying the reflectivity of the top mirror.

A non-unity $\eta_{\mathrm{out}} < 1$ does not affect the action of the atom-photon gate on a vertically

polarised photon since the latter does not interact with the cavity. However, it does play an important role for a horizontally polarised photon. As shown in Ref. [112], the reflection coefficients become

$$|0\rangle|H\rangle \rightarrow (2\eta_{\text{out}} - 1)e^{i\pi}|0\rangle|H\rangle, \tag{E.17}$$

$$|1\rangle|H\rangle \rightarrow \left(1 - \frac{2\eta_{\text{out}}}{1+2C}\right)|1\rangle|H\rangle \tag{E.18}$$

when taking η_{out} into account. This translates into Kraus operators of the form

$$K_0 = \begin{pmatrix} (2\eta_{\text{out}} - 1)e^{i\pi} & 0 & 0 & 0 & 0 \\ 0 & 1 & 0 & 0 & 0 \\ 0 & 0 & \left(1 - \frac{2\eta_{\text{out}}}{1+2C}\right) & 0 & 0 \\ 0 & 0 & 0 & 1 & 0 \\ 0 & 0 & 0 & 0 & 1 \end{pmatrix} \tag{E.19}$$

and

$$K_1 = \begin{pmatrix} 0 & 0 & 0 & 0 & 0 \\ 0 & 0 & 0 & 0 & 0 \\ 0 & 0 & 0 & 0 & 0 \\ 0 & 0 & 0 & 0 & 0 \\ \sqrt{1 - (2\eta_{\text{out}} - 1)^2} & 0 & \sqrt{1 - \left(1 - \frac{2\eta_{\text{out}}}{1+2C}\right)^2} & 0 & 0 \end{pmatrix}. \tag{E.20}$$

The resulting Choi fidelity of the atom-photon gate becomes

$$\boxed{F_{\text{ap}}(\eta_{\text{out}}, C) = \frac{1}{4}\left(1 + \eta_{\text{out}} - \frac{\eta_{\text{out}}}{1+2C}\right)^2,} \tag{E.21}$$

while for the photon-photon gate (Eq. E.12), the Choi fidelity reads

$$\boxed{\begin{aligned} F_{\text{pp}}(\eta_{\text{out}}, C) =& \frac{\left(4\eta_{\text{out}}^3\left(1 - 2C^2\right) + 4\eta_{\text{out}}^2(C^2 - 1)(2C + 1) + (2C + 1)^3\right)^2}{8(2C + 1)^6} \\ &+ \frac{1}{8}\left[\frac{4\eta_{\text{out}}^2\left(\eta_{\text{out}} + 2\eta_{\text{out}}C(C + 1) - (C + 1)^2\right)}{(2C + 1)^2} + 1\right]^2. \end{aligned}} \tag{E.22}$$

$F_{\text{ap}}(\eta_{\text{out}}, C)$ and $F_{\text{pp}}(\eta_{\text{out}}, C)$ are the same as $F_{\text{ap}}(C)$ and $F_{\text{pp}}(C)$ in the limit $\eta_{\text{out}} \rightarrow 1$. The dependence of $F_{\text{ap}}(\eta_{\text{out}}, C)$ and $F_{\text{pp}}(\eta_{\text{out}}, C)$ on η_{out} and C establishes two criteria

to be fulfilled experimentally: $C \gg 1$ and $\eta_{\text{out}} \simeq 1$.

With the parameters achieved on QD3, reducing the top-mirror reflectivity so that $\kappa/(2\pi) = 12.3\,\text{GHz}$, and inputting the losses in the present hetereostructure, $\kappa_i/(2\pi) = 0.55\,\text{GHz}$, the atom-photon and photon-photon fidelities are $F_{\text{ap}}(\eta_{\text{out}}, C) = 92\%$ and $F_{\text{pp}}(\eta_{\text{out}}, C) = 77\%$, respectively ($\eta_{\text{out}} = 96\%$, $C = 11$).

Reducing the intrinsic cavity loss by a factor of ten (which is feasible with a more advanced semiconductor design with narrower gates, for instance), the fidelities could be increased. By choosing $\kappa/(2\pi) = 3.8\,\text{GHz}$, $F_{\text{ap}}(\eta_{\text{out}}, C) = 97\%$ and $F_{\text{pp}}(\eta_{\text{out}}, C) = 92\%$ ($\eta_{\text{out}} = 99\%$, $C = 35$).

References

[1] Q. A. Turchette, C. J. Hood, W. Lange, H. Mabuchi, and H. J. Kimble, *Measurement of conditional phase shifts for quantum logic*, Phys. Rev. Lett. **75**, 4710 (1995).

[2] I. L. Chuang and Y. Yamamoto, *Simple quantum computer*, Phys. Rev. A **52**, 3489 (1995).

[3] L.-M. Duan and H. J. Kimble, *Scalable photonic quantum computation through cavity-assisted interactions*, Phys. Rev. Lett. **92**, 127902 (2004).

[4] M. Afzelius, N. Sangouard, G. Johansson, M. U. Staudt, and C. M. Wilson, *Proposal for a coherent quantum memory for propagating microwave photons*, New Journal of Physics **15**, 065008 (2013).

[5] A. Boca, R. Miller, K. M. Birnbaum, A. D. Boozer, J. McKeever, and H. J. Kimble, *Observation of the vacuum Rabi spectrum for one trapped atom*, Phys. Rev. Lett. **93**, 233603 (2004).

[6] K. Birnbaum, A. Boca, R. Miller, A. Boozer, T. Northup, and H. Kimble, *Photon blockade in an optical cavity with one trapped atom*, Nature **436**, 87 (2005).

[7] C. Hamsen, K. N. Tolazzi, T. Wilk, and G. Rempe, *Two-photon blockade in an atom-driven cavity QED system*, Phys. Rev. Lett. **118**, 133604 (2017).

[8] A. Kawasaki, B. Braverman, E. Pedrozo-Peñafiel, C. Shu, S. Colombo, Z. Li, O. Özel, W. Chen, L. Salvi, A. Heinz, D. Levonian, D. Akamatsu, Y. Xiao, and V. Vuletić, *Geometrically asymmetric optical cavity for strong atom-photon coupling*, Phys. Rev. A **99**, 013437 (2019).

[9] J. Reithmaier, G. Sek, A. Löffler, C. Hofmann, S. Kuhn, S. Reitzenstein, L. Keldysh, V. Kulakovskii, T. Reinecke, and A. Forchel, *Strong coupling in a single quantum dot-semiconductor microcavity system*, Nature **432**, 197 (2004).

[10] T. Yoshie, A. Scherer, J. Hendrickson, G. Khitrova, H. Gibbs, G. Rupper, C. Ell, O. Shchekin, and D. Deppe, *Vacuum Rabi splitting with a single quantum dot in a photonic crystal nanocavity*, Nature **432**, 200 (2004).

[11] A. Faraon, I. Fushman, D. Englund, N. Stoltz, P. Petroff, and J. Vuckovic, *Coherent generation of non-classical light on a chip via photon-induced tunnelling and blockade*, Nature Physics **4**, 859 (2008).

[12] K. Hennessy, A. Badolato, M. Winger, D. Gerace, M. Atatuere, S. Gulde, S. Faelt, E. L. Hu, and A. Imamoglu, *Quantum nature of a strongly coupled single quantum dot-cavity system*, Nature **445**, 896 (2007).

[13] M. T. Rakher, N. G. Stoltz, L. A. Coldren, P. M. Petroff, and D. Bouwmeester, *Externally mode-matched cavity quantum electrodynamics with charge-tunable quantum dots*, Phys. Rev. Lett. **102**, 097403 (2009).

[14] A. Reinhard, T. Volz, M. Winger, A. Badolato, K. J. Hennessy, E. L. Hu, and A. Imamoglu, *Strongly correlated photons on a chip*, Nature Photonics **6**, 93 (2012).

[15] T. Volz, A. Reinhard, M. Winger, A. Badolato, K. J. Hennessy, E. L. Hu, and A. Imamoglu, *Ultrafast all-optical switching by single photons*, Nature Photonics **6**, 605 (2012).

[16] Y. Ota, D. Takamiya, R. Ohta, H. Takagi, N. Kumagai, S. Iwamoto, and Y. Arakawa, *Large vacuum Rabi splitting between a single quantum dot and an H0 photonic crystal nanocavity*, Applied Physics Letters **112**, 093101 (2018).

[17] E. Peter, P. Senellart, D. Martrou, A. Lemaître, J. Hours, J. M. Gérard, and J. Bloch, *Exciton-photon strong-coupling regime for a single quantum dot embedded in a microcavity*, Phys. Rev. Lett. **95**, 067401 (2005).

[18] M. Lermer, N. Gregersen, F. Dunzer, S. Reitzenstein, S. Höfling, J. Mørk, L. Worschech, M. Kamp, and A. Forchel, *Bloch-wave engineering of quantum dot micropillars for cavity quantum electrodynamics experiments*, Phys. Rev. Lett. **108**, 057402 (2012).

[19] V. Loo, C. Arnold, O. Gazzano, A. Lemaître, I. Sagnes, O. Krebs, P. Voisin, P. Senellart, and L. Lanco, *Optical nonlinearity for few-photon pulses on a quantum dot-pillar cavity device*, Phys. Rev. Lett. **109**, 166806 (2012).

[20] J. Kasprzak, K. Sivalertporn, F. Albert, C. Schneider, S. Höfling, M. Kamp, A. Forchel, S. Reitzenstein, E. A. Muljarov, and W. Langbein, *Coherence dynamics and quantum-to-classical crossover in an exciton–cavity system in the quantum strong coupling regime*, New Journal of Physics **15**, 045013 (2013).

[21] R. J. Warburton, *Single spins in self-assembled quantum dots*, Nature Materials **12**, 483 (2013).

[22] R. J. Warburton, C. Schaflein, D. Haft, F. Bickel, A. Lorke, K. Karrai, J. M. Garcia, W. Schoenfeld, and P. M. Petroff, *Optical emission from a charge-tunable quantum ring*, Nature **405**, 926 (2000).

[23] R. Miller, T. E. Northup, K. M. Birnbaum, A. Boca, A. D. Boozer, and H. J. Kimble, *Trapped atoms in cavity QED: coupling quantized light and matter*, Journal of Physics B: Atomic, Molecular and Optical Physics **38**, S551 (2005).

[24] H. Walther, B. T. H. Varcoe, B.-G. Englert, and T. Becker, *Cavity quantum electrodynamics*, Reports On Progress In Physics **69**, 1325 (2006).

[25] D. Wang, H. Kelkar, D. Martin-Cano, T. Utikal, S. Götzinger, and V. Sandoghdar, *Coherent coupling of a single molecule to a scanning Fabry–Pérot microcavity*, Phys. Rev. X **7**, 021014 (2017).

[26] D. Riedel, I. Söllner, B. J. Shields, S. Starosielec, P. Appel, E. Neu, P. Maletinsky, and R. J. Warburton, *Deterministic enhancement of coherent photon generation from a nitrogen-vacancy center in ultrapure diamond*, Phys. Rev. X **7**, 031040 (2017).

[27] K. Karrai and R. J. Warburton, *Optical transmission and reflection spectroscopy of single quantum dots*, Superlattices and Microstructures **33**, 311 (2003).

[28] M. Fox, *Quantum optics: An introduction*, Oxford University Press (2006).

[29] E. M. Purcell, *Proceedings of the american physical society*, Phys. Rev. **69**, 674 (1946).

[30] P. Lodahl, S. Mahmoodian, and S. Stobbe, *Interfacing single photons and single quantum dots with photonic nanostructures*, Rev. Mod. Phys. **87**, 347 (2015).

[31] G. Cui and M. G. Raymer, *Quantum efficiency of single-photon sources in the cavity-QED strong-coupling regime*, Opt. Express **13**, 9660 (2005).

[32] N. Somaschi, V. Giesz, L. De Santis, J. C. Loredo, M. P. Almeida, G. Hornecker, S. L. Portalupi, T. Grange, C. Anton, J. Demory, C. Gomez, I. Sagnes, N. D. Lanzillotti-Kimura, A. Lemaitre, A. Auffeves, A. G. White, L. Lanco, and P. Senellart, *Near-optimal single-photon sources in the solid state*, Nature Photonics **10**, 340 (2016).

[33] W. Nagourney, *Quantum electronics for atomic physics*, Oxford University Press (2010).

[34] L. Redaelli, G. Bulgarini, S. Dobrovolskiy, S. N. Dorenbos, V. Zwiller, E. Monroy, and J. M. Gérard, *Design of broadband high-efficiency superconducting-nanowire single photon detectors*, Superconductor Science and Technology **29**, 065016 (2016).

[35] J. Kasprzak, S. Reitzenstein, E. A. Muljarov, C. Kistner, C. Schneider, M. Strauss, S. Höfling, A. Forchel, and W. Langbein, *Up on the Jaynes-Cummings ladder of a quantum-dot/microcavity system*, Nature Materials **9**, 304 (2010).

[36] K. Kuruma, Y. Ota, M. Kakuda, S. Iwamoto, and Y. Arakawa, *Time-resolved vacuum Rabi oscillations in a quantum-dot–nanocavity system*, Phys. Rev. B **97**, 235448 (2018).

[37] E. T. Jaynes and F. W. Cummings, *Comparison of quantum and semiclassical radiation theories with application to the beam maser*, Proceedings of the IEEE **51**, 89 (1963).

[38] A. V. Kavokin, J. J. Baumberg, G. Malpuech, and F. P. Laussy, *Microcavities*, Oxford University Press (2007).

[39] D. E. Chang, A. S. Sørensen, E. A. Demler, and M. D. Lukin, *A single-photon transistor using nanoscale surface plasmons*, Nature Physics **3**, 807 (2007).

[40] A. V. Kuhlmann, J. Houel, A. Ludwig, L. Greuter, D. Reuter, A. D. Wieck, M. Poggio, and R. J. Warburton, *Charge noise and spin noise in a semiconductor quantum device*, Nature Physics **9**, 570 (2013).

[41] X. Ding, Y. He, Z.-C. Duan, N. Gregersen, M.-C. Chen, S. Unsleber, S. Maier, C. Schneider, M. Kamp, S. Höfling, C.-Y. Lu, and J.-W. Pan, *On-demand single photons with high extraction efficiency and near-unity indistinguishability from a resonantly driven quantum dot in a micropillar*, Phys. Rev. Lett. **116**, 020401 (2016).

[42] T. Kaldewey, S. Lüker, A. V. Kuhlmann, S. R. Valentin, J.-M. Chauveau, A. Ludwig, A. D. Wieck, D. E. Reiter, T. Kuhn, and R. J. Warburton, *Demonstrating the decoupling regime of the electron-phonon interaction in a quantum dot using chirped optical excitation*, Phys. Rev. B **95**, 241306 (2017).

[43] B. Guha, F. Marsault, F. Cadiz, L. Morgenroth, V. Ulin, V. Berkovitz, A. Lemaitre, C. Gomez, A. Amo, S. Combrie, B. Gerard, G. Leo, and I. Favero, *Surface-enhanced gallium arsenide photonic resonator with quality factor of* 6×10^6, Optica **4**, 218 (2017).

[44] C. Schneider, P. Gold, S. Reitzenstein, S. Höfling, and M. Kamp, *Quantum dot micropillar cavities with quality factors exceeding 250,000*, Applied Physics B **122**, 19 (2016).

[45] M. Arcari, I. Söllner, A. Javadi, S. Lindskov Hansen, S. Mahmoodian, J. Liu, H. Thyrrestrup, E. H. Lee, J. D. Song, S. Stobbe, and P. Lodahl, *Near-unity coupling efficiency of a quantum emitter to a photonic crystal waveguide*, Phys. Rev. Lett. **113**, 093603 (2014).

[46] G. Khitrova, H. M. Gibbs, M. Kira, S. W. Koch, and A. Scherer, *Vacuum rabi splitting in semiconductors*, Nature Physics **2**, 81 (2006).

[47] B. Urbaszek, E. J. McGhee, M. Krüger, R. J. Warburton, K. Karrai, T. Amand, B. D. Gerardot, P. M. Petroff, and J. M. Garcia, *Temperature-dependent linewidth of charged excitons in semiconductor quantum dots: Strongly broadened ground state transitions due to acoustic phonon scattering*, Phys. Rev. B **69**, 035304 (2004).

[48] G. Shambat, B. Ellis, J. Petykiewicz, M. A. Mayer, A. Majumdar, T. Sarmiento, J. S. Harris, E. E. Haller, and J. Vuckovic, *Electrically driven photonic crystal nanocavity devices*, IEEE Journal of Selected Topics in Quantum Electronics **18**, 1700 (2012).

[49] L. Greuter, S. Starosielec, A. V. Kuhlmann, and R. J. Warburton, *Towards high-cooperativity strong coupling of a quantum dot in a tunable microcavity*, Phys. Rev. B **92**, 045302 (2015).

[50] J. Miguel-Sánchez, A. Reinhard, E. Togan, T. Volz, A. Imamoglu, B. Besga, J. Reichel, and J. Estève, *Cavity quantum electrodynamics with charge-controlled quantum dots coupled to a fiber Fabry–Pérot cavity*, New Journal of Physics **15**, 045002 (2013).

[51] L. Greuter, D. Najer, A. V. Kuhlmann, S. R. Valentin, A. Ludwig, A. D. Wieck, S. Starosielec, and R. J. Warburton, *Epitaxial lift-off for solid-state cavity quantum electrodynamics*, Journal of Applied Physics **118**, 075705 (2015).

[52] R. J. Barbour, P. A. Dalgarno, A. Curran, K. M. Nowak, H. J. Baker, D. R. Hall, N. G. Stoltz, P. M. Petroff, and R. J. Warburton, *A tunable microcavity*, Journal of Applied Physics **110**, 053107 (2011).

[53] L. Greuter, S. Starosielec, D. Najer, A. Ludwig, L. Duempelmann, D. Rohner, and R. J. Warburton, *A small mode volume tunable microcavity: Development and characterization*, Applied Physics Letters **105**, 121105 (2014).

[54] D. Hunger, C. Deutsch, R. J. Barbour, R. J. Warburton, and J. Reichel, *Laser micro-fabrication of concave, low-roughness features in silica*, AIP Advances **2**, 012119 (2012).

[55] S.-B. Zheng and G.-C. Guo, *Efficient scheme for two-atom entanglement and quantum information processing in cavity QED*, Phys. Rev. Lett. **85**, 2392 (2000).

[56] J. M. Fink, M. Goeppl, M. Baur, R. Bianchetti, P. J. Leek, A. Blais, and A. Wallraff, *Climbing the Jaynes-Cummings ladder and observing its $\sqrt{n}$ nonlinearity in a cavity QED system*, Nature **454**, 315 (2008).

[57] L. Schneebeli, M. Kira, and S. W. Koch, *Characterization of strong light-matter coupling in semiconductor quantum-dot microcavities via photon-statistics spectroscopy*, Phys. Rev. Lett. **101**, 097401 (2008).

[58] A. Stockklauser, P. Scarlino, J. V. Koski, S. Gasparinetti, C. K. Andersen, C. Reichl, W. Wegscheider, T. Ihn, K. Ensslin, and A. Wallraff, *Strong coupling cavity QED with gate-defined double quantum dots enabled by a high impedance resonator*, Phys. Rev. X **7**, 011030 (2017).

[59] X. Mi, J. V. Cady, D. M. Zajac, P. W. Deelman, and J. R. Petta, *Strong coupling of a single electron in silicon to a microwave photon*, Science **355**, 156 (2017).

[60] N. Samkharadze, G. Zheng, N. Kalhor, D. Brousse, A. Sammak, U. C. Mendes, A. Blais, G. Scappucci, and L. M. K. Vandersypen, *Strong spin-photon coupling in silicon*, Science **359**, 1123 (2018).

[61] A. J. Landig, J. V. Koski, P. Scarlino, U. C. Mendes, A. Blais, C. Reichl, W. Wegscheider, A. Wallraff, K. Ensslin, and T. Ihn, *Coherent spin-photon coupling using a resonant exchange qubit*, Nature **560**, 179 (2018).

[62] H. C. Casey, D. D. Sell, and K. W. Wecht, *Concentration dependence of the absorption coefficient for n- and p-type GaAs between 1.3 and 1.6 eV*, Journal of Applied Physics **46**, 250 (1975).

[63] A. Högele, S. Seidl, M. Kroner, K. Karrai, R. J. Warburton, B. D. Gerardot, and P. M. Petroff, *Voltage-controlled optics of a quantum dot*, Phys. Rev. Lett. **93**, 217401 (2004).

[64] A. V. Kuhlmann, J. Houel, D. Brunner, A. Ludwig, D. Reuter, A. D. Wieck, and R. J. Warburton, *A dark-field microscope for background-free detection of resonance fluorescence from single semiconductor quantum dots operating in a set-and-forget mode*, Review of Scientific Instruments **84**, 073905 (2013).

[65] P. A. Dalgarno, J. M. Smith, J. McFarlane, B. D. Gerardot, K. Karrai, A. Badolato, P. M. Petroff, and R. J. Warburton, *Coulomb interactions in single charged self-assembled quantum dots: Radiative lifetime and recombination energy*, Phys. Rev. B **77**, 245311 (2008).

[66] A. Kuhn and D. Ljunggren, *Cavity-based single-photon sources*, Contemporary Physics **51**, 289 (2010).

[67] D. Najer, I. Söllner, P. Sekatski, V. Dolique, M. C. Löbl, D. Riedel, R. Schott, S. Starosielec, S. R. Valentin, A. D. Wieck, N. Sangouard, A. Ludwig, and R. J. Warburton, *A gated quantum dot far in the strong-coupling regime of cavity-QED at optical frequencies*, arXiv:1812.08662 (2018).

[68] C. Dory, K. A. Fischer, K. Müller, K. G. Lagoudakis, T. Sarmiento, A. Rundquist, J. L. Zhang, Y. Kelaita, N. V. Sapra, and J. Vučković, *Tuning the photon statistics of a strongly coupled nanophotonic system*, Phys. Rev. A **95**, 023804 (2017).

[69] Z. Wasilewski, S. Fafard, and J. McCaffrey, *Size and shape engineering of vertically stacked self-assembled quantum dots*, Journal of Crystal Growth **201-202**, 1131 (1999).

[70] F. Beauville and The VIRGO Collaboration, *The VIRGO large mirrors: a challenge for low loss coatings*, Classical and Quantum Gravity **21**, S935 (2004).

[71] A. V. Kuhlmann, J. H. Prechtel, J. Houel, A. Ludwig, D. Reuter, A. D. Wieck, and R. J. Warburton, *Transform-limited single photons from a single quantum dot*, Nature Communications **6**, 8204 (2015).

[72] W. Franz, *Einfluß eines elektrischen Feldes auf eine optische Absorptionskante*, Zeitschrift für Naturforschung A **13** (1958).

[73] V. L. Keldysh, *Behaviour of non-metallic crystals in strong electric fields*, J. Exptl. Theoret. Phys. (USSR) **33** (1957).

[74] D. E. Aspnes, *Electric-field effects on optical absorption near thresholds in solids*, Phys. Rev. **147**, 554 (1966).

[75] J. Hader, N. Linder, and G. H. Döhler, *k·p theory of the Franz-Keldysh effect*, Phys. Rev. B **55**, 6960 (1997).

[76] B. Knupfer, P. Kiesel, M. Kneissl, S. Dankowski, N. Linder, G. Weimann, and G. H. Dohler, *Polarization-insensitive high-contrast GaAs/AlGaAs waveguide modulator based on the Franz-Keldysh effect*, IEEE Photonics Technology Letters **5**, 1386 (1993).

[77] Y. Xuan, H. Lin, and P. D. Ye, *Simplified surface preparation for GaAs passivation using atomic layer-deposited high-κ dielectrics*, IEEE Transactions on Electron Devices **54**, 1811 (2007).

[78] J. Robertson, Y. Guo, and L. Lin, *Defect state passivation at III-V oxide interfaces for complementary metal–oxide–semiconductor devices*, Journal of Applied Physics **117**, 112806 (2015).

[79] C. K. Carniglia and D. G. Jensen, *Single-layer model for surface roughness*, Appl. Opt. **41**, 3167 (2002).

[80] J. Davies, *The physics of low-dimensional semiconductors: An introduction*, Cambridge University Press (1998).

[81] L. Zamora Peredo, L. García-González, J. Hernandez Torres, I. Cortes-Mestizo, V. Mendez-Garcia, and M. López-López, *Photoreflectance and raman study of surface electric states on AlGaAs/GaAs heterostructures*, Journal of Spectroscopy **2016**, 1 (2016).

[82] J. M. Bennett, *Recent developments in surface roughness characterization*, Measurement Science and Technology **3**, 1119 (1992).

[83] D. E. Wohlert, K. L. Chang, H. C. Lin, K. C. Hsieh, and K. Y. Cheng, *Improvement of AlAs–GaAs interface roughness grown with high As overpressures*, Journal

of Vacuum Science & Technology B: Microelectronics and Nanometer Structures Processing, Measurement, and Phenomena **18**, 1590 (2000).

[84] K. Vahala, *Optical microcavities*, Nature **424**, 839 (2003).

[85] M. Trupke, E. A. Hinds, S. Eriksson, E. A. Curtis, Z. Moktadir, E. Kukharenka, and M. Kraft, *Microfabricated high-finesse optical cavity with open access and small volume*, Applied Physics Letters **87**, 211106 (2005).

[86] D. Hunger, T. Steinmetz, Y. Colombe, C. Deutsch, T. W. Hänsch, and J. Reichel, *A fiber Fabry–Pérot cavity with high finesse*, New Journal of Physics **12**, 065038 (2010).

[87] A. A. P. Trichet, P. R. Dolan, D. M. Coles, G. M. Hughes, and J. M. Smith, *Topographic control of open-access microcavities at the nanometer scale*, Opt. Express **23**, 17205 (2015).

[88] H. Kelkar, D. Wang, D. Martín-Cano, B. Hoffmann, S. Christiansen, S. Götzinger, and V. Sandoghdar, *Sensing nanoparticles with a cantilever-based scannable optical cavity of low finesse and sub-λ^3 volume*, Phys. Rev. Applied **4**, 054010 (2015).

[89] F. Chen, Z. Deng, Q. Yang, H. Bian, G. Du, J. Si, and X. Hou, *Rapid fabrication of a large-area close-packed quasi-periodic microlens array on BK7 glass*, Opt. Lett. **39**, 606 (2014).

[90] M. He, X. Yuan, J. Bu, and W. C. Cheong, *Fabrication of concave refractive microlens arrays in solgel glass by a simple proximity-effect-assisted reflow technique*, Opt. Lett. **29**, 1007 (2004).

[91] P. Nussbaum, R. Völkel, H. P. Herzig, M. Eisner, and S. Haselbeck, *Design, fabrication and testing of microlens arrays for sensors and microsystems*, Pure and Applied Optics: Journal of the European Optical Society Part A **6**, 617 (1997).

[92] J. Benedikter, T. Hümmer, M. Mader, B. Schlederer, J. Reichel, T. W. Hänsch, and D. Hunger, *Transverse-mode coupling and diffraction loss in tunable Fabry–Pérot microcavities*, New Journal of Physics **17**, 053051 (2015).

[93] S. Calixto, M. Rosete-Aguilar, F. J. Sanchez-Marin, and L. C. neda Escobar, *Rod and spherical silica microlenses fabricated by CO_2 laser melting*, Appl. Opt. **44**, 4547 (2005).

[94] H.-K. Choi, D. Yoo, I.-B. Sohn, Y.-C. Noh, J.-H. Sung, S.-K. Lee, T.-M. Jeong, M. S. Ahsan, and J.-T. Kim, *CO_2 laser assisted fabrication of micro-lensed single-mode optical fiber*, J. Opt. Soc. Korea **19**, 327 (2015).

[95] H.-K. Choi, M. S. Ahsan, D. Yoo, I.-B. Sohn, Y.-C. Noh, J.-T. Kim, D. Jung, J.-H. Kim, and H.-M. Kang, *Formation of cylindrical micro-lens array on fused silica glass surface using CO_2 laser assisted reshaping technique*, Opt. Laser Technol. **75**, 63 (2015).

[96] K. M. Nowak, H. J. Baker, and D. R. Hall, *Efficient laser polishing of silica micro-optic components*, Appl. Opt. **45**, 162 (2006).

[97] F. Laguarta, N. Lupon, and J. Armengol, *Optical glass polishing by controlled laser surface-heat treatment*, Appl. Opt. **33**, 6508 (1994).

[98] G. W. Forbes, *Shape specification for axially symmetric optical surfaces*, Opt. Express **15**, 5218 (2007).

[99] R. L. Olmon, B. Slovick, T. W. Johnson, D. Shelton, S.-H. Oh, G. D. Boreman, and M. B. Raschke, *Optical dielectric function of gold*, Phys. Rev. B **86**, 235147 (2012).

[100] M. Uphoff, M. Brekenfeld, G. Rempe, and S. Ritter, *Frequency splitting of polarization eigenmodes in microscopic Fabry–Pérot cavities*, New Journal of Physics **17**, 013053 (2015).

[101] C. Law and H. Kimble, *Deterministic generation of a bit-stream of single-photon pulses*, Journal of Modern Optics **44**, 2067 (1997).

[102] J. A. Frey, H. J. Snijders, J. Norman, A. C. Gossard, J. E. Bowers, W. Löffler, and D. Bouwmeester, *Electro-optic polarization tuning of microcavities with a single quantum dot*, Optics Letters **43**, 4280 (2018).

[103] J.-P. Berenger, *A perfectly matched layer for the absorption of electromagnetic waves*, Journal of Computational Physics **114**, 185 (1994).

[104] J.-M. Jin, *Theory and computation of electromagnetic fields*, John Wiley & Sons, Inc. (2010).

[105] J. Johansson, P. Nation, and F. Nori, *Qutip 2: A Python framework for the dynamics of open quantum systems*, Computer Physics Communications **184**, 1234 (2013).

[106] K. A. Fischer, Y. A. Kelaita, N. V. Sapra, C. Dory, K. G. Lagoudakis, K. Müller, and J. Vučković, *On-chip architecture for self-homodyned nonclassical light*, Phys. Rev. Applied **7**, 044002 (2017).

[107] T. Grange, N. Somaschi, C. Antón, L. De Santis, G. Coppola, V. Giesz, A. Lemaître, I. Sagnes, A. Auffèves, and P. Senellart, *Reducing phonon-induced decoherence in solid-state single-photon sources with cavity quantum electrodynamics*, Phys. Rev. Lett. **118**, 253602 (2017).

[108] A. Javadi, private communication (2019).

[109] A. Reiserer, N. Kalb, G. Rempe, and S. Ritter, *A quantum gate between a flying optical photon and a single trapped atom*, Nature **508**, 237 (2014).

[110] R. Jozsa, *Fidelity for mixed quantum states*, Journal of Modern Optics **41**, 2315 (1994).

[111] P. Sekatski and N. Sangouard, private communication (2019).

[112] S. Sun, H. Kim, G. S. Solomon, and E. Waks, *A quantum phase switch between a single solid-state spin and a photon*, Nature Nanotechnology **11**, 539–544 (2016).

Acknowledgements

First and foremost, I would like to thank Prof. Richard J. Warburton for letting me join this very exciting ongoing project. I value very much his clear way of thinking and excellent support for the challenges that needed to be faced during this PhD. I am particularly grateful to him showing respect for my family life.

Secondly, I would like to thank my co-referee, Prof. Jacek Kasprzak, for taking the time to assess this thesis.

I would also like to thank: My predecessor, Lukas Greuter, for handing over his expertise on the microcavity experiment. Arne Ludwig, Sascha R. Valentin and Rüdiger Schott for growing such an excellent semiconductor sample for our experiments. Vincent Dolique for applying an extremely low-loss dielectric coating to our curved mirror templates. Sebastian Starosielec, Immo Söllner, Matthias C. Löbl, Daniel Riedel, Martina Renggli and Benjamin Petrak for support in the lab and theoretical inputs. Nicolas Sangouard and Pavel Sekatski for providing the analytical theory. Ivan Favero for inspiration on surface passivation. Henri Thyrrestrup Nielsen and Matthias C. Löbl for support in evaluating the second-order correlation measurements with very small binning times. Arne Ludwig, Philipp Treutlein, Melvyn Ho and Peter Lodahl for fruitful discussions. Many thanks to: Sascha Martin and his team from the mechanics shop for engineering the microcavity hardware. Dominik Sifrig for reliably providing liquid helium for our experiments (I have to note here that the one and only time our experiment was running out of helium due to issues with the helium liquefier was the day my second son was born). Michael Steinacher and his team for technical support from the electronics lab. Beat Glatz and Germaine Weaver for IT and administrative support, respectively. My successor, Natasha Tomm, and our new post-doc, Alisa Javadi for having a great past year together in the quantum-dot cavity-team and for their helpful support. I wish Natasha all the best for her PhD. I also thank the entire Nano-photonics group for the helpful and friendly working atmosphere. A special thanks goes to Nadine Leisgang's mom who repeatedly provided us with excellent cakes for our group meetings.

Last but not least, I am deeply grateful to my family and friends for their perpetual support and my beloved wife and kids particularly for their encouragement and patience.

List of publications

1. D. Najer, I. Söllner, P. Sekatski, V. Dolique, M. C. Löbl, D. Riedel, R. Schott, S. Starosielec, S. R. Valentin, A. D. Wieck, N. Sangouard, A. Ludwig, and R. J. Warburton, *A gated quantum dot far in the strong-coupling regime of cavity-QED at optical frequencies*,
Preprint at arXiv:1812.08662 (2018).

2. D. Najer*, M. Renggli*, D. Riedel, S. Starosielec, and R. J. Warburton, *Fabrication of mirror templates in silica with micron-sized radii of curvature*,
Applied Physics Letters **110**, 011101 (2017).
**equal contribution*

3. L. Greuter, D. Najer, A. V. Kuhlmann, S. R. Valentin, A. Ludwig, A. D. Wieck, S. Starosielec, and R. J. Warburton, *Epitaxial lift-off for solid-state cavity quantum electrodynamics*,
Journal of Applied Physics **118**, 075705 (2015).

4. L. Greuter, S. Starosielec, D. Najer, A. Ludwig, L. Duempelmann, D. Rohner, and R. J. Warburton, *A small mode volume tunable microcavity: Development and characterization*,
Applied Physics Letters **105**, 121105 (2014).